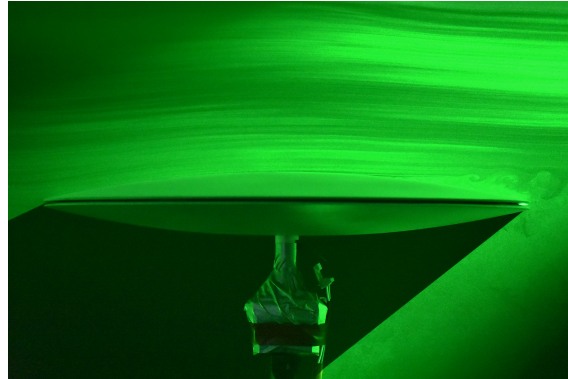




TÉCNICO
LISBOA



The Flying Saucer Concept for Micro Aerial Vehicles: Experimental Study

João Pedro Reis Rodrigues

Thesis to obtain the Master of Science Degree in

Aerospace Engineering

Supervisor: Prof. João Manuel Melo de Sousa

Examination Committee

Chairperson: Prof. Afzal Suleman

Supervisor: Prof. João Manuel Melo de Sousa

Member of the Committee: Prof. Agostinho Rui Alves da Fonseca

October 2021

Dedicated to those that are the lights illuminating my path.

Declaration

I declare that this document is an original work of my own authorship and that it fulfills all the requirements of the Code of Conduct and Good Practices of the Universidade de Lisboa.

Acknowledgments

This is a work that spans over a year of my life. In that time I have grown, both on a personal and professional level, and I am incredibly grateful that I did not do that alone. I would then like to thank the people that allowed me to get to this point in my path.

To my family, an immense amount of gratitude is owed, for their support through all of the turns, bumps and holes on the path, and for pushing me to make the decisions that led me here.

To Prof. João Manuel Melo de Sousa, I would like to express my thanks for his irreplaceable support throughout the development of this thesis. Many hurdles were met along the way, but his expertise, readiness to help and contagious enthusiasm for the project are what allowed them to be jumped over.

To my friends, who even unknowingly have helped me to keep moving forward towards my goals through their support, camaraderie and humour. I can not thank them enough, for a friend is always a light that can illuminate the dark path ahead.

And lastly, a special thank you to Vítor, who has inspired me in ways I cannot put into words, for his support, work ethic, passion and willingness to discuss ideas regarding this thesis, even if just to set my mind at ease.

Resumo

Nesta dissertação é apresentado um estudo experimental sobre uma inovadora asa circular rotativa, numa tentativa de determinar a sua viabilidade numa aplicação em micro veículos aéreos. Um protótipo foi desenvolvido com dois discos convexos rotativos, independentes um do outro, com diâmetro de 400 mm e uma espessura relativa de 12%. Três configurações de rotação foram testadas num túnel aerodinâmico. Os testes foram realizados a um número de Reynolds de 100000, para ângulos de ataque entre -2° e 20° , com uma variação de Advance Ratio (AdvR), o quociente entre a velocidade da extremidade do disco e o escoamento incidente, de 0 a 4 para a rotação síncrona e fixa em 2 para os restantes casos. Testes adicionais de visualização de escoamento foram realizados para o caso de rotação síncrona numa gama específica de ângulos e AdvR.

A rotação síncrona indicou um melhor desempenho do protótipo para AdvR=2, dados os valores mais baixos de arrasto e a pequena diferença entre valores de sustentação para os diferentes AdvR. Tal deve-se a uma minimização da bolha de separação com estruturas turbulentas de espessura moderadamente baixa. A rotação assíncrona com uma metade inferior estática sugere um aumento de sustentação com a adição de discos em rotação, dado que os valores de sustentação são superiores ao do caso completamente estático, mas inferiores ao caso de rotação síncrona. Os resultados para rotação oposta indicam uma influência mais significativa no momento de rolamento por parte do disco inferior, com o momento de guinada geral a cancelar-se, aproximadamente.

Palavras-chave: Asa Circular Rotativa, Micro Veículo Aéreo, Túnel Aerodinâmico, Visualização de Escoamento, Rotação Síncrona, Rotação Assíncrona

Abstract

In this dissertation, an experimental study is presented regarding an innovative rotating disc wing, in an attempt to determine the viability of such a design in an application for micro aerial vehicles. A prototype was developed with two independently rotating convex discs, with a diameter of 400 mm and a relative thickness of 12%. Three rotation configurations were tested in a wind tunnel. The tests were performed at a Reynolds number of 100000, in a range of angles of attack from -2° to 20° , with a variation of Advance Ratio (AdvR), the ratio between disc edge speed and incoming flow speed, from 0 to 4 for synchronous rotation and fixed at 2 for the remaining cases. Additional flow visualization tests were performed for the synchronous rotation case at a specific range of angles and AdvR.

Synchronous rotation indicated a better performance of the prototype at AdvR=2, given the lower values of drag and the small difference between lift values at different AdvR. This is due to a minimization of the separation bubble with turbulent structures of moderately small thicknesses. Asynchronous rotation with a static lower half suggests an increase in the generation of lift with the addition of rotating discs, since these values are larger than the fully static case, but smaller than the synchronous rotation one. Results for opposite rotations indicate a more significant influence of the bottom disc in the rolling moment, with the overall yaw moment approximately cancelling out.

Keywords: Rotating Disc Wing, Micro Aerial Vehicles, Wind Tunnel, Flow Visualization, Synchronous Rotation, Asynchronous Rotation

Contents

- Declaration v
- Acknowledgments vii
- Resumo ix
- Abstract xi
- List of Tables xvii
- List of Figures xix
- Nomenclature xxi

- 1 Introduction 1**
- 1.1 Motivation 1
- 1.2 Topic Overview 3
- 1.3 Objectives 3
- 1.4 Thesis Outline 3

- 2 Theoretical Concepts Behind a Rotating Disc Flight 5**
- 2.1 Fundamental Concepts 5
 - 2.1.1 Nomenclature 5
 - 2.1.2 Aerodynamic Forces and Moments 6
 - 2.1.3 Robins-Magnus Effect 7
 - 2.1.4 Gyroscopic Precession 8
 - 2.1.5 Laminar Separation Bubble 8
 - 2.1.6 von Kármán’s Problem 9
- 2.2 Overview of Previous Studies 10
 - 2.2.1 Transition of a Rotating Disc Flow 10
 - 2.2.2 Geometry’s Impact on the Aerodynamics of a Rotating Disc 11
 - 2.2.3 Disc’s Flight Dynamics 13

- 3 Conceptual Design 15**
- 3.1 Number of Motors 15
- 3.2 Size of the Prototype 16
- 3.3 Alpha Configuration 16
- 3.4 Beta Configuration 17

3.5	Gamma Configuration	18
3.6	Delta Configuration	19
3.7	Epsilon Configuration	19
3.8	Final Decision	20
4	Building the Prototype	23
4.1	Maximum Rotation Speed	23
4.2	Prototype's Profile	24
4.3	Motor Selection	25
4.4	Gear System	29
4.5	Central Structure	30
4.6	Discs' Design	31
4.7	Discs' Material	34
5	Testing the Prototype	37
5.1	Wind Tunnel Assembly	37
5.2	AerolST	39
5.3	Motors' Control and Operation	42
5.4	Hall Sensor Calibration	43
5.5	Wind Tunnel Corrections	45
5.6	Wind Tunnel Tests	46
5.6.1	Stability Tests	48
5.6.2	Quantification of Uncertainties	50
5.6.3	Synchronous Rotation Tests	53
5.6.4	Asynchronous Rotation Tests with Static Lower Half	57
5.6.5	Asynchronous Rotation Tests with Opposite Directions	59
5.6.6	Flow Visualization	62
5.7	Analysis of Results	65
6	Conclusions	69
6.1	Achievements	69
6.2	Future Work	71
A	Numerical Solution for Ordinary Differential Equations in von Kármán's Problem	75
B	Prototype's Drawings and General Dimensions	77
B.1	Bottom Disc	77
B.2	Top Disc	78
B.3	Central Structure	79

C Motors' Datasheets **80**

C.1 Maxon's EC 45 flat [27] 80

C.2 Faulhaber's Brushless DC-Flat Motors [6] 81

List of Tables

3.1	Decision-matrix for the different concepts	21
4.1	PLA's Properties [12]	23
4.2	Air properties at 20 °C [9].	25
4.3	Characteristics of the gears.	30
4.4	Properties of ABS and PLA [12].	35
5.1	Limiting values of the aerodynamic scale.	38
5.2	Speed calibration test for the small gear.	44
5.3	Speed calibration test for the disc.	44
5.4	Aerodynamic coefficients associated to the vertical support.	45
5.5	Results for an integration time of 5 seconds.	51
5.6	Results for an integration time of 10 seconds.	52
5.7	Results for systematic uncertainties for both multimeter integration times.	52
5.8	Results for random uncertainties for both multimeter integration times.	53
5.9	Results for the final uncertainties for both multimeter integration times.	53

List of Figures

1.1	Avro Canada's VZ-9AV Avrocar	2
1.2	All of the thrust directions produced by the ADIFO prototype [2].	2
2.1	Aerodynamic forces and moments represented on an aircraft [26].	7
2.2	A schematic representation of the Robins-Magnus effect on a disc [32].	7
2.3	A schematic representation of a laminar separation bubble [24].	9
2.4	Caption for figure in TOC.	10
2.5	Variation of transitional Reynolds number, Re_c , as a function of rotational velocity, Ω_D , for smooth and rough discs [40].	11
2.6	Comparison of the influence of disc thickness on aerodynamic characteristics [22].	12
2.7	Influence of disc rim edge curvature on aerodynamic characteristics [22].	12
2.8	Pitching moment coefficient results obtained by Kwon et al. [23].	13
3.1	Sketch of the alpha configuration.	17
3.2	Sketch of the beta configuration.	18
3.3	Sketch of the gamma configuration.	18
3.4	Sketch of the delta configuration.	19
3.5	Sketch of the epsilon configuration.	20
3.6	Alpha configuration.	22
3.7	Beta configuration.	22
3.8	Gamma configuration.	22
3.9	Delta configuration.	22
3.10	Epsilon configuration.	22
4.1	Graphical representation of a NACA 0012 airfoil [38].	24
4.2	Representation of the several considered radii.	26
4.3	Representation of the considered areas.	27
4.4	Maxon's EC 45 flat Ø42.8 mm, brushless, 12 <i>Watt</i> motor.	29
4.5	CAD of the gears.	30
4.6	3D printed prototype's central structure.	31
4.7	Lid system.	32
4.8	Top disc's casing with larger gear assembled.	32

4.9	One of the top disc's ribs.	33
4.10	Prototype with bottom disc assembled (note the Teflon tube near the periphery).	34
5.1	Wind tunnel assembly schematic.	37
5.2	Axes system of the aerodynamic scale [34].	38
5.3	AerolST's graphical user interface.	40
5.4	Reference menu.	40
5.5	Section of the measurement menu where the iterations can be defined.	41
5.6	Section of the measurement menu where the settling time can be set.	42
5.7	Electrical assembly.	43
5.8	Calibration setup.	44
5.9	Aerodynamic scale assembly, the vertical support can be seen connecting the prototype (top) to the scale (bottom).	46
5.10	Stability analysis for a multimeter integration time of 1 second.	49
5.11	Stability analysis for a multimeter integration time of 5 seconds.	49
5.12	Stability analysis for a multimeter integration time of 10 seconds.	49
5.13	Bottom disc with adhesive tape along its periphery.	54
5.14	Lift coefficient results for the synchronous rotation tests.	55
5.15	Drag coefficient results for the synchronous rotation tests.	56
5.16	Pitching moment coefficient results for the synchronous rotation tests.	56
5.17	Roll moment coefficient results for the synchronous rotation tests.	56
5.18	Yaw moment coefficient results for the synchronous rotation tests.	57
5.19	Lift coefficient results for the asynchronous rotation with static lower half tests.	58
5.20	Drag coefficient results for the asynchronous rotation with static lower half tests.	58
5.21	Pitching moment coefficient results for the asynchronous rotation with static lower half tests.	59
5.22	Roll moment coefficient results for the asynchronous rotation with static lower half tests.	59
5.23	Lift coefficient results for the asynchronous rotation with opposite directions tests.	60
5.24	Drag coefficient results for the asynchronous rotation with opposite directions tests.	60
5.25	Pitching moment coefficient results for the asynchronous rotation with opposite directions tests.	61
5.26	Roll moment coefficient results for the asynchronous rotation with opposite directions tests.	61
5.27	Yaw moment coefficient results for the asynchronous rotation with opposite directions tests.	61
5.28	Laser system.	62
5.29	Flow visualization for $\alpha=0^\circ$	63
5.30	Flow visualization for $\alpha=4^\circ$	63
5.31	Flow visualization for $\alpha=10^\circ$	64
5.32	Flow visualization for $\alpha=20^\circ$	64
A.1	Numerical solutions of the ordinary differential equations.	76

Nomenclature

Acronyms and Abbreviations

ABS Acrylonitrile Butadiene Styrene.

ADIFO All Directions Flying Object.

AdvR Advance Ratio.

AoA Angle of Attack.

CAD Computer-Aided Design.

CFD Computational Fluid Dynamics.

CSV Comma-Separated Values.

DC Direct Current.

DSLR Digital Single Lens Reflex.

MAV Micro Aerial Vehicle.

NACA National Advisory Committee for Aeronautics.

PC Personal Computer.

PIV Particle Image Velocimetry.

PLA Polylactic Acid.

PTFE Polytetrafluoroethylene.

UAV Unmanned Aerial Vehicle.

UFO Unidentified Flying Object.

USB Universal Serial Bus.

VTOL Vertical Take-Off and Landing.

Greek symbols

α Angle of attack.

o

η	Performance.	%
γ	Pressure angle.	°
μ	Dynamic viscosity.	kg.m ⁻¹ .s ⁻¹
ν	Kinematic viscosity.	m ² .s ⁻¹
ν_{Po}	Poisson's ratio.	-
Ω	Rotation speed.	rad.s ⁻¹
ρ	Density.	kg.m ⁻³
ρ	Density.	kg.m ⁻³
σ	Failure stress.	MPa
τ	Stress.	Pa
ξ	Characteristic length.	-

Roman symbols

A	Area.	m ²
AR	Aspect Ratio.	-
b	Systematic uncertainty.	-
c	Chord.	m
C_ϕ	Roll moment coefficient.	-
C_ψ	Yaw moment coefficient.	-
C_D	Drag coefficient.	-
C_L	Lift coefficient.	-
C_m	Pitching moment coefficient.	-
D	Diameter.	m
F	Force.	N
I	Inertia tensor.	-
i	Transmission ratio.	-
L	Angular momentum.	kg.m ² .s ⁻¹
M	Torque.	N.m
p	Pressure.	Pa

Q	Uncertainty.	-
\bar{r}	Midpoint radius.	m
\bar{Re}	Midpoint Reynolds number.	-
r	Radius.	m
Re	Reynolds number.	-
s	Random uncertainty.	-
S_f	Safety factor.	-
U_∞	Incoming flow speed.	m.s ⁻¹
Z	Gear's number of teeth.	-

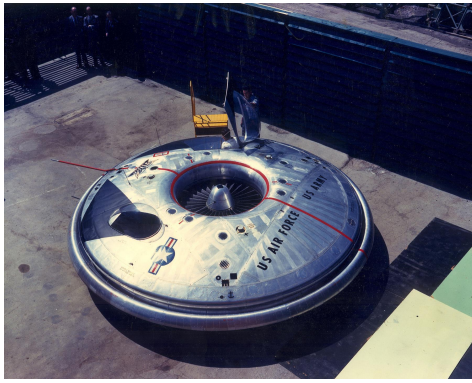
Chapter 1

Introduction

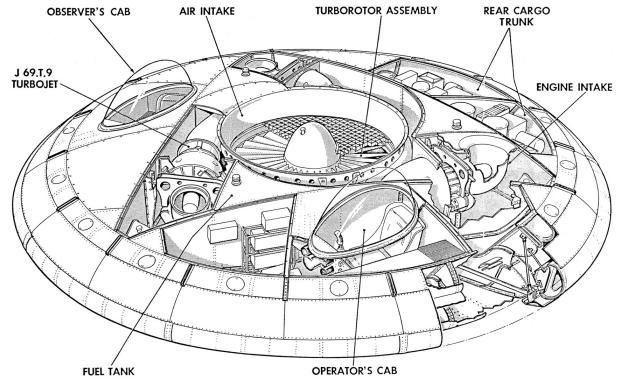
1.1 Motivation

The concept of an aircraft with a "Flying Saucer" shape has been present in humanity's imagination since the midway point of last century. Prompted by the surge of so-called Unidentified Flying Objects (UFO) sightings, as well as through the representation of said aircraft in all forms of science fiction media, several engineers and researchers have been fascinated by the idea of converting these works of fiction into real, practical applications. As such, several studies have been made on circular wings and their feasibility, both in terms of generated aerodynamic forces and aircraft stability and control. One of the most recognizable prototypes that went past the design phase is Avro Canada's VZ-9AV Avrocar, a manned aircraft with circular wing that used the exhaust from turbojet engines to drive a circular "turborotor" which produced thrust. By directing this thrust, lift could be generated and some level of control could be achieved. The aircraft proved that the concept was possible, however in a not very practical way: it could not rise more than a couple of meters off the ground and wind tunnel tests deemed it to be aerodynamically unstable. The growing number of issues with the design and the increasing cost of the project made it very difficult for the prototype to ever reach the production stage, eventually being cancelled in December of 1961 [39].

However, the rise of interest in the Unmanned Aerial Vehicle (UAV), in particular the smaller platforms, of recent years has provided a renewed interest in the Flying Saucer concept. The All Directions Flying Object (ADIFO) prototype arose from such circumstances, offering a small Vertical Take-Off and Landing (VTOL) platform with unique aerodynamic features (such as a high lift-to-drag ratio and a smooth transition from subsonic to supersonic flight) and incredible manoeuvrability, due to its shape and use of multiple thrust nozzles [1].



(a) Overhead view of the Avrocar [11].



(b) Cutaway drawing of the Avrocar showing its major components [10].

Figure 1.1: Avro Canada's VZ-9AV Avrocar

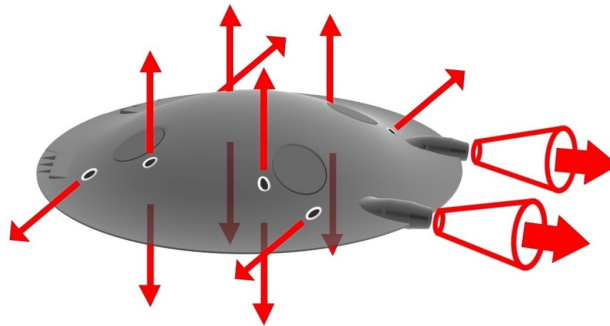


Figure 1.2: All of the thrust directions produced by the ADIFO prototype [2].

Micro Aerial Vehicles (MAVs), which are categorized as autonomous flying vehicles with size restrictions, offer tremendous versatility, being used in all sorts of military, civilian and recreational activities. For the specific application in the military branch, the greatest advantage of these MAVs is their capability for stealth, mainly due to their small size. As such, the use of the saucer shape in a MAV prototype could further increase its stealth capabilities, due to being a shape difficult to detect on radar and to the elimination of the rotor blades (responsible for the characteristic noise associated to these drones). Additionally, given that these blades are considerably fragile components of these vehicles, removing them increases the robustness of the MAV. This factor is quite relevant, since the small size and high manoeuvrability of a MAV makes it a very adequate candidate for information gathering missions, in both military and civilian fields, sometimes in tight spaces where a larger platform could not operate. It is then inevitable that a MAV in this scenario is susceptible to damage and therefore it is important to be sufficiently robust to finish the mission even when hit by debris.

1.2 Topic Overview

Several studies have been performed on flying discs (more commonly Frisbee's, used for recreational purposes, although some have studied Olympic discus as well) to better understand how the rotation of a disc in flight can contribute to its generation of aerodynamic forces and moments, stability and control. In the present thesis an innovative wing configuration with two independently rotating discs, placed symmetrically on top of each other, is developed and then tested at a wind tunnel, to study its generated aerodynamic forces and moments, therefore determining the viability of its application on MAV prototypes.

1.3 Objectives

As such, this thesis has essentially two objectives:

- Develop a functional prototype on which the aforementioned concept can be tested in a wind tunnel;
- Study the aerodynamic characteristics of said prototype, to determine the eventual practical applications of the proposed configuration.

1.4 Thesis Outline

This thesis is comprised of chapters, with this first one being the introduction where the topic and motivation for this work are presented.

In chapter 2 a summary of the relevant theoretical concepts to know is made, as well as a quick overview of some previous studies, of interest to the proposed configuration. There is a particular incidence on studies done on flow transition over a rotating disc and on the impact that the disc's geometry has on its aerodynamics.

In chapter 3 the process of reaching the final design concept is explained. The parameters that were initially considered are presented and the several design options are summarized. A decision matrix is shown, to better illustrate the decision making process that led to one of the designs being selected.

In chapter 4 the process of turning the selected design concept into a physical prototype is described. The additional parameters that were considered at this stage of development are presented. Calculations on the required torque are made, and the electric motors that will power the prototype are selected, based on the obtained values. The characteristics of the gear system are determined. A quick study on 3D printing materials is made in order to select the best option for all components of the prototype.

In chapter 5 the experimental assembly is showcased, with a focus on the wind tunnel and motor's control assemblies. A quick overview of the software used to acquire the data is made. The calibration process is described and the necessary wind tunnel corrections are determined. A quantification of the uncertainties associated to this study is performed. Different rotation configurations and flow visualization tests are performed and their results analysed.

Lastly, chapter 6 presents the main conclusions and achievements of this thesis, along with suggestions of future work to be done.

Chapter 2

Theoretical Concepts Behind a Rotating Disc Flight

In this chapter, the fundamental concepts necessary for this study are summarized. An overview of several previous authors' studies, of interest to the particular case being studied in this thesis, is presented. Studies on flow transition over rotating discs as well as their aerodynamic performance are summarized.

2.1 Fundamental Concepts

The flight of a rotating disc is a complex phenomenon to study, where several aerodynamic concepts are applied. As such, it is important to clarify these concepts as well as define certain terms that will be used throughout this thesis.

2.1.1 Nomenclature

Two relevant terms to define are the leading edge and trailing edge of the disc which, just like in any other wing, represent the front edge (the one facing the incoming flow) and the rear edge respectively. However, given how this work deals with a rotating disc, these are looser definitions since the side that is facing the flow is constantly changing.

Also in regards to the rotation, the discs will have a retreating and an advancing side. The former is defined as the side moving away from the incoming flow, where the edge speed and free stream velocity have the same sign, and the latter is defined as the side moving towards the incoming flow, where the edge speed and free stream velocity have opposite signs.

As with any other wing, the prototype will have a centre of mass, where the force of gravity acts on the body, as well as a centre of pressure, the point where all aerodynamic forces are applied. The two

centres do not have to coincide with one another, with the centre of pressure being usually ahead (i.e. closer to the leading edge) of the centre of mass, for a Frisbee-like shape at typical flight angles of attack (AoA), as was summarized by Potts and Crowther [30].

The aspect ratio of a wing, written as AR , is defined as the ratio between the square of the wing span and the wing area. Given how the planform wing area of the proposed prototype is a circle, the ratio can be written as

$$AR = \frac{(2r)^2}{\pi r^2} = \frac{4}{\pi} \approx 1.27, \quad (2.1)$$

where r is the radius of the disc.

A final concept that needs to be defined, being crucial for this study, is the advance ratio (AdvR). This value is a measure of the edge speed of a disc in relation to the incoming flow speed and can be calculated as

$$AdvR = \frac{\Omega r}{U_\infty}, \quad (2.2)$$

where Ω is the rotation speed of the disc and U_∞ is the incoming flow speed. It is a commonly used ratio in rotating disc studies since it provides a dimensionless measure of the disc's rotation: if its value is equal to zero, the disc is static; if equal to 1, the edges of the disc are moving at the same speed as the incoming flow; if larger than 1, then the edges of the disc are moving faster than the free flow.

2.1.2 Aerodynamic Forces and Moments

One of the objectives of this thesis is to analyse the aerodynamic forces generated by the developed prototype. There are three to consider, one for each Cartesian axis: the lift force, acting on the vertical axis; the drag force, acting on the horizontal axis parallel to the incoming flow; and the side-force, acting on the horizontal axis perpendicular to the incoming flow.

To explain it simply, lift is generated in any wing-like body due to its shape: the idea is to utilize a principle of conservation to force the flow going over the wing to be faster than the one going under it, by making the flow cover a longer distance on the top side. According to Bernoulli's principle, faster moving air is associated to lower pressures, meaning that a pressure gradient will appear, responsible for the generation of a force perpendicular to the flow, commonly known as lift. This force will increase with the AoA up to a critical angle, from there decreasing rapidly. This is what is commonly referred to as stalling. As for drag, it is a force parallel to the flow that opposes the movement of the wing, being always present as long as the wing is moving.

Since these forces act on the centre of pressure, they will cause the prototype to experience moments in relation to its centre of mass, as can be visualized in figure 2.1: a pitching moment around an horizontal axis perpendicular to the free flow, a rolling moment around an horizontal axis parallel to the flow, and a yaw moment around a vertical axis. These moments define the stability of the prototype in-flight, so their analysis is important to determine the performance of the discs.

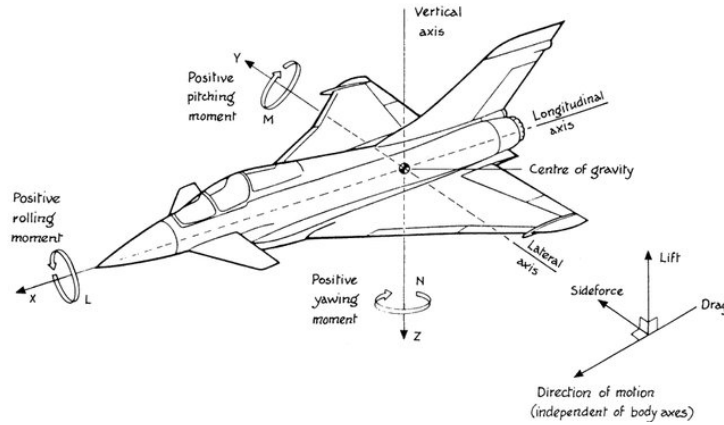


Figure 2.1: Aerodynamic forces and moments represented on an aircraft [26].

2.1.3 Robins-Magnus Effect

The rotation of the disc leads to the consideration of the Robins-Magnus effect: since an incoming flow is present and the disc is rotating, it will have both advancing and receding sides. Due to the signs of the free flow and disc's edge velocities, the air surrounding the receding side will have a faster motion than the one surrounding the advancing side. Recalling that, according to the Bernoulli principle, faster moving air is associated to lower pressures, there will be a generated side-force perpendicular to the airflow (Figure 2.2). Since the centre of pressure is not coincident with the centre of mass, this side force can induce a rolling moment. This effect was verified by Pozderac [32] in his experiments, where he also concluded that increasing the angular velocity of the disc increases the Robins-Magnus effect, which led to a larger rolling moment.

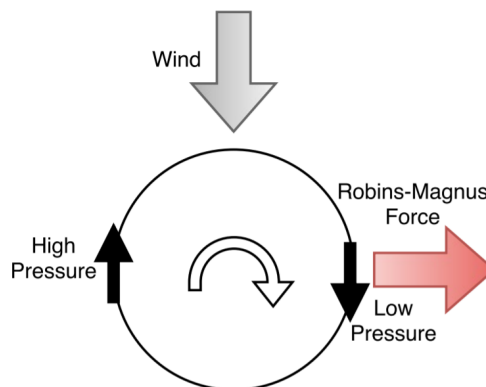


Figure 2.2: A schematic representation of the Robins-Magnus effect on a disc [32].

2.1.4 Gyroscopic Precession

Consider the angular momentum, \vec{L} , a rotational property that can be defined for a rigid body as:

$$\vec{L} = I\vec{\Omega}, \quad (2.3)$$

where I is the inertia tensor. The momentum will have the same direction as the rotation speed of the disc and, if no torques are applied, will remain constant in order to satisfy conservation laws. However, as was described in subsection 2.1.2, the prototype will have aerodynamic moments acting upon it, resulting in a rate of change of the momentum:

$$\frac{d\vec{L}}{dt} = \vec{M}, \quad (2.4)$$

where \vec{M} is the sum of all acting moments.

Assuming an upwards lift force applied on the centre of pressure, it will produce a nose-up pitching moment around the centre of mass. Since this moment is perpendicular to the angular momentum, it will not change its magnitude, only its direction. This change is called precession, being a critical phenomenon to the flight stability of a rotating disc.

In short, what is known as gyroscopic precession consists of the axis of rotation moving towards the direction of the applied torque. In the described example, the pitching moment is translated into a rolling moment: the immediate pitching instability can be suppressed, however, the disc swerves left or right, depending on the direction of the rotation speed. This effect can be commonly verified by throwing a Frisbee-like disc, with the achievable distance of the throw only possible due to it.

2.1.5 Laminar Separation Bubble

Recalling the objective of a potential application of the results obtained from this study on the design of a more efficient MAV, it is important to state that these usually fly at a value of Reynolds number $Re < 200000$. Flying at this low Reynolds number is inevitable, considering the small size of these vehicles, which implies the appearance of certain phenomena associated to this type of flight, namely one known as laminar separation bubble.

A laminar boundary layer is highly susceptible to separation under adverse pressure gradients, since it lacks the momentum transfer from turbulent mixing. When the layer separates from the surface, it forms a laminar and considerably unstable free shear layer. That promotes a transition, which leads to a high mixing and momentum transport, typically associated to turbulent flow, which allows for the flow to reattach itself to the surface. A fully turbulent boundary layer then continues past the reattachment point. A region with recirculating flow can be seen between the separation and reattachment points, known as

the laminar separation bubble. This bubble, which can be visualized in figure 2.3, is then responsible for a severe cut in aerodynamic performance, since drag increases and stability is reduced.

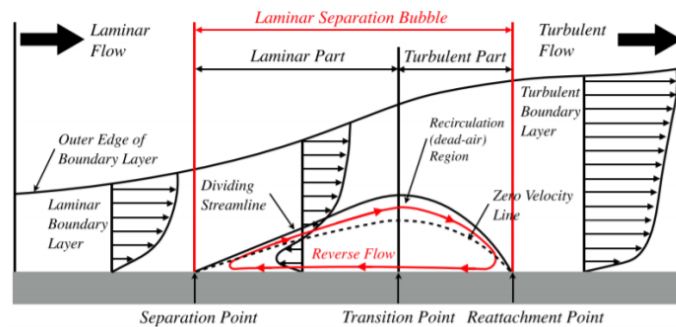


Figure 2.3: A schematic representation of a laminar separation bubble [24].

The size and shape of the bubble are very dependent of the Reynolds number and AoA. A so-called short bubble usually occurs at higher Reynolds numbers, having its biggest impact in inducing transition, not being particularly noticeable on the flow outside of it. As for a long bubble, occurring at lower Reynolds numbers and covering most of the wing's surface, typically has an impact in aerodynamic performance, since it interacts with the exterior flow quite vividly. If the Reynolds number is sufficiently reduced, the size of the bubble increases to a point that it can no longer reattach itself, translating into a complete separation. In terms of the AoA, the separation point moves further upstream as the angle is increased, a result of progressively more intense adverse pressure gradients. Near stall, at very high AoA, the bubble bursts and the aerodynamic performance plummets [33, 5].

2.1.6 von Kármán's Problem

In order to fully understand the type of flow that is seen over the prototype, it is important to mention what is commonly known as von Kármán swirling flow. This problem, solved by Theodore von Kármán in 1921, consists of an infinite rotating planar disc immersed in a still flow, where the rotation of said disc is the only contribution to setting the flow in motion. It is expected that a thin three-dimensional boundary layer is formed, due to the no-slip condition. The flow should be pushed outwards, due to the centrifugal force, and therefore be drawn axially so that mass conservation can be satisfied, as can be seen by the mean velocity profiles in figure 2.4, where the blue profile represented by U is the radial component, the red profile represented by V is the azimuthal component and the green profile represented by W is the axial component. Since the prototype consists of two discs, it is expected that a contribution of this type of flow is seen, once rotation is introduced.

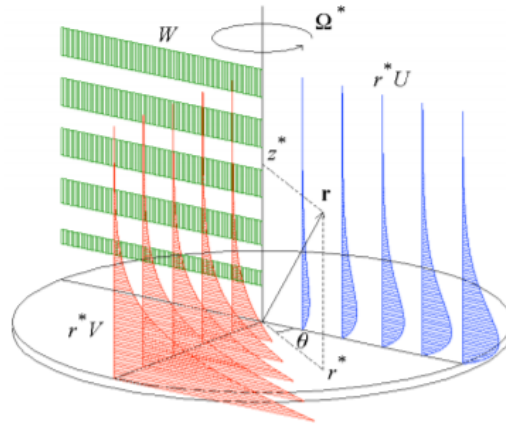


Figure 2.4: Sketch of the von Kármán boundary layer on a rotating disc showing the mean velocity profiles (in a stationary laboratory frame) [19].

2.2 Overview of Previous Studies

Several studies have been performed with a focus on a disc-wing geometry. Although the study done on this thesis regards a fairly unique and innovative configuration, and is therefore laying the foundation for future studies, some relevant information can be taken from previous studies on more standard configurations, and adapted to the study at hand.

2.2.1 Transition of a Rotating Disc Flow

Flow transition is of great relevance when dealing with any aerodynamic study and as such, a proper understanding of laminar-to-turbulent mechanisms can help in the setup of the tests to be performed. Lingwood [25] suggested that, for a Reynolds number of $Re = 510$ an absolute instability appears, indicating a possible point of transition for the flow over the rotating disc. This suggestion was further studied by Imayama et al. [21], reaching a similar conclusion and adding that at $Re = 630$ the boundary layer's thickness had increased substantially, a clear indicator of a fully turbulent flow.

Zoueshtiagh et al. [40] confirmed the theory presented by Lingwood which said that transition would always occur axisymmetrically and in a well defined radius. In the same paper, Lingwood proposes that the laminar-turbulent transition mechanism is not heavily affected by Coriolis and streamline curvature effects, something that was later confirmed by Imayama [19]. Zoueshtiagh included a study on the effects of surface roughness, where he concluded that they are of small importance until a "threshold relative roughness" (which exists somewhere between $335 \mu\text{m}$ and 1.325 mm) is reached.

Imayama [20] tested several edge conditions on the disc, to verify its effect on the transition mechanism. He reached a conclusion that, for the tested interval of Reynolds numbers, and in contrast to a previous study done by Healey [14], the different edge conditions had no significant impact on the flow's transition. Additionally, in the same study, Imayama also performed tests in regards to the surface

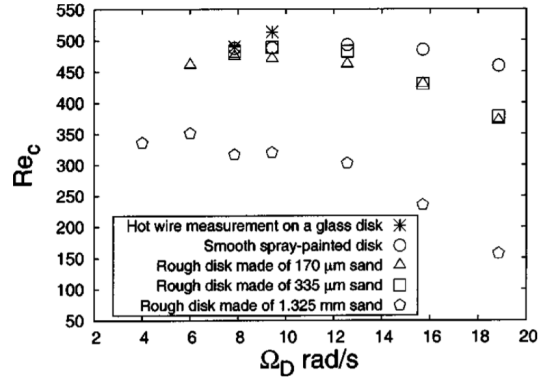


Figure 2.5: Variation of transitional Reynolds number, Re_c , as a function of rotational velocity, Ω_D , for smooth and rough discs [40].

roughness of the disc, where he concluded that the rougher the surface, the lower the Reynolds number where transition would start to occur, in line with the results obtained by Zoueshtiagh.

As for disc rotation in forward flight considerations, the experiments on flying discs performed by Higuchi et al. [15] proved that the rotation of the disc had a larger impact on the flow over its surface at smaller AoA, triggering a transition which led to the elimination of separation at the trailing edge of the disc. At higher AoA, roll-up of trailing vortices becomes very prominent, with the separated flow reattaching at about two thirds from the leading edge, being subject to a large downward induced flow.

2.2.2 Geometry's Impact on the Aerodynamics of a Rotating Disc

Kamaruddin [22] studied the effect of several disc geometric parameters on its aerodynamic characteristics. It was verified that the increase in the thickness of the disc has a small impact on the generated lift, in contrast with the impact on drag, with a considerable increase in profile drag being seen. This translates into a decrease of the lift-to-drag ratio, with an increase of thickness, leading to the conclusion that a better aerodynamic performance is expected at lower thicknesses. Additionally, the effects on the pitching moment were also studied, where it was verified that different thicknesses only have an impact on this variable at higher AoA. In these cases, a larger nose-up pitching moment was seen for a lower thickness (as a result of the centre of pressure being located further away from the disc's centre of mass), while a reduced nose-down pitching moment was verified for a higher thickness (as a result of the centre of pressure being located closer to the disc's centre of mass).

In the same paper, Kamaruddin also studies the aerodynamic effects of changing the disc's rim edge curvature. It is verified that a sharper edge disc leads to a smaller lift when compared to a rounded edge disc, for the range of tested AoA, something that is in line with what was concluded by Hoerner [16] that explained the phenomenon with the fact that a sharper edge disc has a lower effective aspect ratio, which leads to a higher induced drag and therefore, a reduced lift gradient. Despite that, Kamaruddin

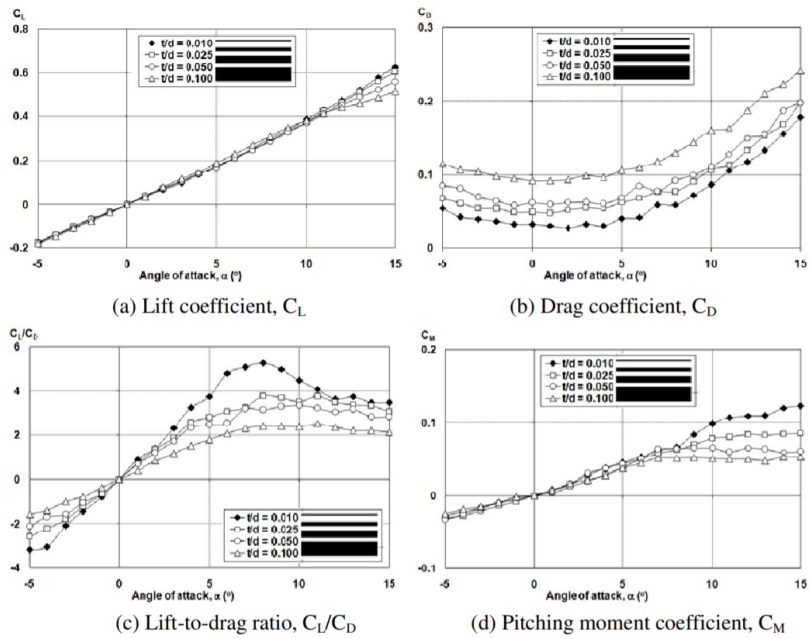


Figure 2.6: Comparison of the influence of disc thickness on aerodynamic characteristics [22].

did note that for a non-square leading or trailing edge curvature, the difference in lift between the two profiles is not very significant.

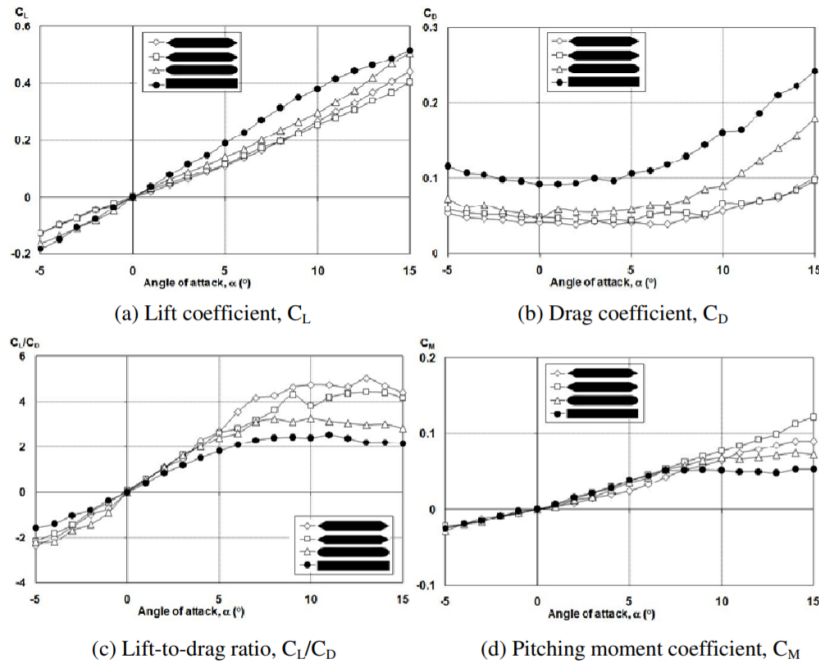


Figure 2.7: Influence of disc rim edge curvature on aerodynamic characteristics [22].

The drag results presented on said paper indicated a better performance (i.e. lower drag) for the sharper edge profiles, something that can be explained by the smaller amount of wake that they generate, when compared to the rounded edge profiles, which is once again in line with Hoerner's conclusions. Finally, in terms of the pitching moment, it was verified that the impact of the rim edge curvature is only noticeable at higher AoA, with the sharper edge disc producing a larger nose-up pitching moment with

the increase of said angle.

When analysing an elliptical airfoil in a low Reynolds number airflow, Kwon et al. [23] verified that this type of profile has a higher value of $\frac{dC_L}{d\alpha}$ for small AoA when compared to conventional symmetric profiles, due to asymmetric separation bubbles that form near the trailing edge of the wing. They also concluded that, in contrast with more traditional symmetric airfoils, the pitching moment coefficient about the quarter chord varied considerably with the AoA.

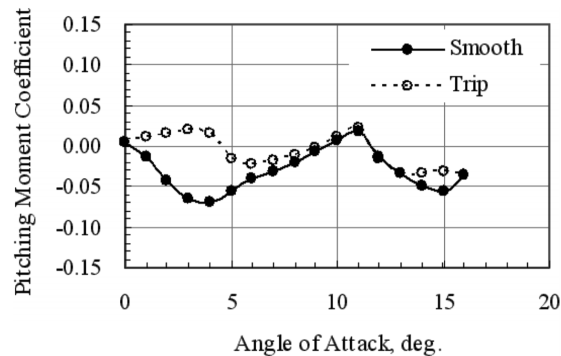


Figure 2.8: Pitching moment coefficient results obtained by Kwon et al. [23].

Pioneering the study of low aspect ratio wings at low Reynolds numbers, Mueller and Torres [28] concluded that wings with an aspect ratio below 1.25 have highly non-linear lift curves, presenting high stall AoA and non-constant slopes in the region before stall occurs, while those with an aspect ratio above that value exhibited a more linear behaviour on their lift curves. These results are in agreement with Hoerner's revisions [16, 17] of many of the theories associated to low aspect ratio wings, with a non-delta planform. The theory states that, for a finite wing generating lift, counter-rotating vortical structures form close to the wingtips, independently of the wing's aspect ratio, with their strength increasing with the AoA. In the case of low aspect ratio wings, these vortices may be present over most of the surface area, therefore influencing the aerodynamic characteristics of said wings. It is important to note that despite the fact that Hoerner's investigations correspond to Reynolds numbers significantly higher than the ones considered on this work, the aerodynamic theory behind them still holds.

2.2.3 Disc's Flight Dynamics

Since this work focuses on the analysis of aerodynamics coefficients on a disc-like wing, it is relevant to understand the type of forces and moments that a typical flying disc will be subject to throughout its flight path. As will be seen in later chapters, the developed prototype is tested on a fixed aerodynamic scale, which means that its flight path will not be physically observed, however the forces and moments responsible for it are still applied on the discs and therefore have an impact on the obtained aerodynamic results. As such, these are worthy of consideration.

Potts and Crowther [29] tested the effects of a disc's rotation speed, through a specific range of AdvR. It was seen that the rotation speed has very little impact on the aerodynamic forces, for pre-stall conditions. Additionally, the lift and drag curves remained constant, while pitching and rolling moments presented a slight variation for increased values of the AdvR. The changes can be explained with an unequal lift distribution, along with gyroscopic precession. Additionally, they found the lift and drag coefficients to be independent of the Reynolds number, for the range of wind tunnel speeds that were tested.

They later verified [31] that the rotation speed of the disc has a direct correlation with its manoeuvrability and stability. They reported that sharp banked turns were possible at very low rotation speeds, but with a risk of losing gyroscopic stability, while higher rotation speeds led to lower manoeuvrability but higher stability, to the point of the disc showing resistance to pitch.

The same authors performed further tests [30], where they concluded that for a non-spinning disc with incoming flow, the pitching moment is close to zero but slightly nose down, based on the pressure profile, at the tested AoA of 5° . Additionally, it was seen that the main contributions to the generation of lift are the low pressure peak on the leading edge and the large pressure difference on the trailing edge. They also utilised flow visualisation techniques to provide information that would enable a better understanding of the flow's physics. With them, they verified that the effect of spin leads to slight asymmetries in the wake's flow structures, with the vorticity of the trailing vortices being reduced on the advancing side and enhanced on the receding one.

In an attempt to find both the geometric parameters and launch conditions for an ideal Olympic discus throw, Seo et al. [35] performed a number of Computational Fluid Dynamics (CFD) simulations together with an optimization algorithm. It was concluded that, in order to achieve the maximum distance in the throw, the initial yaw rate on the axis of symmetry should be maximized, which can be translated into a better aerodynamic performance of the discus in flight, if a higher spin rate is applied. However, it is relevant to note that this effect could be due to the stabilisation of the discus throughout its flight path, instead of an improvement of the aerodynamic coefficients, if one takes the discoveries of Potts and Crowther into consideration.

Chapter 3

Conceptual Design

The development of the prototype to be used in testing presents several challenges. The objective is to obtain a design representative of the dual disc configuration, where each of the discs can rotate independently of one another since, in that case, a greater number of possible flight conditions can be tested. Different parameters have to be considered, such as the effect of the electric motors on the airflow surrounding the discs and the overall size of the prototype. These considerations led to a variety of concept designs, each one with different compromises that inevitably needed to occur. In the present chapter, these parameters are clarified, all of the concepts presented and the choice of the final design is justified. For better distinction between the different designs, a nomenclature based on the Greek alphabet was used.

3.1 Number of Motors

One important parameter to consider is the number of electric motors that is required for the proper operation of the prototype. Since the objective is to rotate two discs independently, the immediate choice would be to use two motors, one for each of the discs. Despite that, one can consider the possibility of a single motor being used, an option which is desirable due to the reduction in electric components (reducing the chance of failure as well) and the minimization of the overall cost of the prototype.

However, the analysis of this idea reveals a considerable disadvantage: the added overall complexity of the design. It is important to remember that the tests to be performed will require that both discs of the prototype can rotate independently from one another, which means that a complex system of gears would have to be developed, personalized to these particular needs. The complexity of such a system would certainly lead to a considerable development time, not to mention that the chances of failure could easily become far from negligible, taking said time away from the objective of this thesis: to study the aerodynamic properties of this particular prototype.

As such, the choice was made in favor of using two electric motors, something that is reflected in all of the concepts presented in the following sections.

3.2 Size of the Prototype

The prototype is to be tested in the open circuit wind tunnel located at Instituto Superior Técnico, as such, another parameter that should be considered is the overall dimensions of the prototype, more specifically its diameter. This should be chosen in such a way that the prototype is fully immersed in the incoming flow, preventing undesired effects which can compromise the obtained results and are difficult to correct *a posteriori*.

Also in consideration should be the range of AoA to be tested. It was decided to bring these up to a value of 20° on this particular study, in order to observe significantly different behaviours of the airflow over the prototype, so it is important to give some margin in the diameter, to maintain the full immersion of the prototype.

Additionally, the prototype needs to include a base to allow for a correct fixing to the aerodynamic scale, present at the experimental assembly. This base should elevate the discs to such a height that they are placed roughly in the centre of the jet stream, once again minimizing any potential interference.

The experimental assembly is better described in section 5.1, however, knowing that the free flow used in testing comes from a $135 \times 80 \text{ cm}^2$ section is enough to determine the overall dimensions of the prototype. All of these considerations led to an overall diameter of 400 mm.

3.3 Alpha Configuration

The first designs take into consideration the position of the motors. This is important for two factors: aerodynamics and cooling. Having external motors can potentially bring unwanted effects on the airflow over the discs, if these are at a sufficiently close range from one another, therefore compromising the obtained results. On the other hand, internal motors could lead to issues regarding overheating, therefore requiring a cooling system of some sort, which would likely lead to small incisions on the surface of the discs, again compromising the obtained results. However this issue is highly dependent on the characteristics of the chosen motor, with the added benefit that one can control its temperature with careful power application.

The alpha configuration is based on a compromise between the position of both motors: one of them being internal, the other being external. In such a way, overheating issues would only potentially arise

on the top motor, which leads to the possibility of small incisions on the top disc, constituting a system of air cooling. The bottom motor's effect on the bottom disc can be diminished through an extension of the motor's shaft, which would elevate the disk and so increase the range between the two components. To maximise the possible flight conditions to be tested, it is of interest that the middle platform (where the internal motor will be attached) is fixed i.e. independent from the rotation of both discs. That can be achieved through a simple system of rails and bearings. All of these elements are illustrated ¹ in figure 3.1:

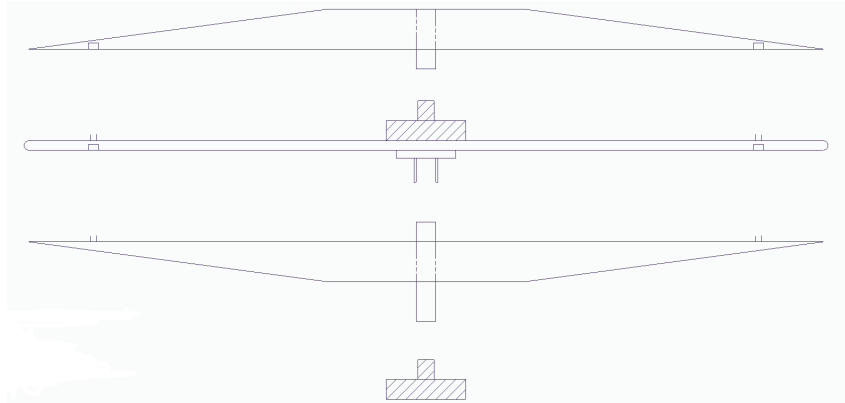


Figure 3.1: Sketch of the alpha configuration.

3.4 Beta Configuration

For the beta configuration, a priority on the motor's cooling is taken, with both of them being external in nature. In order to achieve this, an "arm" contraption is developed to act as a base for the motors. Its shape derives from an attempt to minimize the effect of such a structure on the incoming flow. A system of rails and bearings is once again used, in order to minimize friction between the two discs. This configuration offers an advantage in terms of the motor's cooling, with both of them being directly exposed to the incoming flow, as well as in a greater simplicity in the prototype itself, since no middle platform is required. However, the "arm" structure necessary to make such an assembly possible will bring added effects and compromise the aerodynamic results.

¹All of the presented sketches are merely a representation of their respective concepts, no precise dimensions were considered. In all of them, the blocks with diagonal lines represent the electric motors.

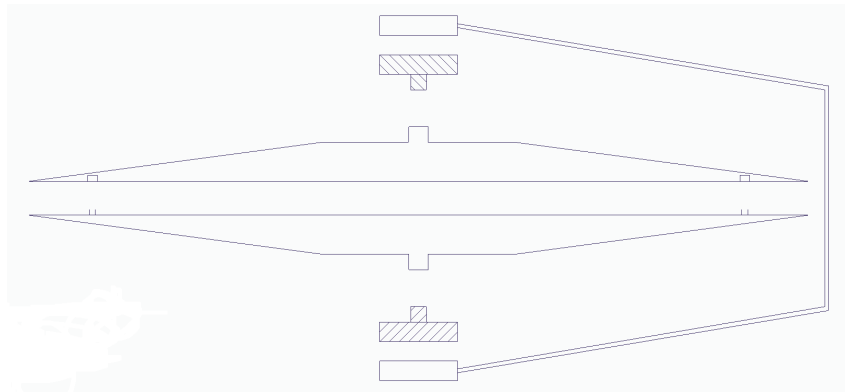


Figure 3.2: Sketch of the beta configuration.

3.5 Gamma Configuration

In a scenario where the aerodynamics of the discs take top priority, a configuration where both motors are assembled inside of the discs is most beneficial, eliminating their effect on the obtained aerodynamic results. For the gamma configuration, an additional parameter was considered: the orientation of the motors. This design includes a middle platform with a cutout to accommodate the motors and the vertical platforms to which these will be attached to. Since the axes of the motors' shafts will be perpendicular to the rotation axes of the discs, a system of bevel gears² could be implemented. This configuration offers a clear advantage in terms of the aerodynamic results however, it requires special care in the selection of the motors, to prevent overheating issues, since a necessity of incisions on the surface of the discs for cooling purposes could compromise the aerodynamic advantages of such a design.

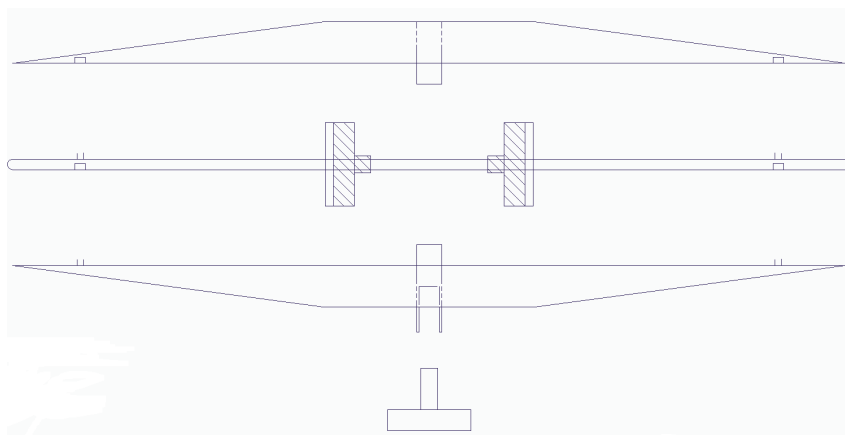


Figure 3.3: Sketch of the gamma configuration.

²Not represented in the sketch.

3.6 Delta Configuration

Still with a priority on the aerodynamic results, a delta configuration can be reached, this time with the axes of the motors' shafts aligned with the discs' axes of rotation. This is a simpler design, when compared to the gamma configuration, since a gear system is not required. The concept borrows several design points from previous configurations, most noticeably the system of rails and bearings from alpha, and the docking system between the base of the scale and the bottom disc from gamma. The uniqueness of this design comes from the bottom motor, now internal and fixed to the bottom of the middle platform. As was the case with the gamma configuration, special caution needs to be taken when choosing the electric motors, to avoid overheating issues.

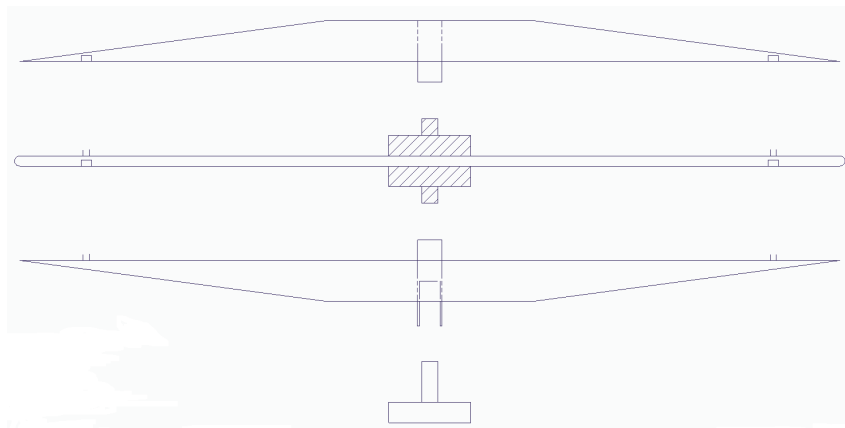


Figure 3.4: Sketch of the delta configuration.

3.7 Epsilon Configuration

After a better consideration of the gamma concept, it was noted that it could provide an opportunity to have a fixed central platform with a couple of adjustments. The key element of this new epsilon configuration is then a central pillar that crosses the entirety of the prototype. Since this element is fixed, attaching the central platform to it means that one can ensure that this is also fixed and therefore without any rotation speed, something that can be useful when operating the prototype, and which was difficult to ensure in previous designs. Additionally, the pillar can act as an alignment tool, guaranteeing the proper placement of all elements of the prototype during testing, as well as providing an easy way to implement the electric cables that will deliver power to the motors, with these going through the inside of it, as an hollow tube is being used. Finally, the pillar brings additional aerodynamic advantages, since its static nature leads to a smaller disturbance on the air flow on the bottom disc, when compared to the rotating element seen on previous configurations.

The gear system is very similar to the one present in the gamma design, with the exception of the gears aligned with the central pillar, which now need to be hollow, in order to accommodate it. Additional

ball bearings are placed on the pillar, not only to ensure a smooth interaction between the rotating discs and the static pillar, but also to fix the discs in their correct vertical positions.

This configuration provides the best results in terms of aerodynamics, however it is important to note that it also provides the highest complexity, both in terms of the components to be manufactured and in the assembly process.

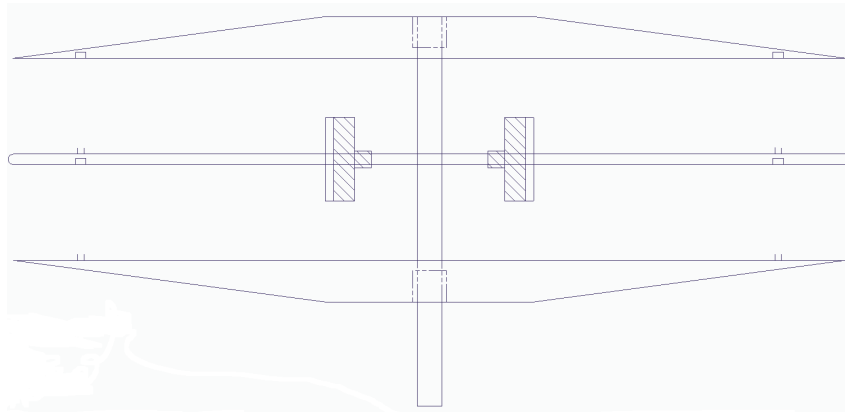


Figure 3.5: Sketch of the epsilon configuration.

3.8 Final Decision

In order to assist the decision of the design to be used, several parameters can be considered:

- **Ease of construction:** Represents the difficulty associated to the manufacture of the required parts for each of the designs. It also takes into consideration the difficulty in making said parts in a Computer-Aided Design (CAD) software.
- **Simplicity:** Considers the overall simplicity of the design. Relevant, since a more complex design can lead to unexpected issues in manufacture and operation of the prototype.
- **Aerodynamic results:** Takes into consideration all of the elements of a design that can potentially have a detrimental effect on the aerodynamic behaviour of the prototype, therefore leading to erroneous conclusions. Given the objective of this thesis, this is the most important parameter and as such is considered as a "tiebreaker" parameter in case of doubt in the choice between designs.
- **Cooling:** Represents the cooling that is provided to the electric motors. Considering the fact that these will have to be operating in a continuous manner during extended periods of time in order to

have reliable test results, temperature becomes a parameter that needs to be taken into account. However, it is of note that if the motor is not being pushed to its limits, the chances of it overheating decrease, even in a scenario where there is a lack of outside cooling. Therefore, a proper choice of the motors can compensate a poor score in this parameter.

- **Ease of assembly:** Considers the difficulty in assembling the actual prototype. It is important in the same way as the "simplicity" parameter, since a higher difficulty associated to this task can lead to large errors during testing, that can go as far as the self-destruction of the prototype itself.
- **Fail-safe:** In the same line as the previous parameter, this one represents the capability of the design in preventing unexpected mistakes from happening during a test.
- **Cable assembly:** Represents the possibility offered by a design of making a proper assembly of the electric cables necessary for the motors. Relevant in the sense that, in case of a design that does not allow it, a more complex system is required to operate the electric motors.
- **Independent rotation of discs:** Considers the difficulty in making each of the discs rotate independently from one another. It is important since it determines the overall complexity of the tests to be performed.

With these parameters in mind, one can build a "decision-matrix" with all of the considered configurations:

Configuration	Alpha	Beta	Gamma	Delta	Epsilon
Ease of construction	4	3	2	5	2
Simplicity	3	4	1	4	1
Aerodynamic results	3	1	4	4	5
Cooling	3	5	1	1	1
Ease of assembly	4	4	2	4	2
Fail-safe	4	2	4	1	5
Cable assembly	3	5	1	1	5
Independent rotation of discs	4	5	2	1	5
Total	28	29	17	21	26

Table 3.1: Decision-matrix for the different concepts

Note that, despite the quantitative scores being given for each parameter, this is a purely subjective classification with the scores going from 1 to 5, from worst to best respectively. In order to have a more visual representation of these results, several radar-plots were made, one for each of the concepts:



Figure 3.6: Alpha configuration.

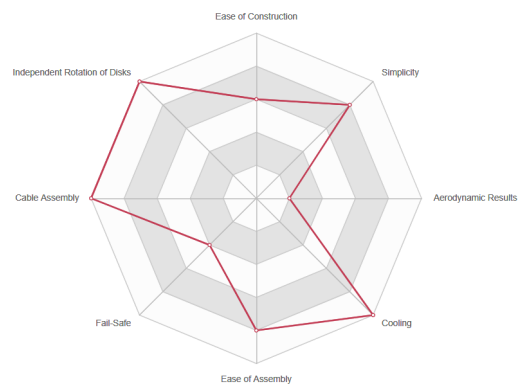


Figure 3.7: Beta configuration.

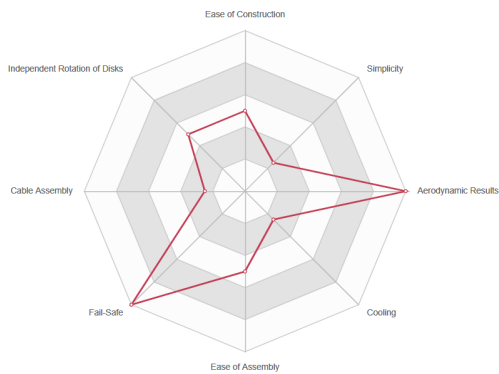


Figure 3.8: Gamma configuration.

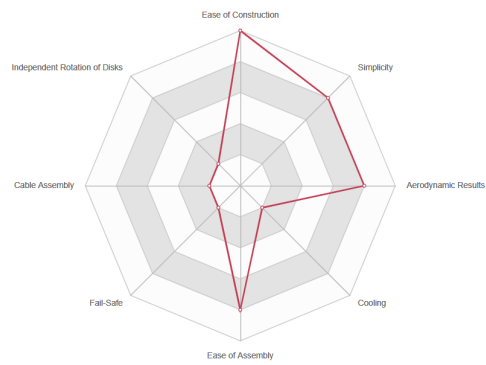


Figure 3.9: Delta configuration.

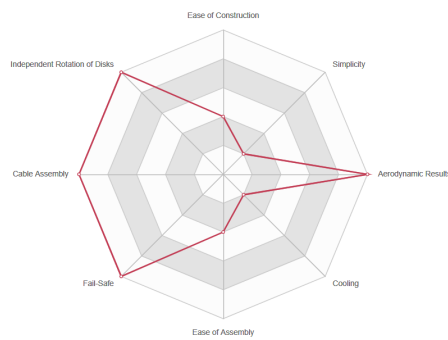


Figure 3.10: Epsilon configuration.

With these, it becomes clear that the choice should be between concepts alpha, beta and epsilon, due to their higher scores. However, as was mentioned before, the quality of the obtained aerodynamic results is of key importance to this thesis. As such, it is undeniable that, despite the higher complexity associated to both manufacture and assembly, the fact that the epsilon concept maintains a relatively small level of disturbance on the airflow over the discs, means that it is the one most suited to fulfill the objectives of this work. Using this logic, the choice was made to further develop this design.

Chapter 4

Building the Prototype

With the process of concept selection concluded, the focus can be shifted into turning the selected design into an actual prototype. This will add the consideration of more parameters, which will undoubtedly introduce further changes in the design. In the current chapter, all of these will be presented.

4.1 Maximum Rotation Speed

In order to have a better understanding of the interval of rotation speeds that can be used for the tests, one can look at the limit of the material itself before rupture. Imayama [19] determined such a speed, Ω_{max} , by using

$$\Omega_{max} = \frac{2}{D} \left(\frac{8\sigma_f}{S_f \rho_{PLA} (3 + \nu_{Po})} \right)^{\frac{1}{2}}, \quad (4.1)$$

where σ_f represents the tensile strength of the material to be used in the 3D printing manufacture process, meaning the maximum tensile load the material can withstand prior to fracture, in this case Polylactic Acid (PLA), a choice that is better explored in section 4.7. S_f represents a safety factor which, for this estimate, will be considered the same as in the mentioned paper, $S_f = 10$ and ν_{Po} is Poisson's ratio which, as mentioned by Imayama, has an approximately constant value of $\frac{1}{3}$ for all solids. By using the already defined diameter as well as the properties in table 4.1, a value of $\Omega_{max} = 413.2 \text{ rad.s}^{-1} \approx 3846 \text{ rpm}$ is obtained.

Tensile strength	$\sigma_f = 37 \text{ MPa}$
Density	$\rho_{PLA} = 1300 \text{ kg.m}^{-3}$

Table 4.1: PLA's Properties [12]

However, the obtained result was deemed to be an impractically high value of rotation speed and the maximum was instead set at $\Omega_{max} = 2000 \text{ rpm}$, very far from a potentially damaging speed.

4.2 Prototype's Profile

The shape and dimensions of the prototype's profile are important geometric parameters to define, since they will have an impact in the design process as well as the choice of the electric motors to use.

Given the scope of this thesis, and considering the findings of previous studies presented in subsection 2.2, a slender profile makes the most sense. As such, the relative maximum thickness was set to 12%, inspired by the commonly tested NACA 0012 profile. Based on the obtained diameter of 400 mm in section 3.2, this translates into a maximum thickness of 48 mm at the centre of the prototype.

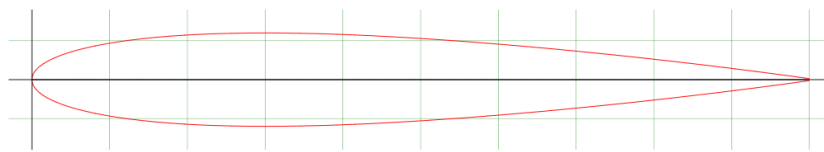


Figure 4.1: Graphical representation of a NACA 0012 airfoil [38].

The final parameter to consider is the shape of the profile, where two options were analysed: an elliptical profile and a biconvex profile. Both offer advantages and disadvantages, and the choice needs to be made keeping in mind that given the rotational nature of the prototype a compromise will always have to be made.

From the studies done by Kwon et al. [23] on an elliptical airfoil, one can see the benefit in aerodynamic performance due to the asymmetric separation bubbles that are formed. However, these can bring difficulties to the particular study of this thesis, since they will interfere with the overall flow over the prototype, creating a situation where it becomes difficult to separate the effects of the bubbles from the effects to be studied, in the obtained results. Additionally, the instability associated to the pitching moment coefficient about the quarter chord could also have a significant impact on the obtained results, therefore influencing any conclusions drawn from them.

As for the biconvex airfoil, it is a shape typically used in studies for supersonic, compressible flows, not being as beneficial for the case of subsonic flow. Despite that, the sharper edges of this profile align themselves with the study done by Kamaruddin [22], which should lead to a more aerodynamically efficient prototype.

As was mentioned previously, one needs to keep in mind that compromises will always have to be made and so, despite not being the best shape for subsonic flow, the lack of additional disturbances on the airflow, when compared to the elliptical airfoil, as well as the possibility of creating a more efficient prototype, make the biconvex airfoil the more suitable for the purposes of this thesis.

4.3 Motor Selection

An important element to be considered, due to its impact on all subsequent decisions, is the choice of the electric motors that will power the prototype. This involves the consideration of four distinct variables:

- **Power:** The higher the value of this parameter, the more energy is dispersed, leading to an increase of temperature within the discs which, as was seen in chapter 3, could lead to potential issues in the selected design. Therefore, the selected motor should have the smallest power possible, while respecting the remaining constraints.
- **Torque:** The motors will need to overcome the drag forces due to the flow over the discs as well as other loads associated to mechanical losses in the system. As such, the chosen motor should be able to provide enough torque to spin the discs at the desired speed.
- **Rotation speed:** It is imperative that the motors are capable of achieving high values of rotation speeds, so that a relevant array of tests can be performed on the prototype.
- **Size:** The motors need to have appropriate dimensions, in order for them to fit within the two discs and allowing for an overall slender profile of the prototype.

Out of all of these parameters, the one that is yet to be determined is the torque, since the maximum rotation speed has already been estimated in section 4.1, while the power and size parameters are more dependant on the available models of motors and therefore do not require an estimate. Since the objective is to have a prototype with a slender profile, a flat plate assumption was made for each of the discs, in order to facilitate calculations. In this case the air temperature was considered to be at 20 °C, with its properties present in table 4.2:

Density	$\rho = 1.204 \text{ kg.m}^{-3}$
Dynamic viscosity	$\mu = 1.825 \times 10^{-5} \text{ kg.m}^{-1}.\text{s}^{-1}$
Kinematic viscosity	$\nu = 1.516 \times 10^{-5} \text{ m}^2.\text{s}^{-1}$

Table 4.2: Air properties at 20 °C [9].

There are two speeds to be considered: the incoming flow velocity and the rotation speed of the discs. However, for this estimate, the incoming flow is considered negligible, since at low AoA the overall torque that it will apply on the discs is null, due to their symmetry and rotation. Even if higher AoA are considered, these situations usually lead to areas of separated flow with lower velocities, and therefore lower torques. As such, the calculation of the applied torque was made using only the rotation speed as reference.

Since the purpose of this estimate is to find the maximum torque that the motors will need to overcome, it is logical that the value for the rotation speed to be used is the maximum one obtained in section

4.1 of $\Omega_{max} = 209.44 \text{ rad.s}^{-1}$. The Reynolds number is defined by the ratio of inertial forces to viscous forces, which can be obtained from

$$Re_r = \left(\frac{\Omega r^2}{\nu} \right)^{\frac{1}{2}}, \quad (4.2)$$

where r is the radius of the disc, Ω is the angular velocity of the disc, and ν is the kinematic viscosity of the fluid, as defined by Imayama [19]. By using the radius at the edge of the disc of $r_{max} = 0.2 \text{ m}$ in equation 4.2, the maximum of the radial component of the Reynolds number can be obtained: $Re_{r_{max}} = 747$. Furthermore, through manipulation of the same equation and using the value of transition Reynolds number $Re_{r_{tr}} = 510$, based on the suggestion by Lingwood [25] that an absolute instability appears on that number, one can obtain the value of $r_{tr} = 0.137 \text{ m}$ as the radius where flow transition occurs, in this case.

We are dealing with a three-dimensional boundary layer, however, for this particular estimate, it was deemed acceptable to consider it to be axisymmetric. With that in mind, the total torque generated due to the boundary layer will be divided between the laminar regime contribution and the turbulent regime contribution. For this calculation, this value will be obtained through the sum of the torques calculated at the midpoints of the laminar and turbulent sections of the boundary layer. As such, using the value of $\bar{r}_l = 0.0685 \text{ m}$ will give the laminar Reynolds number of $\bar{Re}_l = 255$, while using $\bar{r}_t = 0.1685 \text{ m}$ will give the turbulent Reynolds number of $\bar{Re}_t = 626$.

A better visualization of the several radii can be seen in figure 4.2.

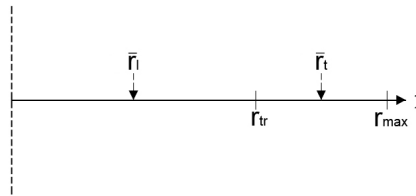


Figure 4.2: Representation of the several considered radii.

For the laminar regime, this particular case is equivalent to von Kármán's similarity solution of the Navier-Stokes equations for a rotating disc, corresponding to the flow described in section 2.1.6 where a characteristic length ξ is defined as

$$\xi = x \left(\frac{\Omega}{\nu} \right)^{\frac{1}{2}}. \quad (4.3)$$

Note that for this particular equation x refers to the axial direction. With this variable, the numerical solution for the Ordinary Differential Equations can be obtained, in this case: $G' = -0.6159$ (see Annex A). With it, an equation to calculate the tangential component of the laminar tension can be formulated as

$$\tau_{\theta_l} = \mu \frac{\partial V}{\partial x} = \mu \Omega \bar{r}_l \frac{\partial G}{\partial \xi} \frac{\partial \xi}{\partial x} = \mu \Omega \bar{r}_l G' \left(\frac{\Omega}{\nu} \right)^{\frac{1}{2}}, \quad (4.4)$$

and its absolute value obtained: $\tau_{\theta_l} = 0.6$ Pa.

For the value of the shear stress associated to the turbulent regime, an approach based on an estimate using the skin friction coefficient is selected. Based on the results of numerical simulations [4], the tangential component of said coefficient can be estimated as $c_{f_{\theta_t}} = 0.004$, using the previously calculated value of the Reynolds number for the considered point within the turbulent regime.

Using the definition of the skin friction coefficient,

$$c_{f_{\theta_t}} = \frac{\tau_{\theta_t}}{\frac{1}{2} \rho (\Omega \bar{r}_t)^2}, \quad (4.5)$$

the value of the tangential component of the turbulent stress can be obtained as $\tau_{\theta_t} = 3.0$ Pa.

It is important to obtain the areas of the disc that are considered to be in each of the regimes, for further calculations. These can be visualized in figure 4.3, where the striped area represents the laminar portion of the boundary layer, A_l , and the dotted area represents the turbulent portion of the boundary layer, A_t .

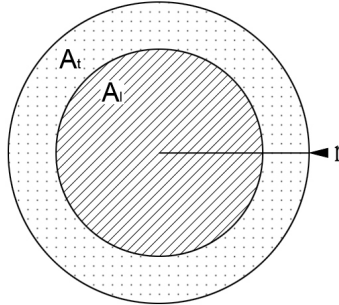


Figure 4.3: Representation of the considered areas.

Making use of the circle's area formula, the radius of the disc r , as well as the already obtained value of r_{tr} , one can easily calculate the values of these areas from

$$A_l = \pi r_{tr}^2, \quad (4.6)$$

$$A_t = \pi r^2 - A_l, \quad (4.7)$$

obtaining $A_l = 0.0598 \text{ m}^2$ and $A_t = 0.0659 \text{ m}^2$, respectively.

With the areas calculated, the respective forces can be calculated from

$$F_{\theta_l} = \tau_{\theta_l} \times A_l, \quad (4.8)$$

$$F_{\theta_t} = \tau_{\theta_t} \times A_t, \quad (4.9)$$

obtaining $F_{\theta_l} = 0.035 \text{ N}$ and $F_{\theta_t} = 0.2 \text{ N}$, respectively.

With these, and taking into consideration the midpoint approach that has been selected,

$$M_\theta = F_{\theta_l} \times \bar{r}_l + F_{\theta_t} \times \bar{r}_t \quad (4.10)$$

can be used to obtain the total of the torque that is applied on one of the discs, which is $M_\theta = 36.1 \text{ mN.m}$.

Finally, a consideration on the mechanical performance of the prototype's elements should be added. Since the prototype is designed to minimize losses due to the friction between the discs themselves as well as between them and the central pillar, with the use of several ball bearings, the value of this performance can be estimated to be $\eta_m = 90\%$. This means that, based upon this estimate, each electric motor will need to provide at least a torque of 40 mN.m . However, after some research on the available motors in the market, it became clear that no current option is capable of providing said torque, while having adequate dimensions for the project. To overcome this obstacle, a gear system is implemented with a transmission ratio approximately equal to two, meaning that the selected motor should be able to provide half of the calculated torque, as well as double the rotation speed of Ω_{max} . A more detailed overview and explanation of the gear system is provided in section 4.4.

Based upon these requisites, the conducted market research yielded two possible candidates. The first one is Maxon's EC 45 flat $\text{Ø}42.8 \text{ mm}$, brushless, 12 Watt motor. It provides a nominal torque of 23.6 mN.m and a nominal speed of 4540 rpm , within a small package capable of being implemented within the discs [27].

The second option is Faulhaber's brushless DC-Flat motors series 3216 012 BXT H. Providing a nominal torque of 38 mN.m and a nominal speed of 3860 rpm [6], some adjustments would have to be made to the gear system's ratio. Crucially however, this motor has a higher power of 20 W (meaning a higher dissipated power resulting in an increase in temperature) with a larger structure. In truth, this option was only considered to provide a backup from a different manufacturer, since Maxon's option is clearly superior, therefore being the one selected to be used in the prototype.

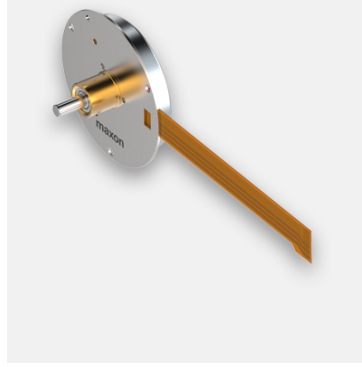


Figure 4.4: Maxon's EC 45 flat Ø42.8 mm, brushless, 12 *Watt* motor.

4.4 Gear System

As mentioned in section 4.3, a gear system with transmission ratio approximately equal to two is to be implemented, in order to overcome the challenge of finding a motor capable of providing enough torque in a small package.

To make the selection of the gears, some parameters must be known. The desired transmission ratio as well as the estimated distance between the axes of the gears³ are known values, however, an additional parameter is required. In this occasion the minimum number of teeth per gear was the chosen value to be estimated.

Firstly, from the transmission ratio,

$$i = \frac{D_2}{D_1} = \frac{Z_2}{Z_1}, \quad (4.11)$$

one can obtain the relationship between the gears' diameters and number of teeth, where i is the transmission ratio, D the gear's diameter, Z the number of teeth, and the subscripts 1 and 2 representing the smaller and larger gears respectively. With this it can be obtained that $D_2 = 2 \times D_1$ and $Z_2 = 2 \times Z_1$.

The number of teeth needs to be such that no interference happens during the contact between both gears, in other words, it needs to ensure a smooth operation of the gears. Their minima can be calculated using

$$Z_1 \geq -Z_2 + \sqrt{Z_2^2 + \frac{4(1 + Z_2)}{\sin^2(\gamma)}}, \quad (4.12)$$

where γ is the pressure angle, typically given the value of 20° [3]. As such, the minima of 15 teeth for the smaller gear and 30 teeth for the larger one are obtained.

The process of designing a gear from the very beginning is complicated, time consuming and can

³Corresponds to the distance between the centerlines of one of the motors and the central pillar, which can be estimated through the CAD file of the prototype

potentially lead to various errors during operation. As such, in order to design the gears for the prototype, Icus' CAD software was used [18]. This tool, ready to use directly from the store's website, allows for the user to simply introduce the desired parameters (present in table 4.3), with the design being generated automatically. Icus also provides unique materials for the 3D printing filament, specifically designed for gear systems due to their increased resistance to wear and high temperatures, with their I3 filament being selected in this case.

Characteristic	Smaller gear	Larger gear
Module	1.76	1.76
Number of teeth	17	34
Reference circle diameter	29.92 mm	59.84 mm
Width of bottom section	5 mm	5 mm
Width of top section	4 mm	-

Table 4.3: Characteristics of the gears.

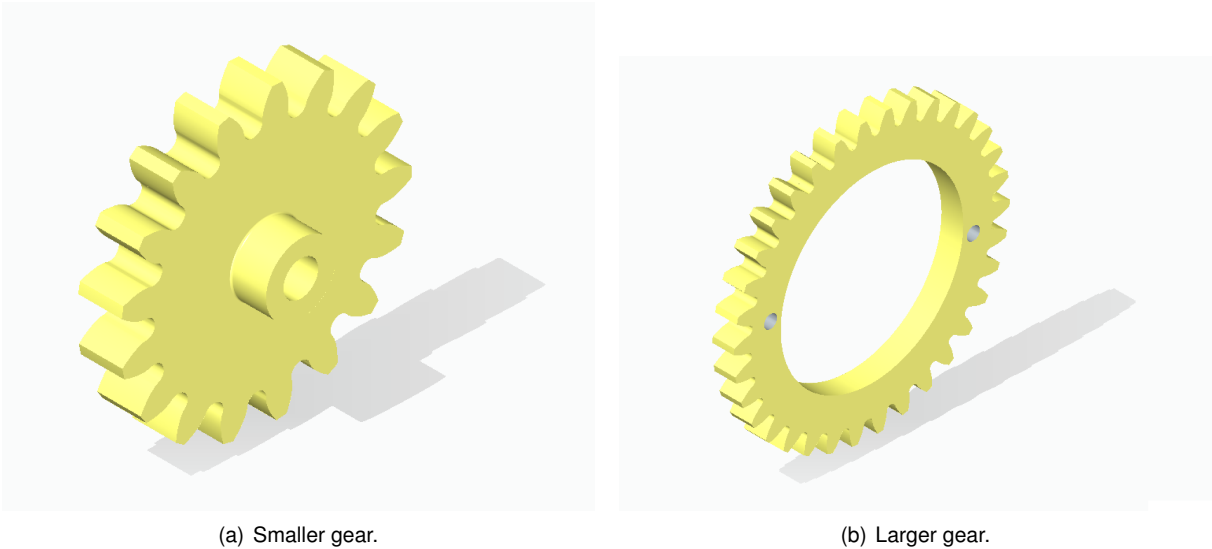


Figure 4.5: CAD of the gears.

4.5 Central Structure

The design of the central structure is of extreme importance to the prototype, since it is the element that will provide both stability and alignment to all other components. The pillar offers a static base where certain elements of the assembly can be fixed to. With that in mind, a solution was found where extensions are placed on the outside of the pillar, acting as bases for the motors. The offset between them is due to the size constraints within the prototype, therefore providing the best use of the available space. This is an obvious departure from what was initially drafted for concept epsilon back in section 3.7 with a flat disk serving as the platform to support both the motors and the discs. However, it was verified

that such a platform would not be necessary, with the option using these smaller extensions being much better both in terms of spent material and in usage of the available space. Of course, this leads to the motors being assembled perpendicularly to what was originally thought for the concept, which allows for the creation of the system of spur gears described in section 4.4.

Additionally, a portion of the pillar is to be made hollow, so that the necessary cables for the motors' operation can go through it, unimpeded by the movement of the discs. The middle section of the pillar has a larger diameter so that the ball bearings (that allow for a smooth rotation of the discs) can be properly attached. The motors' platforms are also built into the larger diameter section, in order to improve stability and resistance to bending moments. Lastly, the lower end of said pillar houses a support for a M12 hexagon nut, used to fix the prototype to the aerodynamic scale, a system that provides the additional advantage of being able to assemble the entirety of the prototype unimpeded by said scale.



Figure 4.6: 3D printed prototype's central structure.

4.6 Discs' Design

The discs' profile shape has already been determined in section 4.2, however, additional parameters need to be considered, both in terms of assembling the prototype and in terms of its overall efficiency.

Firstly, as would be expected, an opening on the centre of the discs is required to accommodate the pillar from the central structure described in section 4.5. The top disc does not require an opening due to the pillar, since it does not pierce through the disc. However, it does require an opening for the correct assembly of the ball bearings, therefore leading to the need of adding a lid, to minimize aerodynamic interference. Note that this system cannot be used on the bottom disc, due to the piercing central pillar. The lid works with a lock mechanism based on rotation: it is inserted and then rotated, fixing it in place during operation of the prototype. Any open gaps between the lid and the disc are then covered with

some Plasticine, to ensure a smooth surface.

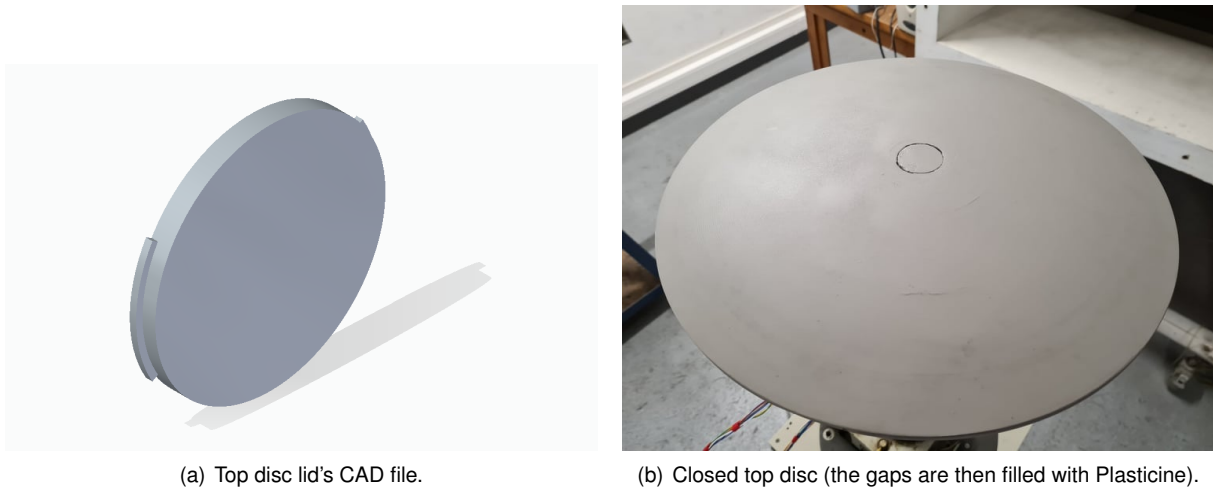


Figure 4.7: Lid system.

As mentioned previously, ball bearings are used to connect the rotating discs to the fixed central structure. As such, the discs require a tubular section leading to the centered opening, that will accommodate all of the required supports and cuts for the bearings and retaining rings used for that task, serving as a "casing" for those components. The "casing" of the top disc is also used to house the locking mechanism of the lid.

The specificity of the material used to print the gears, led to them being printed separately, meaning that a solution needed to be found to fix the larger gears onto the discs. The tubular structure mentioned previously offered a good base for them, so additional platforms were added for that purpose, with the gears being fixed to them with two screws each, as can be seen in figure 4.8.



Figure 4.8: Top disc's casing with larger gear assembled.

To guarantee structural integrity, four equally spaced ribs are placed on each of the discs. These

have the added benefit of acting as fins, facilitating the movement of the air trapped within the prototype. In order to not compromise the aerodynamic results, no cuts were made to the discs' surfaces with the purpose of cooling the interior of the prototype. Instead, the cooling system is based on convection with the air inside of the prototype: the motors are cooled with the moving air caused by the fins. As such, the increase of air movement will contribute to a more efficient heat transfer and therefore, a better cooling system.



Figure 4.9: One of the top disc's ribs.

One of the challenges of building this prototype is making sure that no air coming from the outside flow penetrates within the prototype itself: doing so could call into question the obtained aerodynamic results, since it could lead to the situation of two very close but separate wings, instead of the desired single wing with two rotating halves. However, one needs to keep in mind that PLA, the material used to print the discs, is susceptible to considerable deformations when exposed to very high temperatures as well as high levels of wear. These can be reached if the two discs were to get in contact with each other, considering the friction generated at the desired rotation speeds for the tests. As such, preventive measures should be applied to ensure that the discs refrain from touching each other, in order to preserve their shape and structural integrity. This translates into giving a small margin between both discs in the assembly, despite the fact that this will logically allow for a portion of the outside airflow to enter the prototype. To solve this issue, labyrinth-like "rails" are implemented near the edges of the discs: the idea is to force the air coming from the outside to go around several obstacles on its way to the inside of the prototype, losing its energy in the process, which should minimize the amount that effectively penetrates the prototype and practically nullify the amount that could exit on the opposite side of it.

An additional aspect to take into consideration is the fact that, due to possible inaccuracies in the manufacture of all different components, there can be oscillations on the discs that could put their edges into contact with one another. To minimize this effect, a tube is inserted into the "rail" of the bottom disc. The idea is to close the gap between both discs, effectively forcing them to be in permanent contact with one another along their periphery. In this way, not only will the discs have additional points of contact to

stabilize their rotation, the addition of the tube will also help in sealing the inside of the prototype from the incoming airflow.

This of course means that the material of the tube needs to be such that it ensures a minimum amount of friction, since it is designed to be a permanent point of contact between the discs. Additionally, it should allow the tube to be easily shaped into a circle of the required diameter. With these considerations in mind, Polytetrafluoroethylene (PTFE), commonly known as Teflon, was selected as the material to be used. Finally, to further decrease the friction between the discs, the top disc's rail was covered in lubricant grease.



Figure 4.10: Prototype with bottom disc assembled (note the Teflon tube near the periphery).

4.7 Discs' Material

An important parameter that should not be overlooked and is typically not considered in the early design phase, is the material of the elements of the prototype.

Due to the complex geometry of the four main elements of the prototype (central structure, bottom disc, top disc and lid), it was decided that these components would be manufactured with the use of 3D printing, since this method offers the best quality to cost (both in terms of time and money) ratio. With this method however, the choice of the material used for the printing filament becomes an additional parameter to be considered.

From the wide range of 3D printing materials, Acrylonitrile Butadiene Styrene (ABS) and PLA were considered, for their common availability and reduced cost. Both offer advantages and disadvantages depending on the application, as such their properties were analysed in order to verify which would be best for this particular project.

ABS was one of the first plastics to be used in industrial 3D printing, remaining a very popular material to this day, mainly due to its toughness and impact resistance, making it ideal for applications in parts where extra usage and wear (such as LEGO bricks, for example) are expected [36]. Additionally, this material has a relatively high glass transition temperature of 105 °C [12], meaning that it can withstand applications with a considerable amount of heat without deforming.

The most considerable disadvantage of this material is associated to its printing. ABS requires a high printing temperature, which can be provided by more complex printers that include heated beds. Because of this, the material tends to warp when it is being cooled, which might lead to dimensional inaccuracies [36].

On the other hand, PLA is one of the most popular materials used in desktop 3D printing, since it is inexpensive, easy to print, and creates parts with a large range of applications [37]. It has a similar tensile strength to ABS however, it is clearly inferior in terms of flexural strength and elongation before breaking [12], as can be seen in table 4.4.

Property	ABS	PLA
Tensile strength	27 MPa	37 MPa
Elongation	3.5 - 50%	6%
Flexural modulus	2.1 - 7.6 GPa	4 GPa
Glass transition temperature	105 °C	60 °C

Table 4.4: Properties of ABS and PLA [12].

Despite that fact, PLA's main disadvantage of interest to this project is its lower glass transition temperature of 60 °C, which is reflected in a lower heat resistance for any parts printed with this material. As such, PLA tends to lose its structural integrity and begins to deform, as it approaches that temperature. However, this also means that the printing temperature for this material is significantly lower, when compared to the ABS's one, which leads to less warping and better dimensional accuracy, if the parts are properly cooled [12].

At first glance, ABS seems to be the better option between the two, since it offers the better mechanical properties and heat resistance. However, the size of the discs means that the warping effect, associated to the printing of this material, cannot be neglected. After all, the objective of this work is to analyse the aerodynamic performance of the prototype: discs with poor dimensional accuracy and overall poor surface quality, would certainly compromise the obtained results.

As such, the decision was made to use the two materials to print different parts of the prototype. For its better dimensional accuracy and ease of printing, PLA was chosen as the material for the two discs and the top disc's lid. For its better mechanical properties and especially for its increased heat

resistance, ABS was selected as the material for the central structure, since it will be in direct contact with the two motors, which raises significant mechanical and thermal concerns.

Chapter 5

Testing the Prototype

With the prototype fully constructed, it is time to test it in the wind tunnel. In the present chapter, the experimental assembly is showcased and the testing process is described. The obtained results are presented in plot format as well as in flow visualization images. An analysis of the results is performed at the end of the chapter.

5.1 Wind Tunnel Assembly

The testing of the prototype was done in the open circuit wind tunnel, located at the Mechanical Engineering Department of Instituto Superior Técnico. The tunnel operates with an incompressible flow that can reach a maximum of approximately $10 \text{ m}\cdot\text{s}^{-1}$ at the location of the prototype. A centrifugal fan installed at the entrance of the experimental assembly, activated by a Direct Current (DC) motor, provides the required airflow. Prior to the test section, a stabilization chamber exists within the tunnel, which possesses a series of nets and honeycomb structures, as well as a converging section with an area ratio of 3:1, all with the objective of ensuring a good quality on the incoming airflow, which should be uniform and with low turbulence. All of the tests were performed in a free flow coming from a section of $135 \times 80 \text{ cm}^2$ with a release to the atmosphere.

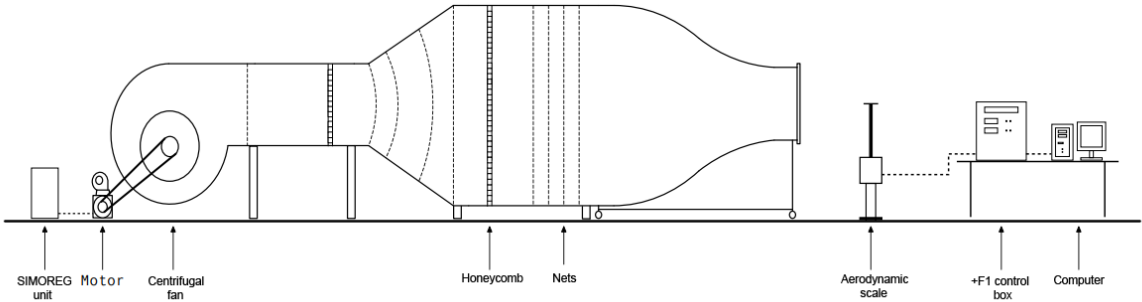


Figure 5.1: Wind tunnel assembly schematic.

To obtain the required measurements of aerodynamic loads on the prototype, an aerodynamic scale is included in the experimental assembly. It includes 6 load cells (HBM-Z6), which allow for the measurement of forces along three axes, as well as their respective moments, in addition to 2 Harmonic Drive Systems' high accuracy servomotors, allowing for a precise control of both AoA and yaw of any given model fixed to the scale. The yaw control was not used in the performed tests, since the axially symmetric nature of the prototype makes it redundant.

All loads are considered positive according to the axes system represented in figure 5.2.

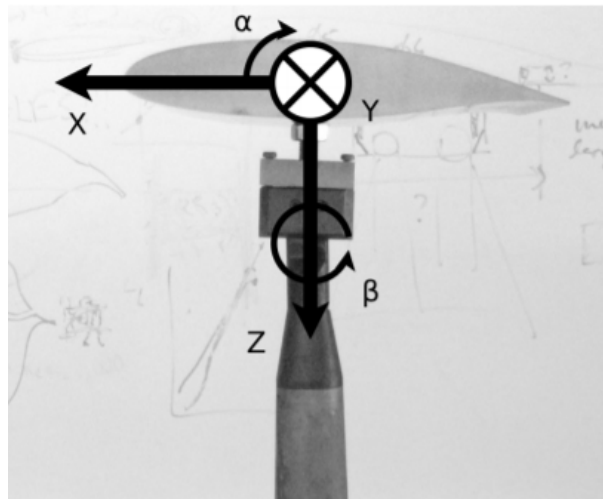


Figure 5.2: Axes system of the aerodynamic scale [34].

The aerodynamic scale's system has an horizontal xy plane, with the z axis aligned with the base and positive in the downwards direction. The x axis is positive in the opposite direction as the incoming airflow. Lastly, the AoA turns around the y axis, being positive according to the right hand rule (represented by α in figure 5.2).

The limiting values of the aerodynamic scale, for the relevant loads and moments are presented in table 5.1.

Drag	30 N
Lift	-20+50 N
Roll moment	± 5 N.m
Pitching moment	± 5 N.m
Yaw moment	± 5 N.m
AoA	$\pm 30^\circ$

Table 5.1: Limiting values of the aerodynamic scale.

All loads and angles are measured by the +F1 control box, which includes a PREMA 5001 multimeter for an analog-digital conversion, so that the values can be transmitted to a Personal Computer (PC) and allow the control of the motors to be done through it.

The airflow is ensured by a centrifugal fan, which is activated by a DC motor Thrige-Titan Lak 160 LA, with a nominal power of 21.5 kW and a nominal angular speed of 2280 rpm, controlled by Siemens' microprocessor-based converter SIMOREG DC-Master 6RA70, both installed aft of the wind tunnel. The speed value is displayed in revolutions per minute on a screen at the SIMOREG unit. The control of this speed can be done through the "AeroIST" program, installed on the PC present in the assembly, being presented in terms of a percentage of the motor's nominal speed.

The measurement of the atmospheric air temperature is performed using a Schneider Electric's AP9512BLK temperature sensor, installed near the exit of the converging section of the tunnel. These values can only be read when displayed on the program mentioned previously. The range of measurements goes from 0 °C to 33.9 °C, with a resolution of 0.033 °C, according to the manufacturer.

As for the pressure differences, they are measured using a Furness Controls Limited's FCO12 micromanometer, which has limits of ± 199.9 mmH₂O and a maximum accuracy of 1%. Typically, this instrument is connected to the total pressure tube installed on the wind tunnel and to the collector of static pressure of the test section, which is the same as the atmospheric pressure in free flow tests. The dynamic pressure can then be calculated through the difference of both values, which allows for the undisturbed flow speed on the tunnel to be determined. The resolution of the system that obtains the dynamic pressure is ± 0.019 mmH₂O. Before each test, one should zero the micromanometer to ensure an accurate display of the dynamic pressure. To do so, the integration time should be changed to its minimum, using the proper knob on the device. Then, the "zero" knob should be adjusted until a zero is indicated on the digital display. Finally, the integration time should be readjusted for a better reading of the values, being possible to regulate it from 20 ms to 10 s. Of note is the fact that the dynamic pressure is also displayed on the "AeroIST" program, with the values shown there being the ones used on the data analysis. As such the value indicated on the micromanometer's display was used simply to check if the dynamic pressure was being correctly calculated.

5.2 AeroIST

In order to record the values obtained from the aerodynamic scale, a user interface is present on the PC of the wind tunnel assembly in the form of the "AeroIST" program, developed by Roque as part of his Master's thesis [34].

To begin, the user should setup a reference, a process which is equivalent to taring the scale. The AoA, percentage of the nominal speed of the wind tunnel's motor (which corresponds to the incoming airflow speed) and multimeter integration time (corresponding to the time taken to obtain the data from a single load cell) can all be adjusted at this stage, to better suit the measurements that will be made

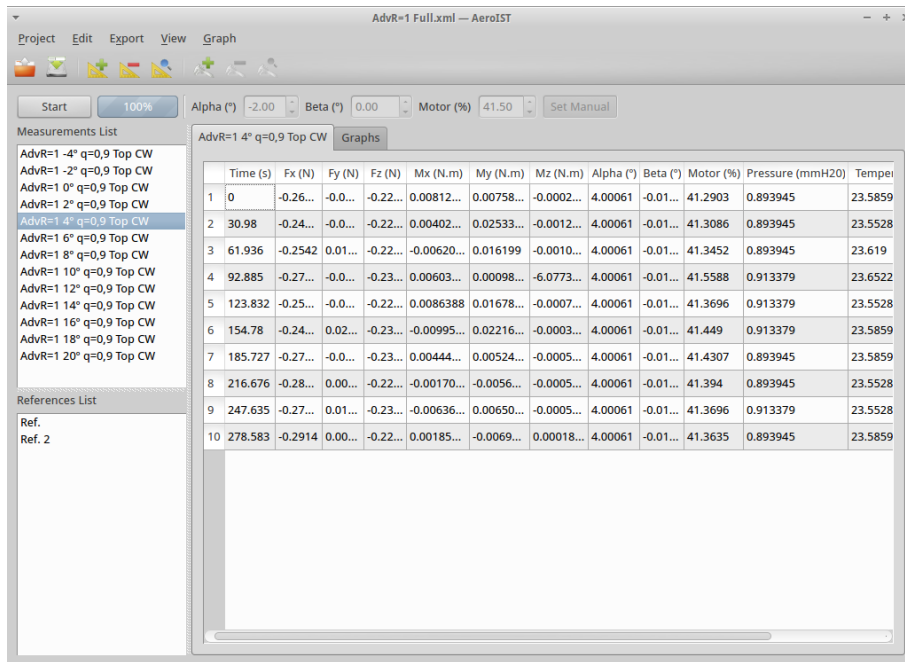


Figure 5.3: AeroIST's graphical user interface.

following this process. Additionally, the number of measurements to be done during the reference acquisition can also be selected, which is useful for accuracy purposes. Once the variables are selected and the reference menu is exited, the program automatically begins the measuring process, presenting the values of the forces and moments relative to all three coordinate axes in a table on the user interface.

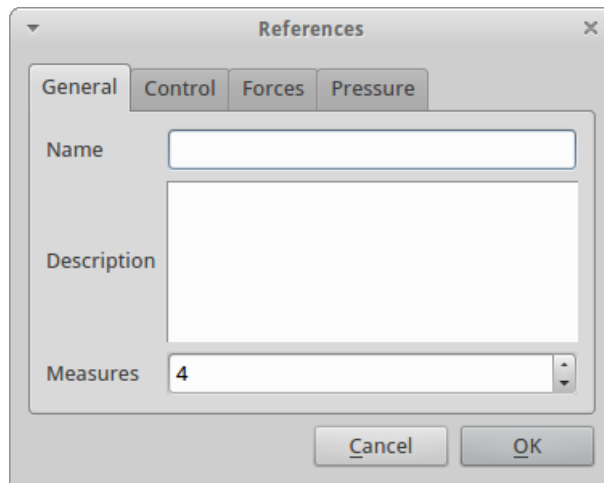


Figure 5.4: Reference menu.

With a performed reference the user can then proceed to the setup of the actual measurements. On the appropriate menu, the user can once again select the desired AoA and percentage of the nominal speed of the wind tunnel's motor, with an added option to do a "sweep" of measurements that cover a certain interval of these variables with a step determined by the user. In this case, the program automatically performs one iteration for each desired value of one of these variables.

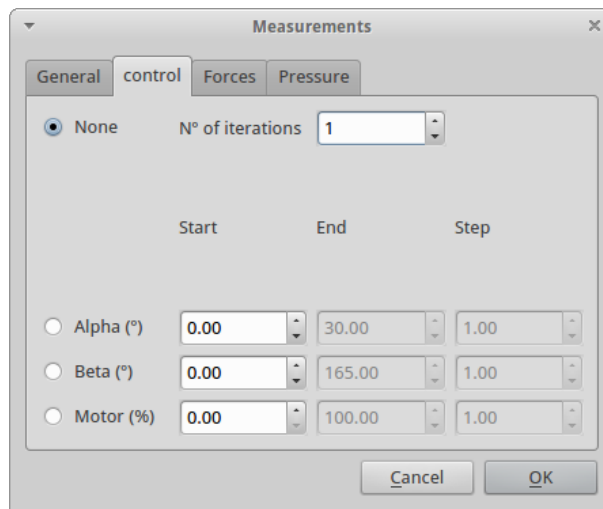


Figure 5.5: Section of the measurement menu where the iterations can be defined.

It is then important to define the concepts of measurement and iteration in the context of "AeroIST". A measurement is understood as the acquisition of the data from all 6 load cells present in the scale. The time required for each measurement is dependent on the multimeter integration time, selected by the user, since the control box measures each of the load cells individually and in a sequential manner, only proceeding to the following cell once the multimeter completes the integration of the current one. Similarly to the reference menu, the user can once again determine the integration time for the multimeter. When all 6 values have been integrated the measurement is displayed in a table on the user interface. On the other hand, an iteration is simply understood as a group of measurements where no variables are changed. As such, the measurement menu includes an option to select the number of measurements to be done for each iteration, as well as an option to manually select the desired number of iterations.

A final variable present in the measurement menu is the "settling time". This is simply the time that the program should consider to be in between iterations, since in this period some changes might have been introduced to the system which require time to "settle" and as such the program should wait before starting the measuring process of the following iteration.

With the setup process complete, the user can then press the "Start" button to commence the measuring process. The measurements are displayed on the user interface as soon as they are complete (i.e. as soon as the control box goes through all 6 load cells), which include the 6 forces and moments, the air temperature measured by the sensor in the assembly, the percentage of the nominal speed of the wind tunnel's motor, and the dynamic pressure, measured by the micromanometer also in the assembly. This last value is of particular importance, since it is the only way to confirm the actual incoming airflow speed during the tests.

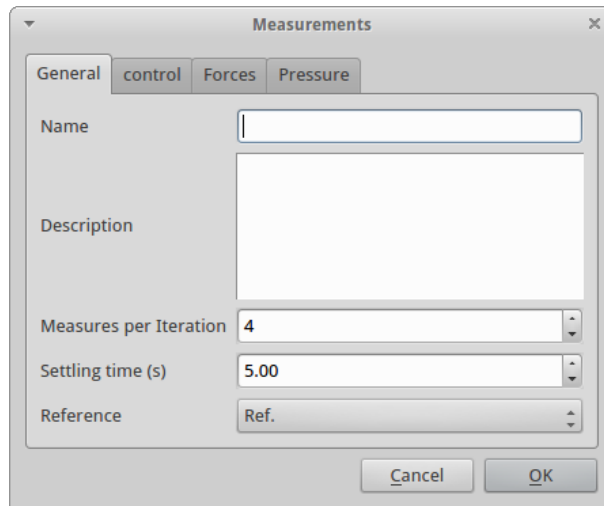


Figure 5.6: Section of the measurement menu where the settling time can be set.

The process is automatically stopped once all iterations are performed and the data can then be saved into a Comma-Separated Values (CSV) file, to then be properly analysed on a spreadsheet program.

5.3 Motors' Control and Operation

In order to control and operate the two EC 45 flat motors within the prototype, an electrical assembly (which is showcased in figure 5.7) needs to be implemented. In it, two Maxon's ESCON 50/5 controllers are included, one for each of the motors. These will be responsible for transmitting the electrical power from the source to the motors as well as making them rotate at the desired speeds and directions. The programming of the controllers is done entirely through Maxon's own software, ESCON Studio, by connecting them to a PC via a Universal Serial Bus (USB) cable. In it, a desired speed can be specified as well as a speed ramp, which controls the time that it takes for the motor to reach said speed, something that is important to keep at a moderate value, in order to prevent damaging the prototype. The direction of rotation can also be programmed from the software, each one being assigned one of the input ports at the "Digital I/O" section of the controllers: in this way the direction can easily be selected by connecting the power output of the mentioned section to the desired input port, without the need to reprogram the controller through the software.

The fact that the motors have a flex-print type cable adds a problem, since this type is not supported by the controllers. As such, two Flex-Print Connector to Printed Circuit Board-screw clamps adapters were acquired, to allow for the connection of the motors to the controllers. This brought the added benefit of extending the length of the cables, which is quite useful in the overall assembly.



(a) Full test setup.



(b) ESCON 50/5 controllers close-up.

Figure 5.7: Electrical assembly.

5.4 Hall Sensor Calibration

In this study, the speed at which the discs are rotating is a crucial value to be controlled. As such, it is critical that the process of acquiring said value is as precise as possible, enabling an accurate capture of the remaining data.

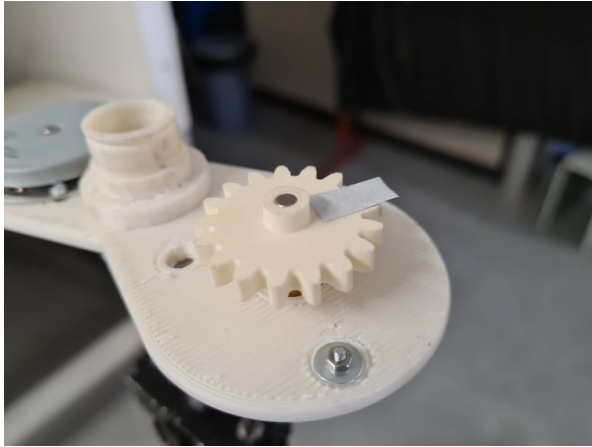
The selected motors have Hall sensors incorporated into them, which allows for the measurement of the rotation speed. This speed can then be visualized through the "Data Recorder" tool in ESCON Studio. However, as was mentioned previously, it is crucial that the value seen on the software is accurate to the actual rotation speed of the discs.

In order to verify this, calibration tests were performed using the "Photo" function of a digital tachometer. To measure the speed, a reflective mark needs to be applied on the surface of the object, which will act as a target. By pressing the measuring button, a light beam is emitted from the tachometer, which should be directed towards a fixed area where the reflective mark will pass through. The tachometer is capable of detecting the reflected light from the mark, and using the frequency of its occurrence, is capable of calculating the rotation speed of the object.

For the tests, two objects were measured: one of the small gears ⁴, directly coupled to the motor's shaft, and one of the discs, which should present half of the motor's speed due to the gears' transmission ratio that is used. Several speeds were tested, with the values being measured by both the tachometer and ESCON Studio. These can be seen in tables 5.2 and 5.3.

For the test on the small gear, the tachometer consistently measured the exact speed that was input into the controller. ESCON Studio was not as precise in obtaining these values, presenting an average

⁴For the measurement of the small gear, the disc was not attached to the motor i.e. only the motor and the gear were present in the assembly



(a) Reflective mark on one of the small gears.



(b) Reflective mark on the top disc.

Figure 5.8: Calibration setup.

Input speed (rpm)	ESCON Studio (rpm)	Tachometer (rpm)
100	100.2	100
250	249	250
500	499.6	500
1000	999.5	1000
1500	1498.6	1500
2000	1997.8	2000
2500	2497.5	2500

Table 5.2: Speed calibration test for the small gear.

relative error to the input value of 0.15%. However, this does prove that the values presented by ESCON's Software are reliable for the measurement of the small gear, as well as the fact that the motor rotates at the desired speed when no disc is attached to it.

Input speed (rpm)	ESCON Studio (rpm)	Tachometer (rpm)
100	101.5	50
250	250.5	125
500	501.5	250
750	749.5	375
1000	1000	499.9

Table 5.3: Speed calibration test for the disc.

For the test on the disc, it can be seen that the tachometer correctly measured the expected speed of the disc. Given the results of the previous test, it would be predictable that ESCON Studio would be, once again, not as precise in obtaining the values. This was indeed verified, with the software presenting an average relative error to the input value of 0.41%.

This relative error is still perfectly reasonable, but it is clearly larger than the one from the small gear

test. This is likely due to the oscillations that are present once the disc is added into the assembly, which force the controller to perform more corrections in order to maintain the desired speed, leading to a more erratic speed reading. These oscillations are an outcome of the fact that, unfortunately, the dimensional accuracy required was not met in every part of the prototype, particularly in the printing of the central structure.

Of note is the fact that the input speed range for the second calibration case does not go faster than 1000 rpm. This is due to the aforementioned oscillations: these will add an unexpected increase of loads in the system, which will increase the amount of torque required of the motor. Since this is limited by its available power of 12 W, the achievable rotation speed becomes smaller than what was initially expected. It was seen that under a specific setup of the assembly (which will be explored in the following section), the discs could reach faster rotation speeds, but for all other configurations the maximum allowable speed was always approximately 1000 rpm.

With the calibration performed, the wind tunnel tests can be executed with confidence that the rotation speed of the discs is being accurately measured by ESCON Studio.

5.5 Wind Tunnel Corrections

Given the experimental nature of this work, there will be unwanted influences from several components on the obtained results. However, these elements are all necessary to perform the tests, as such their influence simply needs to be quantified so that the results can be correctly presented. One such element is the vertical support that connects the prototype to the aerodynamic scale, necessary to ensure that the prototype is correctly positioned within the wind tunnel's jet stream, as can be seen in figure 5.9.

To quantify its influence, a test is performed at a Reynolds number of $Re = 100000$ (the same value that will be used throughout the testing process) with only the vertical support present in the assembly. The average values of the relevant aerodynamic loads were compiled and then converted into their respective aerodynamic coefficients, with these being presented in table 5.4. These values are then subtracted to the ones obtained during the tests, so that the final results are free from the influence of the vertical support.

Lift coefficient (C_L)	0.07
Drag coefficient (C_D)	0.20
Pitching moment coefficient (C_m)	-0.18
Roll moment coefficient (C_ϕ)	0
Yaw moment coefficient (C_ψ)	0.01

Table 5.4: Aerodynamic coefficients associated to the vertical support.



Figure 5.9: Aerodynamic scale assembly, the vertical support can be seen connecting the prototype (top) to the scale (bottom).

Delgado [8] performed a detailed study on the experimental error associated to the open section of the wind tunnel. His findings suggest a correction dependant on the aspect ratio of the wing which leads to an increase on all lift-dependent coefficients (which includes pitching and roll moments), based on a comparison between experimentally obtained results and theoretical values obtained from the "lifting-line theory". Since his study included the correction values to be applied on cases of an aspect ratio of 1 and 2 (recalling this prototype has an aspect ratio approximately equal to 1.27), a linear interpolation can be used to determine that an increase of 16.3% needs to be applied on all lift-dependent coefficients results, in order to correct them.

5.6 Wind Tunnel Tests

Another important parameter to define before beginning the tests is the Reynolds number at which they will occur. The objective should be to maximise the range of $AdvR$ to be tested, since the rotation of the discs is the main feature of the prototype, therefore being interesting to see how the different $AdvR$ values impact the aerodynamic variables. This can be achieved in two ways: increase the rotation speed of the discs and decrease the incoming airflow speed. As was noted on section 5.4, the motors are more limited in terms of their maximum speed than originally thought. Additionally, operating the motors at their maximum capacity for extended periods of time could damage the entire prototype. To prevent such

issues, it was decided to minimize the incoming airflow speed (and therefore the Reynolds number⁵), so that the maximum AdvR could be reached with the motors operating in a reasonable window. The number was then set as $Re = 100000$.

As was already mentioned, the incoming airflow speed control is in reality done through the value of dynamic pressure. As such, a quick program was developed on a spreadsheet software in order to obtain this required value, using as input variables the Reynolds number and the air temperature. The program is also designed to calculate the required rotation speed of the motors, if the desired AdvR value is input.

The program converts the input temperature from degrees Celsius to degrees Kelvin and then uses Sutherland's law:

$$\mu = \mu_0 \left(\frac{T}{T_0} \right)^{1.5} \frac{T_0 + 111}{T + 111}, \quad (5.1)$$

where $\mu_0 = 1.716 \times 10^{-5} \text{ kg.m}^{-1}.\text{s}^{-1}$ and $T_0 = 273.15 \text{ K}$, to obtain the value of dynamic viscosity, μ .

Assuming that the room where the tests are performed is at an approximate altitude of 100 m in relation to sea-level, the pressure in the room can be estimated to be $p \approx 100129 \text{ Pa}$. Using it with the ideal gas law,

$$p = R\rho T \Leftrightarrow \rho_{air} = \frac{p}{RT}, \quad (5.2)$$

where $R = 287 \text{ J.kg}^{-1}.\text{K}^{-1}$, can be used to calculate the air density, ρ_{air} .

With these values, together with the Reynolds number definition

$$Re = \frac{\rho_{air} U_{\infty} c}{\mu} \Leftrightarrow U_{\infty} = \frac{Re \mu}{\rho_{air} c}, \quad (5.3)$$

where $c = 0.4 \text{ m}$ (the chord of the prototype and the characteristic length of this case), the desired incoming airflow speed can be obtained.

Knowing this value, the program can then convert it into a desired dynamic pressure using

$$q = \frac{1}{2} \rho_{air} U_{\infty}^2, \quad (5.4)$$

as well as use the definition of the AdvR alongside the gear ratio present in the prototype to obtain the required rotation speed of the motors.

⁵Defined here as seen in equation 5.3 unlike the definition used in section 4.3

5.6.1 Stability Tests

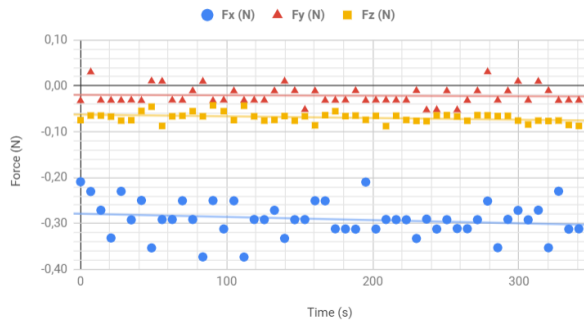
Initially, a set of measurements needed to be performed in order to determine the best integration time to be used on the multimeter. Roque describes that the obtained results are more stable if a larger integration time is used [34], however it is important to note that the geometry used for those tests is quite different from the prototype of this thesis, which warrants further investigation on which of the larger integration times should be used on this case.

Another parameter that needs to be taken into consideration is the total time of the tests, or in other words, the product of the integration time across all 6 load cells with the number of measurements. Since each point of the relevant plots is going to be obtained through the average of the measurements on each of the tests, it is crucial that this total test time allows for the acquisition of enough values that will allow for an accurate averaged point, even with some measurement oscillations taken into consideration.

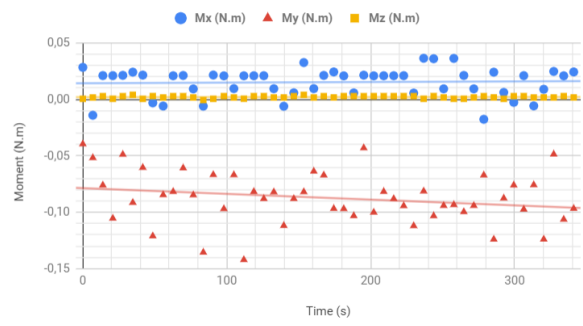
However, that raises concerns in terms of the operation of the prototype. As was mentioned in previous sections, this is a design that is not optimized for the cooling of the motors. That, together with the unexpected decrease of mechanical performance of several components of the built prototype (which can be visually verified by the oscillations of the discs), means that there is a very realistic possibility of the prototype being critically damaged if it is in continuous operation for extended periods of time. As such, a compromise needs to be made: the integration time needs to be one that allows stable and accurate results to be obtained within a total test time that does not compromise the operation of the prototype.

A total time of around 5 minutes was deemed acceptable for the tests, with the choice of integration time falling between 1, 5 and 10 seconds, corresponding to a total of 50, 10 and 5 measurements respectively. Given that the profile of the prototype is symmetric, from theory it is expected to not generate any lift force if it is at an $AoA=0^\circ$. As such, this AoA is the most likely to produce stable results and so it was the one used for these measurements. The Reynolds number of the incoming airflow was kept at the same value to be used in further tests: $Re = 100000$. The results of these tests were converted into plots, which are presented in figures 5.10, 5.11 and 5.12.

Something of note is the fact that the total time of these tests varied for each of the integration times. What is seen is that the smaller that integration time is, the longer the complete test actually takes, despite the fact that all tests were prepared to have a duration of 5 minutes each, based on the integration time and number of measurements. This is in accordance with the findings of Roque, who stated that the reason for this is due to the time the control box takes to end one measurement and begin a new one. In essence, this change is not instantaneous and will add to the overall time of the test. Given how for smaller integration times, the number of measurements needs to be increased in order to reach the desired test time of 5 minutes, this implies that more changes will occur and therefore more time will be added to the expected total.

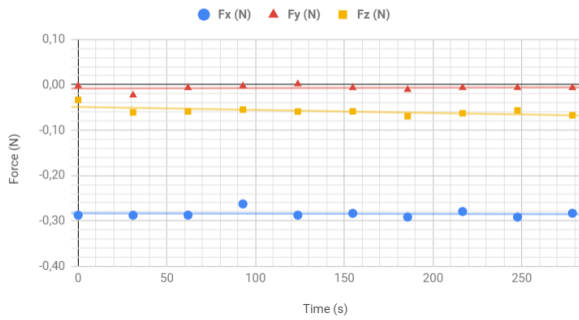


(a) Aerodynamic Forces.

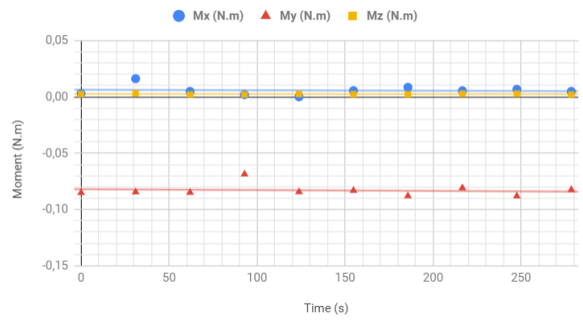


(b) Aerodynamic Moments.

Figure 5.10: Stability analysis for a multimeter integration time of 1 second.

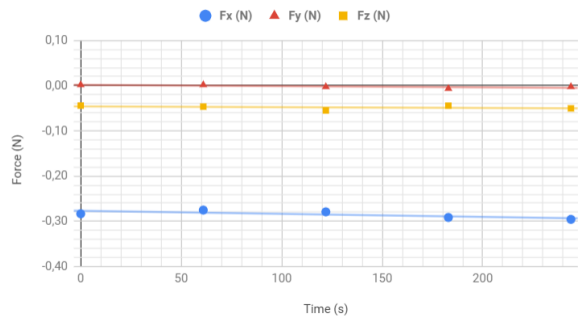


(a) Aerodynamic Forces.

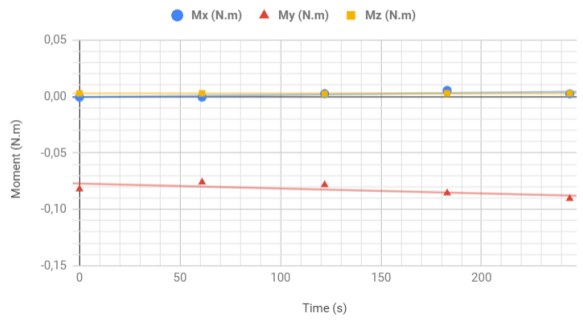


(b) Aerodynamic Moments.

Figure 5.11: Stability analysis for a multimeter integration time of 5 seconds.



(a) Aerodynamic Forces.



(b) Aerodynamic Moments.

Figure 5.12: Stability analysis for a multimeter integration time of 10 seconds.

Analysing the obtained plots, it becomes clear that the integration time of 1 second should be avoided: despite the fact that, on average, most results are acceptably stable (the forces in the y and z directions, corresponding to the side-force and lift, as well as the moments in the x and z directions, corresponding to the rolling and yaw moments) as can be seen by the approximate horizontal slopes of the trendlines, the remaining variables have considerable oscillations between the obtained points in addition to not presenting horizontal trendlines.

In contrast, for the remaining integration times, the oscillations between obtained points are far less noticeable. Curiously, the analysis shows that there is not a significant difference between the cases

of 5 and 10 seconds: both present horizontal trendlines for most variables, indicating a stable result on average (as was already mentioned), with a couple of variables presenting trendlines with slightly negative slopes.

For an integration time of 5 seconds, the force in the z direction and the moment in the y direction, corresponding to the pitching moment, present non-horizontal trendlines. As for an integration time of 10 seconds, the variables that present a non-horizontal slope are the force in the x direction, corresponding to drag, and the moment in the y direction, as in the previous case.

Comparing between the two times, the stability of the aerodynamic forces seems quite similar, however, the integration time of 5 seconds clearly presents more stable results for the aerodynamic moments. Despite this, it is important to note that these stability tests were performed without rotation on the discs. What was later verified is that the choice of integration time should be adapted depending on the AdvR used, however, either 5 or 10 seconds were always chosen.

5.6.2 Quantification of Uncertainties

Any experimental study is expected to have errors associated to its results, based on the techniques and instruments used in the measurement process. After all, independently of how accurate an instrument is claimed to be, a realistic experimental setup is never going to be able to replicate an ideal one: there are simply too many uncontrollable variables in the real world that prevent us from achieving the same conditions that can be obtained in a theoretical or computational study. As such, an analysis of the uncertainties associated to the experimental study is crucial to ensure a correct assessment of any results that are obtained.

The uncertainty, Q , is then a representation of the experimental error, or in other words, the difference between the experimentally obtained values and the real ones, which are unknown. The quantification of the uncertainties should yield an interval defined as $\pm Q$, around the average value of each aerodynamic coefficient.

For this study, a procedure based on a Taylor Series Method is used, as described by Coleman and Steele [7]. Firstly, it is important to determine which variables used to obtain the coefficients are susceptible to uncertainties. Every force coefficient can be generally defined as

$$C_F = \frac{F}{q A} = \frac{F}{q \frac{\pi}{4} c^2}, \quad (5.5)$$

and every moment coefficient as

$$C_M = \frac{M}{q A c} = \frac{M}{q \frac{\pi}{4} c^3}, \quad (5.6)$$

where F and M are a generic aerodynamic force and moment respectively, q is the dynamic pressure, A is the planform area of the prototype (which is simply the area of a circle) and c is the chord of the prototype.

The uncertainties are then classified as systematic (represented by b) or random (represented as s), where the former are defined as uncertainties that remain constant throughout the entirety of the testing process, and the latter defined as uncertainties that, due to the influence of certain unpredictable factors, can change throughout the tests. Based on equations 5.5 and 5.6, it can be seen that there are four variables to classify: F , M , q and c .

The uncertainty associated to the chord of the prototype, b_c , can be considered as systematic, since it remains constant as the chord is only measured once with a ruler. The uncertainty is then considered to be half of the smallest scale division in the ruler, ± 0.5 mm. The remaining uncertainties can be classified as random, since they will be subject to different factors such as shifts in temperature and vibrations induced by the rotation of the discs, which prevents them from remaining constant throughout the testing process. Their values can be obtained with the standard deviation of the respective measurements in any given test, defined as

$$s = \sqrt{\frac{\sum_{i=1}^{\infty} (x_i - \bar{x})^2}{n}}, \quad (5.7)$$

where x_i is an individual measurement, \bar{x} is the average of the measurements and n the number of measurements.

To calculate these random uncertainties, the results obtained from the stability tests presented in subsection 5.6.1 are used. As will be seen in further sections, the multimeter integration time was set at 5 seconds for lower AdvR and 10 seconds for higher AdvR. The necessary results to the uncertainty analysis are summarized in tables 5.5 and 5.6:

Variable	Average value	Standard deviation
F_x (N)	-0.2841	0.0084
F_z (N)	-0.0581	0.0099
M_x (N.m)	0.0057	0.0044
M_y (N.m)	-0.0830	0.0055
M_z (N.m)	0.0025	0.0004
q (Pa)	8.9573	0 ⁶

Table 5.5: Results for an integration time of 5 seconds.

Notice how the information regarding the dynamic pressure is the same on both tables, with a standard deviation equal to zero for this variable. This is likely due to the fact that the stability tests were performed at the end of a testing day (meaning that the wind tunnel had been in operation for long

⁶Approximation to zero, standard deviation in stability tests is extremely small.

enough to provide an approximately steady flow), as well as the fact that these tests take a considerably smaller time to complete, which reduces the chances for a change in dynamic pressure to register. This however, does not mean that there is no uncertainty associated to the dynamic pressure: in fact, that uncertainty was verified throughout the testing process, when larger number of measurements were made. Instead, the conclusion that can be drawn is that the random uncertainty of the dynamic pressure is simply too small to be noticeable on the baseline tests and thus is assumed to be zero in the calculations to obtain the overall uncertainty of the aerodynamic coefficients.

Variable	Average value	Standard deviation
F_x (N)	-0.2849	0.0085
F_z (N)	-0.0479	0.0046
M_x (N.m)	0.0018	0.0025
M_y (N.m)	-0.0825	0.0058
M_z (N.m)	0.0027	0.0002
q (Pa)	8.9573	0 ⁷

Table 5.6: Results for an integration time of 10 seconds.

We now have all of the necessary information to calculate the uncertainty of each of the relevant aerodynamic coefficients. Firstly, the systematic uncertainty for the force coefficients, b_F , can be obtained from:

$$b_F^2 = \left(\frac{\partial C_F}{\partial c} b_c \right)^2 \Leftrightarrow b_F = \pm \sqrt{\left(-\frac{8 F}{q \pi c^3} b_c \right)^2}, \quad (5.8)$$

with the systematic uncertainty for the moment coefficients, b_M , obtainable from:

$$b_M^2 = \left(\frac{\partial C_M}{\partial c} b_c \right)^2 \Leftrightarrow b_M = \pm \sqrt{\left(-\frac{12 M}{q \pi c^4} b_c \right)^2}. \quad (5.9)$$

The variables in equations 5.8 and 5.9 are then replaced by the measured value, in the case of c (a value of 401 mm was obtained), and by the average value of the measurements, for F , M and q . The obtained uncertainties are displayed in table 5.7:

Systematic uncertainty	5 seconds	10 seconds
b_{C_D}	0.000626	0.000628
b_{C_L}	0.000128	0.000106
b_{C_ϕ}	0.000047	0.000015
b_{C_m}	0.000684	0.000680
b_{C_ψ}	0.000021	0.000022

Table 5.7: Results for systematic uncertainties for both multimeter integration times.

As for the random uncertainty of either force or moment coefficients, s_{C_X} , it can be simply obtained

⁷See footnote 6.

from the random uncertainties (i.e. the standard deviation values) of the aerodynamic force or moment, s_X , and dynamic pressure, s_q , as

$$s_{C_X} = \sqrt{s_X^2 + s_q^2}. \quad (5.10)$$

The obtained values are presented in table 5.8:

Random uncertainty	5 seconds	10 seconds
s_{C_D}	0.0084	0.0085
s_{C_L}	0.0099	0.0046
s_{C_ϕ}	0.0044	0.0025
s_{C_m}	0.0055	0.0058
s_{C_ψ}	0.0004	0.0002

Table 5.8: Results for random uncertainties for both multimeter integration times.

The final uncertainty value of each of the coefficients, I_{C_X} , with a confidence level of 95%⁸, can be obtained from

$$I_{C_X} = 2 \sqrt{b_{C_X}^2 + s_{C_X}^2}, \quad (5.11)$$

with the obtained values presented in table 5.9:

Uncertainty	5 seconds	10 seconds
I_{C_D}	± 0.0168	± 0.0170
I_{C_L}	± 0.0198	± 0.0092
I_{C_ϕ}	± 0.0088	± 0.0050
I_{C_m}	± 0.0111	± 0.0117
I_{C_ψ}	± 0.0008	± 0.0004

Table 5.9: Results for the final uncertainties for both multimeter integration times.

5.6.3 Synchronous Rotation Tests

Following the stability tests, the focus was shifted to the scenario where both discs are rotating at the same speed and in the same direction, in this case a clockwise rotation when seen from above.

The fact that both discs in this scenario are essentially not independent from one another presented an opportunity to increase the angular velocity that can be reached. As was mentioned in section 5.4, a smaller than expected maximum rotation speed was verified during the calibration process, which can be detrimental to this work, since it is of interest to test as wide of a range of AdvR as possible. However, the calibration was performed with a single disc on the assembly. What was later verified is that the addition of the second disc increases the stability of the system, if both discs rotate synchronously.

⁸Meaning that in 100 measurements, the real value is expected to be located within the determined interval 95 times.

As such, and in order to minimize any sort of oscillations between the two discs, some adhesive tape was used to fix them together, effectively making them a single unit which can then be set into motion by a single motor.

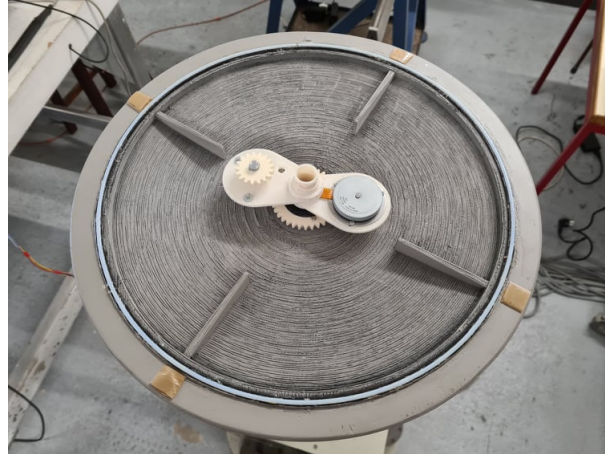


Figure 5.13: Bottom disc with adhesive tape along its periphery.

Despite the fact that only one of the motors was used for these tests⁹, the minimization of the discs' oscillations resulted in higher achievable rotation speeds. This allowed for tests to be performed up to an AdvR equal to 4.

During the testing process, it was noticed that the results between the different AdvR did not have any consistency. Additionally, when repeating tests for the same AdvR, the obtained values could vary significantly, despite the fact that the flow conditions were kept constant in all tests, through the control of the dynamic pressure of the airflow. To clarify, for a specific AdvR, the gap between values at different AoA remained approximately constant, the change was only reflected in the values themselves.

As such, "baseline" tests were performed. The problem seemed to arise from the fact that the wind tunnel would stop in-between changes of AoA, to allow for the motor to properly cool down, preventing it from being in continuous operation for too long. However, this prevents the wind tunnel from achieving a properly steady state, which could have an impact on the measured results.

The "baseline" tests consisted in selecting four AoA (represented by the greek letter alpha, α) across the tested range (in this case: 2° , 6° , 14° and 18°) and testing them individually for the different AdvR. So as an example, the AoA is first fixed at 2° . The wind tunnel is then setup to run several iterations without stopping: each iteration still runs for approximately 5 minutes and will correspond to each of the tested AdvR. The "settling time" is adjusted to allow for the airflow to stabilize between iterations, as the rotation speed of the discs is progressively increased. With the iterations complete, the AoA is increased and the process is repeated for the remaining three angles.

⁹The synchronization between both motors proved to be difficult to achieve and ultimately not necessary.

Logically, this means that in this method the motor is pushed to its limit, with a continuous operation time of well over 5 minutes, so these tests were moved to the end of the list to ensure that, even if something did go wrong, there was still available data that could be analysed.

Despite their risk, the values obtained from these tests contributed to adjusting the already obtained values, since they provided the expected "gap" between them at different AdvR values. The adjustment consisted firstly in determining the average of the expected "gaps" between each AdvR across the four AoA, for each of the aerodynamic variables. Then, working up through the tested AdvR values, the "gap" between the values of the actual tests, at the four selected AoA are determined, with the obtained average expected "gaps" added into the results. These "corrected gaps" are then averaged across the four AoA and applied to the actual test results for each of the AdvR across all AoA. This process is done sequentially until all results are corrected.

Additionally, it was also verified during the tests that the results were becoming more unstable from AdvR equal to 2 and above. This was due to the induced vibrations on the vertical support from the increased rotation speed on the prototype. In an attempt to increase the stability of the results, the multimeter integration time was increased from 5 seconds to 10 seconds for these AdvR.

The plots from all relevant aerodynamic coefficients of this set of tests are presented from figure 5.14 to figure 5.18. Due to clearly dubious results, the plot in figure 5.17 does not contain the results regarding AdvR equal to 0.5 and 3. The uncertainties calculated in subsection 5.6.2 are represented on the plots for two sets of AdvR results: AdvR=1 for the uncertainty with a multimeter integration time of 5 seconds and AdvR=3 (or AdvR=4 in the case of figure 5.17) for the uncertainty with an integration time of 10 seconds.

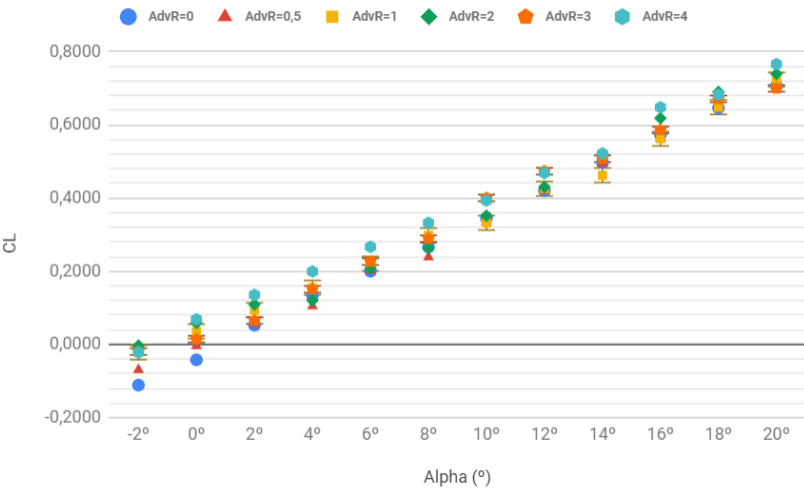


Figure 5.14: Lift coefficient results for the synchronous rotation tests.

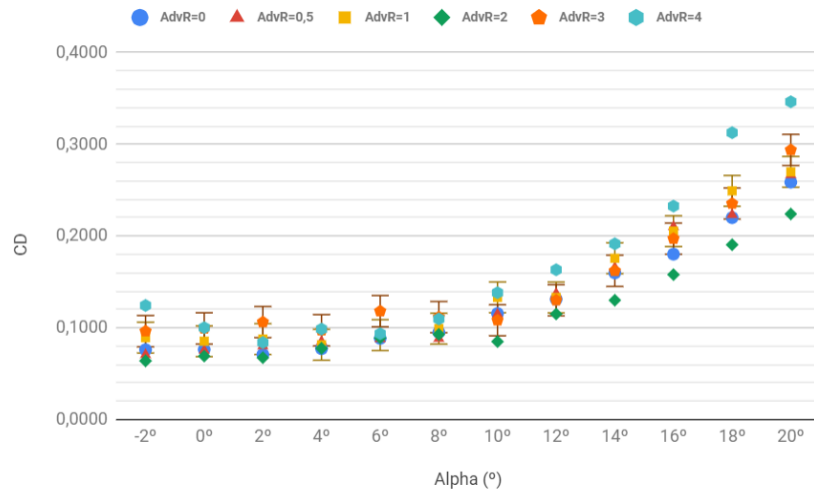


Figure 5.15: Drag coefficient results for the synchronous rotation tests.

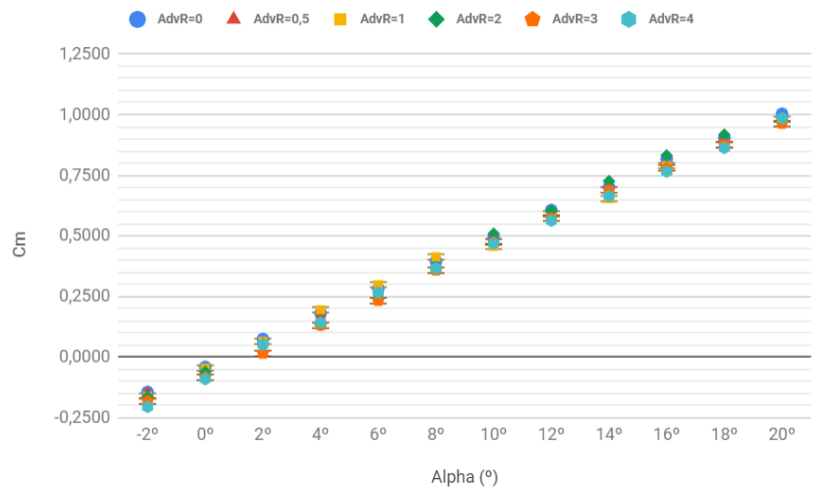


Figure 5.16: Pitching moment coefficient results for the synchronous rotation tests.

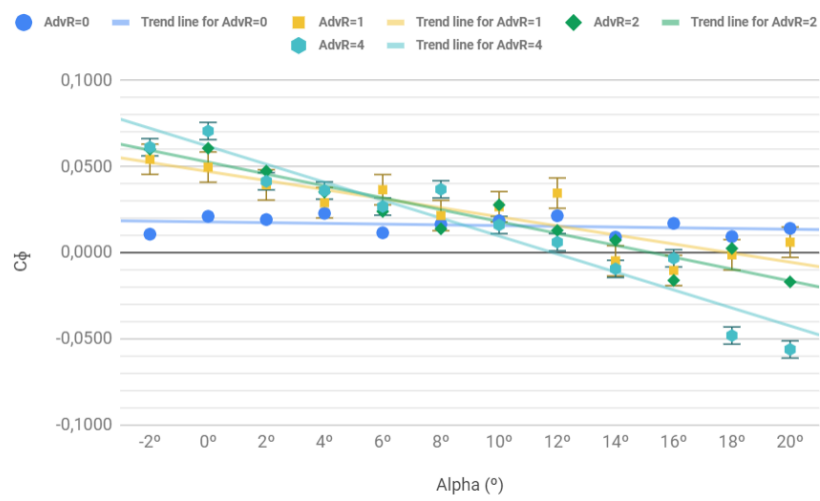


Figure 5.17: Roll moment coefficient results for the synchronous rotation tests.

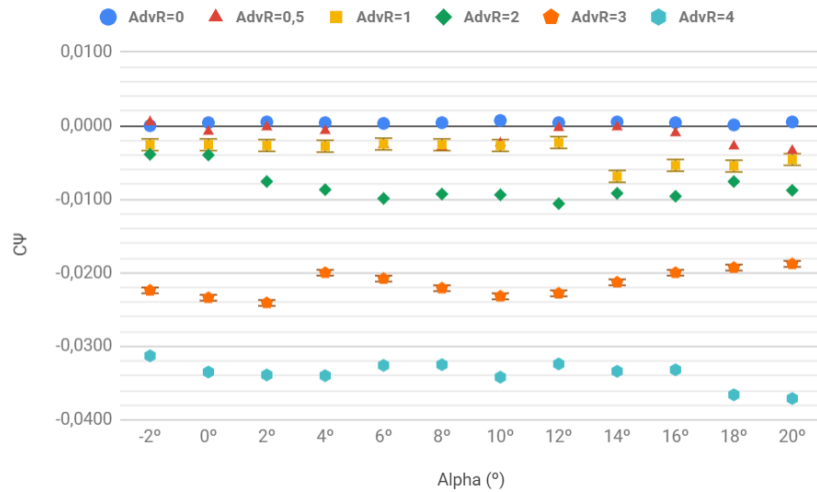


Figure 5.18: Yaw moment coefficient results for the synchronous rotation tests.

5.6.4 Asynchronous Rotation Tests with Static Lower Half

The next set of tests focused on the unique characteristic of the developed prototype: the capability for an asynchronous rotation between the two discs. Two configurations are relevant to the study, with the first one consisting of a static half with a rotating second half. In this case, the bottom disc was kept immobilised by fixing it with tape to the central pillar, with the top disc being set into a clockwise rotation when seen from above.

The asynchronous rotation meant the increase of oscillations between the two discs, when compared to the case of synchronous rotation, leading to increased loads on the motor and therefore a smaller maximum rotation speed. Out of the already tested AdvR values in subsection 5.6.3, the maximum permissible value to be tested for this configuration is an AdvR equal to 2. As such, the tests were performed at this AdvR being then compared to the results at that same value for the synchronous rotation. The plot in figure 5.19 includes the results of synchronous rotation for an AdvR=0 for a better analysis, as will be seen in section 5.7. Based on the observations of the previous tests, the multimeter integration time was kept at 10 seconds.

A "baseline" test was also performed, to ensure the correct distance between the obtained values in this configuration and the ones obtained in the synchronous rotation configuration. However, due to the way that the bottom disc is immobilised in this case, it is not possible to run both configurations at an AdvR=2 in a sequential manner (i.e. with the wind tunnel in continuous operation). As such, the asynchronous rotation was complemented with a fully static prototype (AdvR=0) at the four previously mentioned AoA. The adjustment is then made in relation to the AdvR=0 values, despite the results being presented in comparison to the synchronous AdvR=2 case.

The plots from all relevant aerodynamic coefficients of this set of tests are presented from figure 5.19

to figure 5.22. In this case, the calculated uncertainties are presented in all of the obtained results.

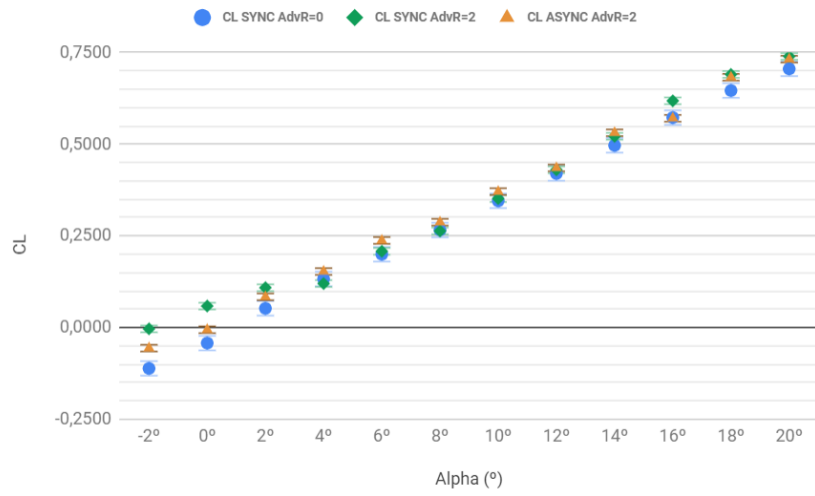


Figure 5.19: Lift coefficient results for the asynchronous rotation with static lower half tests.

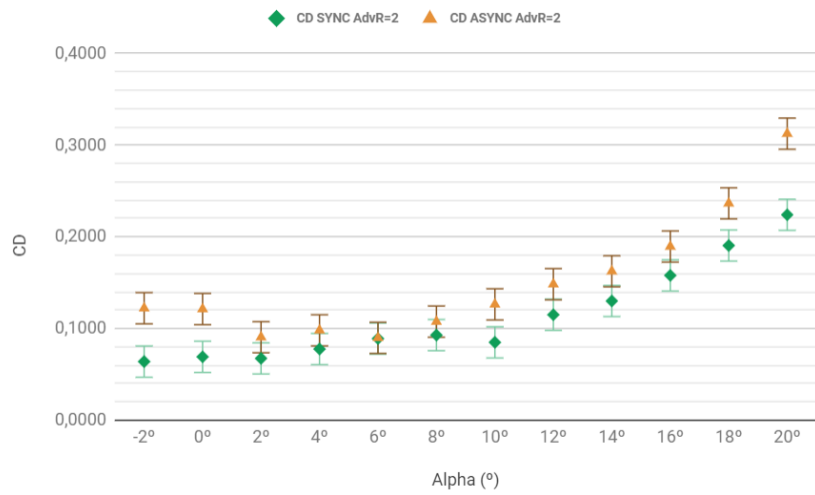


Figure 5.20: Drag coefficient results for the asynchronous rotation with static lower half tests.

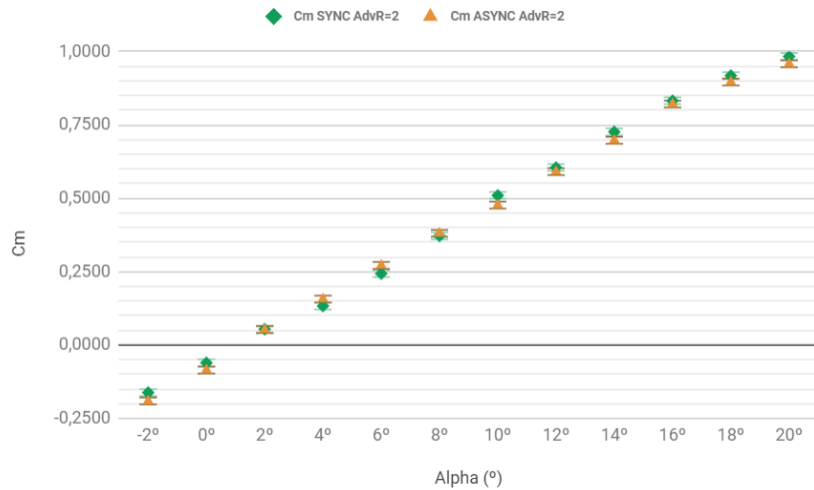


Figure 5.21: Pitching moment coefficient results for the asynchronous rotation with static lower half tests.

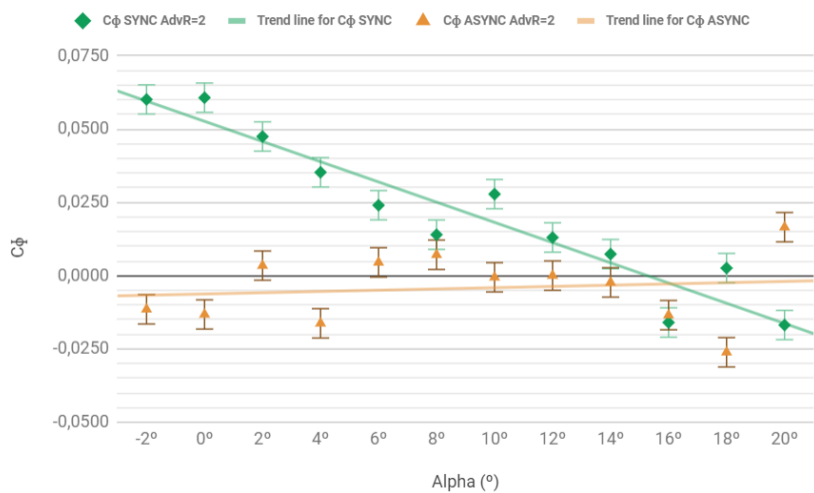


Figure 5.22: Roll moment coefficient results for the asynchronous rotation with static lower half tests.

5.6.5 Asynchronous Rotation Tests with Opposite Directions

The second configuration of interest to the study of asynchronous rotation consists in having the two discs rotating in opposite directions. In this case, both discs are set to rotate at the same speed, with the top disc rotating in a clockwise direction when seen from above and the bottom disc rotating in the opposite direction.

Even more noticeable than in the previous set of tests, the oscillations between the two discs are considerable, which has an impact on the maximum permissible rotation speed. Once again, the tests were performed at an AdvR equal to 2 and then compared to the results at that value for the synchronous rotation case. The multimeter integration time was set at 10 seconds, similarly to the previous configuration.

For similar reasons as the previous case, the "baseline" test performed for this configuration was identical to the one done in subsection 5.6.4. The plots with the relevant aerodynamic coefficients are then presented from figure 5.23 to figure 5.27, with the calculated uncertainties being presented in all results once more.

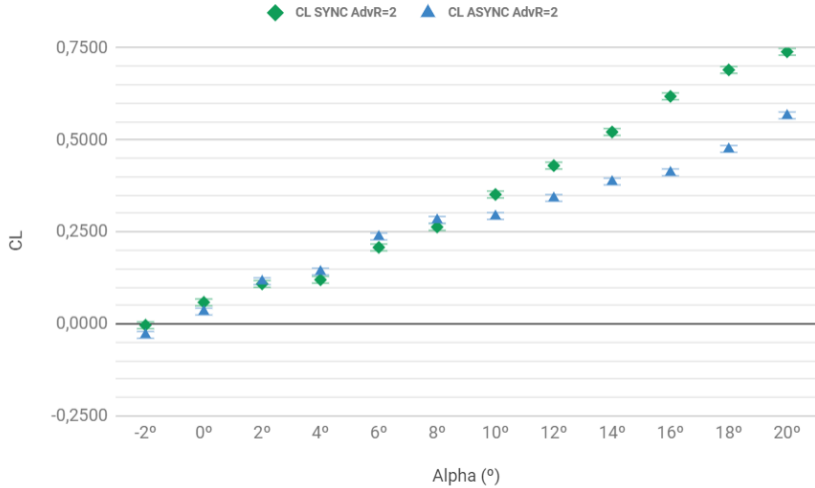


Figure 5.23: Lift coefficient results for the asynchronous rotation with opposite directions tests.

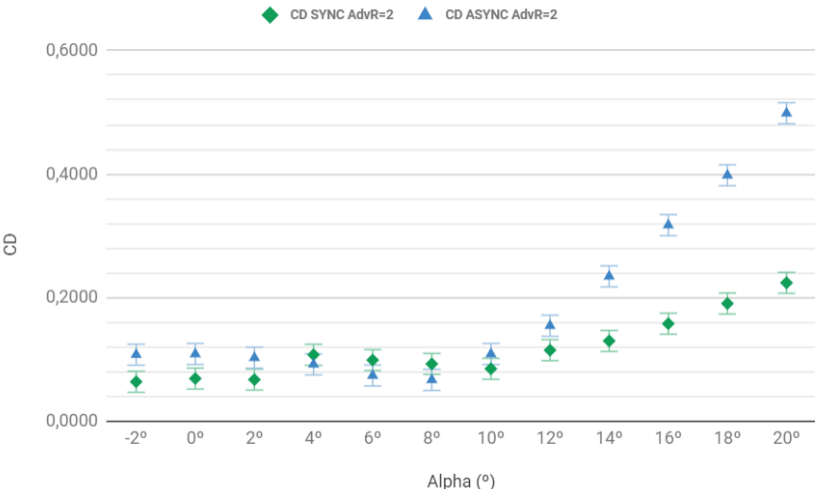


Figure 5.24: Drag coefficient results for the asynchronous rotation with opposite directions tests.

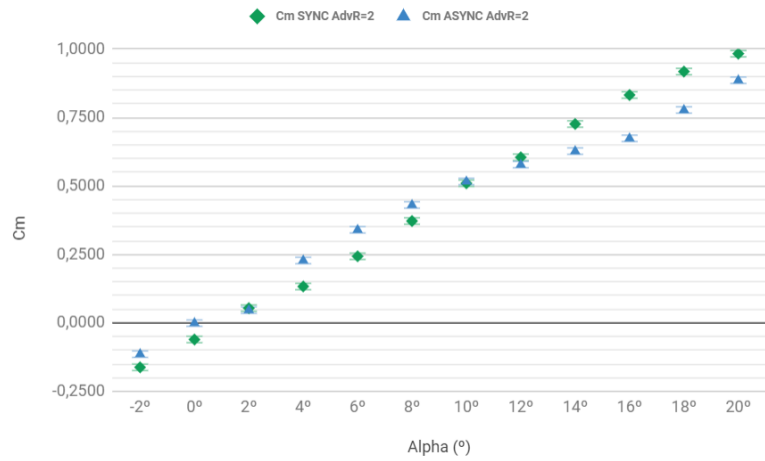


Figure 5.25: Pitching moment coefficient results for the asynchronous rotation with opposite directions tests.

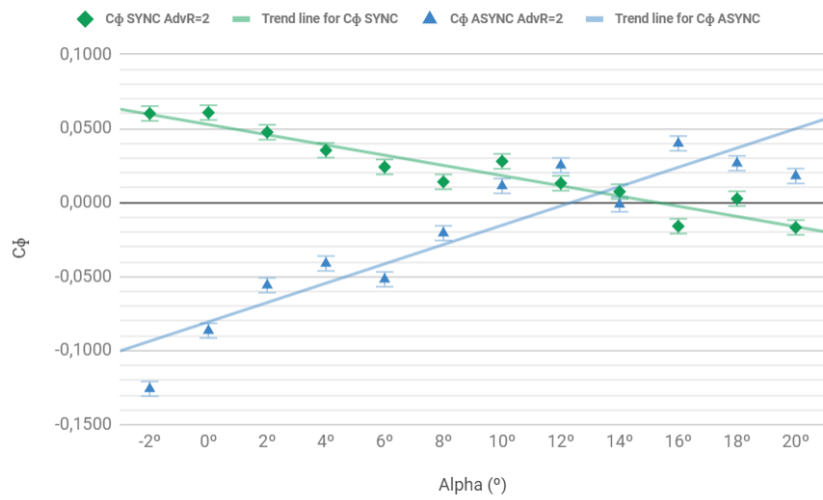


Figure 5.26: Roll moment coefficient results for the asynchronous rotation with opposite directions tests.

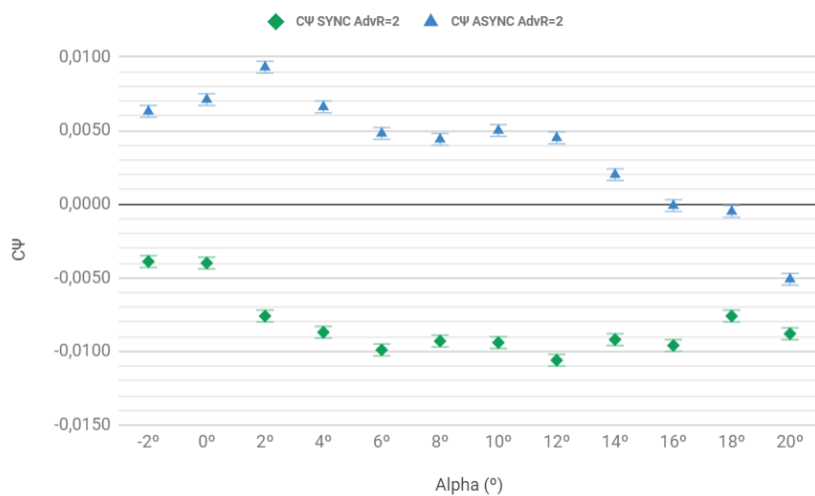


Figure 5.27: Yaw moment coefficient results for the asynchronous rotation with opposite directions tests.

5.6.6 Flow Visualization

In an attempt to better understand the obtained values of all of the performed tests, as well as to clarify the impact of the discs' oscillations on the surrounding airflow, a set of tests with a focus on a qualitative visualization of the flow surrounding the prototype were set up.

In order to perform them, some additional equipment was added into the wind tunnel assembly, which included:

- **Fog machine:** Turned on during the tests, supplies the "particles" necessary to identify flow patterns in the images taken;
- **Laser emitter:** Originally used for Particle Image Velocimetry (PIV) tests, sends out a vertical laser sheet in pulses, necessary to properly illuminate the flow surrounding the prototype. Due to its position, only the flow over the upper surface of the prototype can be visualised;
- **Digital Single Lens Reflex (DSLR) Camera:** Used to take pictures of the airflow surrounding the prototype. Caution needs to be taken, to ensure that the shutter is open when one of the laser pulses is being emitted.

The laser emitter was setup so that the flow crossing the mid-span plane of the prototype could be seen on the images taken, since this was the plane thought to present the clearest results.



(a) Laser emitter.



(b) Laser sheet over the prototype.

Figure 5.28: Laser system.

Some AoA and AdvR values were selected to represent the entire range of the performed tests: two low AoA (0° and 4°), one medium AoA (10°) and one high AoA (20°), no rotation (AdvR=0), medium rotation (AdvR=2) and high rotation (AdvR=4). In order to obtain as clear of an image as possible, the configuration that offered the least amount of oscillations, i.e. the one used in subsection 5.6.3 was used. The results are displayed from figure 5.29 to figure 5.32.

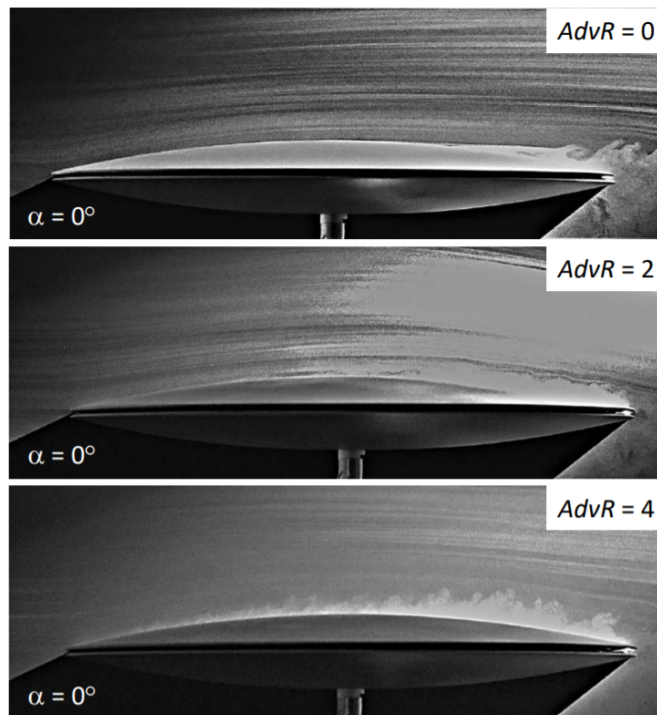


Figure 5.29: Flow visualization for $\alpha=0^\circ$.

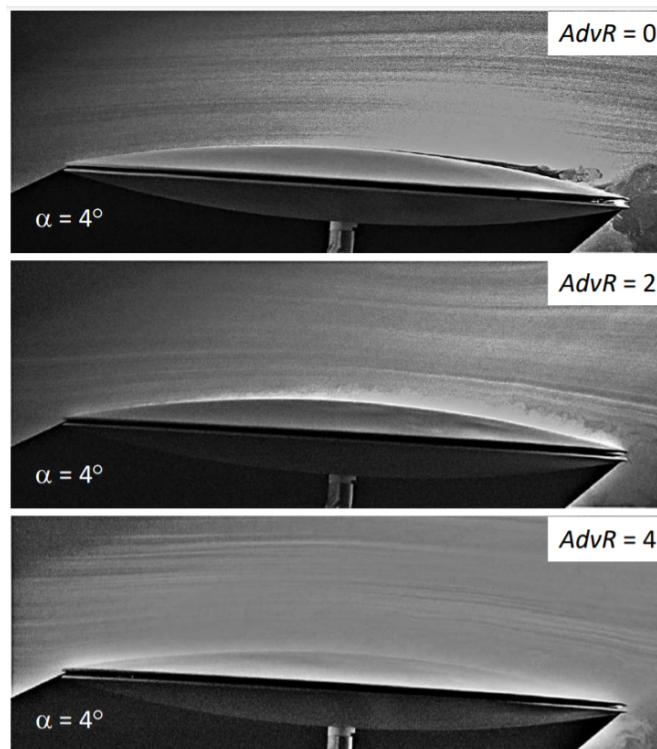


Figure 5.30: Flow visualization for $\alpha=4^\circ$.

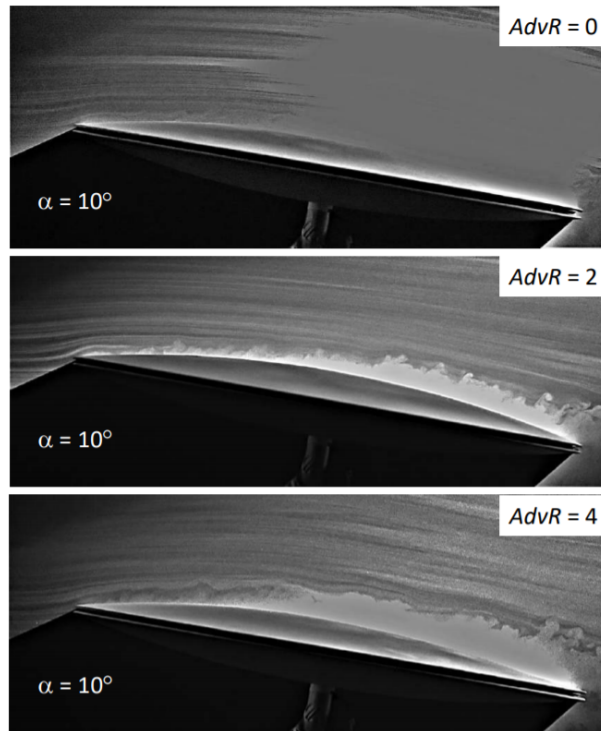


Figure 5.31: Flow visualization for $\alpha=10^\circ$.

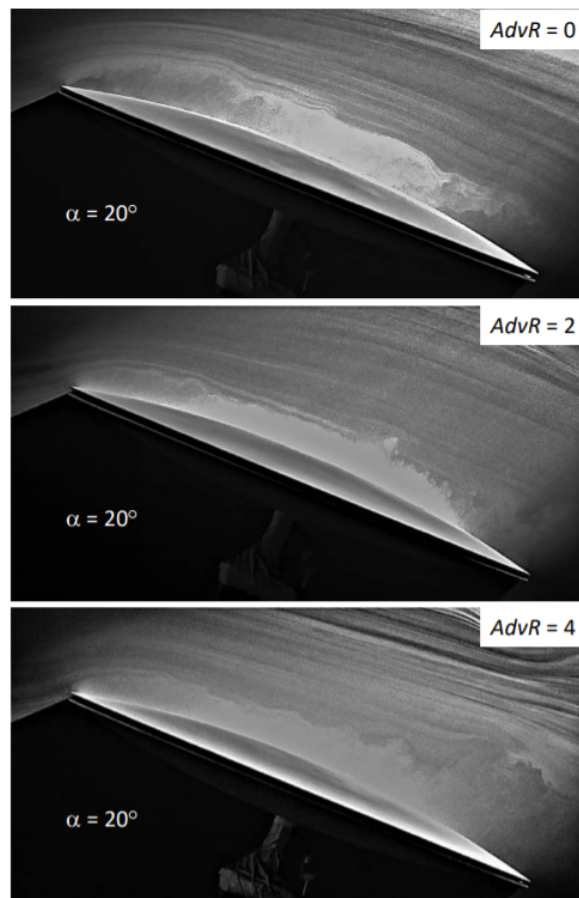


Figure 5.32: Flow visualization for $\alpha=20^\circ$.

5.7 Analysis of Results

Beginning the analysis with the flow visualization images at an $\alpha=0^\circ$ (figure 5.29): it can be clearly seen that, without rotation, there is a separation of the boundary layer as soon as an adverse pressure gradient begins to appear (at 50% of the chord). This is due to two factors, the first being the geometry of the prototype itself, which induces said pressure gradient. The second is the relatively low Reynolds number at which the tests were performed (recall that it had a value of $Re = 100000$), indicating a laminar boundary layer, which is much more susceptible to separation than a turbulent one associated to higher values of the Reynolds number.

Introducing rotation on the discs leads to an interaction between the induced von Kármán flow and the already present horizontal flow, which creates some turbulent structures. At an $AdvR=2$, these begin roughly at the midpoint of the chord, with the boundary layer section between the leading edge and that point presenting laminar flow characteristics. Crucially however, the introduction of the turbulent structures triggered a transition of the boundary layer, suppressing its separation. The increase of rotation to $AdvR=4$ simply led to the turbulent structures beginning closer to the leading edge, seen by the clear earlier transition of the boundary layer.

At an $\alpha=4^\circ$ (figure 5.30), the case of $AdvR=0$ is very similar to the previous one: there is still a laminar separation of the boundary layer, albeit happening slightly closer to the leading edge, due to the increase in AoA. The case of $AdvR=2$ confirms the explanation given for the previous AoA tests, since it is once again clear that the addition of rotation led to the creation of turbulent structures which prevent the separation of the boundary layer. This time however, transition begins much closer to the leading edge, being more comparable to the case of $AdvR=4$ at the previous AoA. This can be simply explained as an outcome of the increased AoA as well as the sharp edges of the prototype which will increase the air flow speed over the surface of the prototype, also increasing the Reynolds number, which of course triggers an earlier transition. At an $AdvR=4$, despite the lack of clarity in the picture, an increase of the thickness of the turbulent boundary layer can be observed.

Moving on to an $\alpha=10^\circ$ (figure 5.31), at an $AdvR=0$ it can be seen that a small separation bubble is present near the leading edge. This can be explained by the fact that, at this angle, the sharp edge will increase the flow speed to a point that can not be maintained following the leading edge. This effectively means that a considerable adverse pressure gradient exists in that area, forcing the flow to separate. However, the relatively low Reynolds number of the incoming air flow allows the separated flow to "mix" with it, leading to an increase of turbulence which promotes the flow to reattach to the surface of the disc aft of the leading edge, this time forming a turbulent boundary layer, which prevents further separation.

The addition of rotation at $AdvR=2$ leads to a forced transition which triggers the appearance of turbulent structures closer to the leading edge, however the separation bubble is still present, with the

separated flow reattaching roughly at the same point. Despite that, it is clear that the thickness of the boundary layer is considerably larger, no doubt due to the interaction with the von Kármán swirling flow. Increasing to an AdvR=4, it is clear that there is an increase in the thickness of the boundary layer, which is in-line with what has been found up to this point. However, the lack of quality of the image makes it difficult to conclude on whether the separation bubble is still present or not.

Finally, analysing the images taken at $\alpha=20^\circ$, it can be seen that without rotation, the flow separates right at the leading edge, quickly transitioning into turbulent flow. It then reattaches to the surface of the disc somewhere near the midpoint of the chord (the image quality makes it difficult to pinpoint the exact location of the reattachment). The structures seen aft of that point can be a result of transient effects from the separation bubble: it is important to note that these images represent a single instant in time, being crucial to separate the effects that are constant in time from those who are transient, in the analysis.

At an AdvR=2 the separation is still clearly visible, however, the added rotation has clearly decreased its thickness. The image makes it difficult to conclude on its chordwise extension, but it is safe to assume that it follows the same trend. Increasing the rotation to an AdvR=4 does not seem to affect the separation bubble any further, however, an increase of the thickness of the turbulent structures is verified, as is expected. A disturbance in the air flow lines near the trailing edge can be seen, a result of the swirling flow interaction from the perspective of the mid-span plane that the pictures represent, as mentioned in subsection 5.6.6.

In terms of the plots of the aerodynamic coefficients, let us begin by analysing the ones regarding the tests with synchronous rotation:

- C_L (**figure 5.14**): it can be seen that the slopes ($\frac{\partial C_L}{\partial \alpha}$) for the different AdvR results remain approximately constant. The values for AdvR=4 seem to be consistently above all other values, which is in-line with what CFD simulations done by Gomes [13] suggest that a very small increase should be expected at this AdvR. A note can be made regarding the dispersion of values, which is considerably larger at lower AoA. This can be explained simply by the fact that, at lower AoA, the generated forces are smaller, being naturally more difficult to measure accurately. As the AoA is increased so too are the generated forces, leading to a smaller dispersion between all AdvR;
- C_D (**figure 5.15**): for most AdvR, the values seem to be approximately the same, however, there are two exceptions. The first one is for AdvR=2 where it can be verified that the obtained values are generally lower, particularly at higher AoA. This aligns itself with what was observed in the flow visualization images, since it was at this value that some of the separation bubbles could be suppressed and, crucially, the turbulent structures were kept at moderately small thicknesses. Both of these factors contribute to an expected lower drag force, which is seen on the plot. The second exception is for an AdvR=4, with clearly larger values, that can be explained by the considerable

thickness of the turbulent structures, verified in the flow visualization figures. Despite the fact that most of the verified separation bubbles can be suppressed at this AdvR, the size of the turbulent vortices that are formed leads to a considerable increase in drag, an effect which is logically more noticeable at higher AoA, since it is paired up with the existence of the unsuppressed separation bubbles;

- C_m (**figure 5.16**): within the expected, with the results approximately equal across all tested AdvR values, a logical result if one takes into consideration the CFD results for C_L , since the pitching moment is directly dependent of this variable;
- C_ϕ (**figure 5.17**): it becomes clear that the rotation of the discs has an impact in this coefficient. Given how for an AdvR=0 the obtained values are approximately equal to zero and constant, with all other AdvR presenting different values, it can be concluded that the aerodynamic centre is located on the longitudinal symmetry axis of the prototype without rotation, being moved away from said axis with the introduction of rotation. Also of note is the gyroscopic effect present with the rotation of the discs, which certainly contributes for the noticeable difference between all AdvR results;
- C_ψ (**figure 5.18**): presents expected values, with an observable increase in the yaw moment from an AdvR=2 onward, when rotation begins to be more intense.

Moving on to the analysis of the asynchronous rotation plots, beginning with the case of the fixed bottom disc:

- C_L (**figure 5.19**): it can be seen that, although the difference between the values is relatively small, the results of the asynchronous rotation (taken at an AdvR=2) are roughly located between the synchronous rotation values taken at AdvR=0 and AdvR=2. This suggests that having two rotating discs is more beneficial than just one, in terms of lift generation, however, it also becomes clear that, for this prototype, having a single disc in rotation creates more lift than two static discs;
- C_D (**figure 5.20**): the asynchronous rotation can be observed to have, in general, larger values of C_D , indicating the possibility of it not enjoying the effect responsible for the lower values on the synchronous rotation case, described previously. This, however, is not within the expected, since the top disc is still rotating in the asynchronous case and therefore should be generating the mentioned effect. A possible explanation is that the added oscillations present in the asynchronous rotation led to an increase of the thickness of the turbulent structures on the top disc, which led to an increase of drag. Unfortunately, without flow visualization images to complement this analysis, it becomes difficult to pinpoint the exact reason for this increase;
- C_m (**figure 5.21**): despite not showing a large difference between asynchronous and synchronous rotations, the plot suggests a trend between the results similar to what is seen for the C_L values, which is within the expected;

- C_ϕ (**figure 5.22**): Despite considerable oscillations, an analysis of the trend line of the results seems to indicate a decrease in this coefficient for the asynchronous rotation case. This can be explained by the decrease of gyroscopic effects, since now one of the discs is immobilized.

Finally, the case of asynchronous rotation with opposite rotation directions:

- C_L (**figure 5.23**): results indicate a clear decrease in lift for the asynchronous rotation, particularly at higher AoA, not at all within what is expected, given how the direction of the rotation of the discs should not influence the amount of lift that is generated;
- C_D (**figure 5.24**): these results may help to clarify the behaviour of C_L , since an increase in drag is verified, once again being more noticeable at higher AoA. This suggests the presence of larger turbulent structures and even a larger separation bubble, no doubt a possible outcome of the considerable oscillations that were visually perceived between the discs during these tests;
- C_m (**figure 5.25**): results follow the same trend as the ones from C_L , as would be expected;
- C_ϕ (**figure 5.26**): an analysis of the trend line clearly indicates results with opposite signs to those obtained from the synchronous rotation case, which could indicate that the bottom disc has a larger contribution for this coefficient, since it was the one that changed the direction of rotation. This explanation also aligns itself with the values for this variable with a static bottom disc;
- C_ψ (**figure 5.27**): despite some oscillations, these results seem to be closer to zero for the asynchronous rotation, an expected outcome given how the discs should produce yaw moments with opposite directions but in equal magnitude.

Chapter 6

Conclusions

6.1 Achievements

The work done for this thesis had the objective of testing a unique configuration of a rotating disc-like wing, to determine its viability in an application within MAVs. With that in mind, several achievements can be highlighted:

- **Building the prototype:** a conceptual design of a prototype was developed, compliant with all imposed size restraints, namely a diameter of 400 mm and a relative thickness of 12%. The design consists of two discs that together form a circular wing with a symmetrical biconvex profile. The discs can rotate independent from each other, at different rotation speeds and directions. All of the elements necessary to rotate the discs (motors, central structure and gear system) are placed inside of the closed prototype, to minimize aerodynamic interference. A system of rails was developed to act both as an obstacle to the incoming flow, preventing it from entering the prototype, and as a base for a Teflon tube, responsible for minimizing friction between the discs. A study on available 3D printing materials was made, to determine the best options for all different components of the prototype. Ultimately, the built prototype can be attached to the aerodynamic scale present in the wind tunnel assembly with minimum aerodynamic interference. Dimensional inaccuracies in the prototype led to undesired oscillations which limited the maximum rotation speed of the discs. Despite that, the prototype can reach AdvR (the ratio between the discs' edge speed and the incoming flow velocity) values of up to 4 when both discs are rotating synchronously, and up to 2 when asynchronous rotation is applied, either with one of the discs stationary or both rotating at the same speed but opposite directions, which allows for a fair range of speeds to be tested;
- **Flow visualization tests:** flow visualization images were obtained for a synchronous rotation case at AoA equal to 0° , 2° , 10° and 20° , for AdvR values equal to 0, 2 and 4. The images show the flow pattern over the top disc, thanks to the equipment typically used for PIV tests. Without rotation, laminar separation is present at lower AoA, with a small separation bubble appearing at

$\alpha=10^\circ$, which grows in size at $\alpha=20^\circ$. The introduction of rotation leads to an interaction of the induced von Kármán swirling flow and the incoming flow from the wind tunnel, which generates turbulent structures. These help to suppress flow separation at lower AoA and decrease the size of the separation bubble at higher AoA. The major observable difference between the AdvR=2 and AdvR=4 cases is the increase in the thickness of turbulent structures with the increase of AdvR;

- **Synchronous rotation tests:** results of a synchronous rotation case were obtained with an aerodynamic scale and a previously developed software. The tests were performed at a relatively low Reynolds number of $Re = 100000$ for a range of AdvR (0, 0.5, 1, 2, 3 and 4). C_L results aligned themselves with previously obtained CFD data only showing a slight increase at AdvR=4. C_D results showcase lower values of this coefficient at an AdvR=2 due to the suppression or minimization of the separation bubble with turbulent structures of moderately small thicknesses. This suggests that the best aerodynamic performance of the prototype is seen with a synchronous rotation at this AdvR, given the approximately similar C_L results, certainly indicating a larger lift-to-drag ratio for this case. C_ϕ values suggest an influence of rotation on this coefficient, with an increase of the rolling moment with AdvR, due to a movement of the centre of pressure and gyroscopic effects.
- **Asynchronous rotation with static lower half tests:** a situation of asynchronous rotation with a static bottom disc was analysed at the same Reynolds number. Oscillations between the discs limited the AdvR to a value of 2. Results were compared to the synchronous rotation case at the same AdvR. C_L values indicate a general decrease, in comparison to the synchronous case, but not enough to be lower than two static discs, since the rotation has a positive effect on laminar separation phenomena, even if present in only one of the discs. C_D results show an increase for the asynchronous rotation case, a possible outcome of the increased oscillations between discs. An analysis of the C_ϕ trend line indicates a significant decrease of this coefficient, possibly due to a decrease of gyroscopic effects.
- **Asynchronous rotation with opposite directions tests:** a final asynchronous rotation case was analysed at the same Reynolds number. This time, both discs were set at an AdvR=2 but with opposite directions. Results were once again compared to the synchronous rotation ones at the same AdvR. The decrease of C_L and increase of C_D at higher AoA, suggests larger turbulent structures and separation bubbles, due to the increase of oscillations between the discs, seen at a maximum amount for this rotation case. C_ϕ results indicate a change in sign across the range of AoA, when compared to the ones obtained for the synchronous rotation. Given how the bottom disc was the only that changed the direction of rotation, this implies that this disc has a larger influence on this coefficient. Lastly, C_ψ results can be seen closer to zero for this asynchronous rotation, an expected result since the two discs rotating in opposite directions should produce equal yaw moments with opposite signs.

In conclusion, despite the difficulties that arose throughout development, in particular the ones associated to the dimensional inaccuracies of the built prototype which unfortunately led to a less than

optimal set of test results, the ones that were obtained showcased some interesting phenomena, especially those regarding C_D , C_ϕ and C_ψ . It is important to keep in mind that the wing design studied here is a novel concept, so, although the question of "can this configuration be used on MAVs?" remains without a conclusive answer, the obtained results are interesting enough to have contributed to the study of flying discs and prove that further investigations on this innovative disc configuration are worthwhile, for which this work can serve as a baseline to.

6.2 Future Work

As mentioned previously this work should serve as a stepping stone to further studies on similar configurations of rotating flying discs. As such, some points that could be considered for future studies are:

- **Rebuild the prototype with a different manufacturing method:** it became clear that current solutions within the 3D printing space do not provide the level of dimensional accuracy required for this prototype. The technology will certainly evolve, but at the time of writing, a process based on computer aided manufacturing, despite being more expensive and possibly more time consuming, will certainly lead to more favourable results;
- **Test the prototype at larger AdvR values:** based on the previous point, if a prototype can be built that allows for higher rotations to be reached, a wider range of AdvR should be tested. This point is particularly relevant for the cases of asynchronous rotation;
- **Perform a more in-depth flow visualization analysis:** the images that were obtained for this study are quite revealing, helping to better understand the flow surrounding the prototype. As such, it will certainly be quite beneficial to expand this study to the cases of asynchronous rotation. Additionally, a quantification of the flow field using PIV should be performed, which will certainly add to the knowledge of the surrounding flow;
- **Test more asynchronous rotation configurations:** an interesting scenario that was not tested on this thesis is one where both discs are rotating, albeit with different rotation speeds. If done at all possible permutations of the direction of rotation of the discs, a wide range of tests can be performed that will certainly explore this innovative configuration to its maximum.

Bibliography

- [1] ADIFO Aircraft. *ADIFO*. URL: <http://www.adifoaircraft.com/> (visited on 11/25/2020).
- [2] ADIFO Aircraft. *All of the thrust directions produced by the ADIFO prototype*. URL: <https://newatlas.com/adifo-flying-saucer-romanian/58999/#gallery:6> (visited on 11/25/2020).
- [3] E. M. Almas. “Orgãos de Máquinas: Volume I”. Class Notes. 2018.
- [4] E. Appelquist et al. “Turbulence in the rotating-disk boundary layer investigated through direct numerical simulations”. In: *European Journal of Mechanics / B Fluids* (Jan. 2018).
- [5] V. de Brederode. *Aerodinâmica Incompressível: Fundamentos*. 1st ed. IST Press, 2014.
- [6] *Brushless DC-Flat Motors Series 3216... BXT H*. Faulhaber. Aug. 2020.
- [7] H. W. Coleman and W. G. Steele. *Experimentation, validation, and uncertainty analysis for engineers*. 4th ed. John Wiley & Sons, 2018.
- [8] H. Delgado. “Novas Tecnologias Biomiméticas para a Aerodinâmica de Veículos Aéreos a Baixo Número de Reynolds”. PhD thesis. Instituto Superior Técnico, 2018.
- [9] Engineers Edge. *Viscosity of Air, Dynamic and Kinematic*. 2000. URL: https://www.engineersedge.com/physics/viscosity_of_air_dynamic_and_kinematic_14483.htm (visited on 10/30/2020).
- [10] U.S. Air Force. *Cutaway drawing of the Avrocar showing its major components*. URL: <https://media.defense.gov/2008/Mar/13/2000644712/-1/-1/0/080313-F-1234P-012.JPG> (visited on 11/25/2020).
- [11] U.S. Air Force. *Overhead view of the Avrocar*. URL: <https://media.defense.gov/2015/Oct/09/2001299080/-1/-1/0/151009-F-DW547-015.JPG> (visited on 11/25/2020).
- [12] K. Giang. *PLA vs. ABS: What's the difference?* 2020. URL: <https://www.3dhubs.com/knowledge-base/pla-vs-abs-whats-difference/> (visited on 11/02/2020).
- [13] M. Gomes. “The Flying Saucer Concept for Micro Aerial Vehicles: Computational Study”. MA thesis. Instituto Superior Técnico, July 2021.
- [14] J. J. Healey. “Model for unstable global modes in the rotating-disk boundary layer”. In: *Journal of Fluid Mechanics* 663.8 (Aug. 2010), pp. 148–159.
- [15] H. Higuchi et al. “Rotating Flying Disks and Formation of Trailing Vortices”. In: *18th AIAA Applied Aerodynamics Conference* (Aug. 2000).

- [16] S. F. Hoerner. *Fluid-Dynamic Drag: Practical information on aerodynamic drag and hydrodynamic resistance*. 1965.
- [17] S. F. Hoerner. *Fluid-Dynamic Lift: Practical information on aerodynamic and hydrodynamic lift*. Ed. by H. V. Borst. 2nd ed. Hoerner, L. A., 1985.
- [18] Icus. *Configurador CAD*. 2020. URL: https://www.igus-cad.com/default.aspx?treeid=10301&__hstc=150219241.f75b61591b0b67241f4a7c7daf5d18a6.1595253813069.1602759661330.1604254449600.24&__hssc=150219241.2.1604254449600&__hsfp=335341055&_ga=2.67882645.566300696.1604254449-2012016545.1595347273 (visited on 11/01/2020).
- [19] S. Imayama. *Experimental study of the rotating-disk boundary-layer flow*. Tech. rep. SE-100 44 Stockholm, Sweden: Royal Institute of Technology, May 2012.
- [20] S. Imayama. "Studies of the rotating-disk boundary-layer flow". PhD thesis. SE-100 44 Stockholm, Sweden: Royal Institute of Technology, Dec. 2014.
- [21] S. Imayama, P. H. Alfredsson, and R.J. Lingwood. "An experimental study of laminar-turbulent transition of a rotating-disk flow". In: *EUROMECH Colloquium 525 - Instabilities and transition in three-dimensional flows with rotation* (June 2011).
- [22] N. M. Kamaruddin. "Dynamics and Performance of Flying Discs". PhD thesis. School of Mechanical, Aerospace and Civil Engineering - University of Manchester, 2011.
- [23] K. Kwon and S. O. Park. "Aerodynamic Characteristics of an Elliptic Airfoil at Low Reynolds Number". In: *Journal of Aircraft* 42.6 (June 2005), pp. 1642–1644.
- [24] D. Lee et al. "Mechanisms of surface pressure distribution within a laminar separation bubble at different Reynolds numbers". In: *Physics of Fluids* 27.023602 (2015).
- [25] R. J. Lingwood. "Absolute instability of the boundary layer on a rotating disk". In: *Journal of Fluid Mechanics* (1995a).
- [26] B. Lucoveic, F. Vargas, and P. Paglione. "Control Augmentation System and Auto Pilot using Back-stepping Thecnique". In: *23rd ABCM International Congress of Mechanical Engineering* (Dec. 2015).
- [27] *Maxon Product Range 2021/2022*. Maxon. Mar. 2021.
- [28] T. J. Mueller and G. E. Torres. *Aerodynamics of Low Aspect Ratio Wings at Low Reynolds Numbers With Applications to Micro Air Vehicle Design and Optimization*. Final Contractor Report. University of Notre Dame, Nov. 2001.
- [29] J. R. Potts and W. J. Crowther. "The Flow Over a Rotating Disc-Wing". In: *Aerodynamics Research Conference* (Apr. 2000).
- [30] J.R. Potts and W.J. Crowther. "*FrisbeeTM* Aerodynamics". In: *20th AIAA Applied Aerodynamics Conference Exhibit* (June 2002).
- [31] J.R. Potts and W.J. Crowther. "Flight Control of a Spin Stabilised Axi-Symmetric Disc-Wing". In: *American Institute of Aeronautics and Astronautics* (2001).

- [32] P. Pozderac. *Gone With the Wind: An Investigation into the Flight Dynamics of Discs*. Tech. rep. Physics Department, The College of Wooster, May 2016.
- [33] W. B. Roberts. "Calculation of Laminar Separation Bubbles and Their Effect on Airfoil Performance". In: *AIAA Journal* 18.79-0285R (1980).
- [34] F. Roque. "Desenvolvimento de uma plataforma aberta e escalável para aquisição de dados no túnel aerodinâmico de baixa velocidade". MA thesis. Instituto Superior Técnico, Oct. 2012.
- [35] K. Seo et al. "Optimization of the size and launch conditions of a discus". In: *The 2014 conference of the International Sports Engineering Association* (2014).
- [36] Simplify3D. *ABS*. 2020. URL: <https://www.simplify3d.com/support/materials-guide/abs/> (visited on 11/02/2020).
- [37] Simplify3D. *PLA*. 2020. URL: <https://www.simplify3d.com/support/materials-guide/pla/> (visited on 11/02/2020).
- [38] Airfoil Tools. *NACA 0012 AIRFOILS (n0012-il)*. URL: <http://airfoiltools.com/airfoil/details?airfoil=n0012-il> (visited on 11/30/2020).
- [39] National Museum of the United States Air Force. *Avro Canada VZ-9AV Avrocar*. Oct. 2015. URL: <https://www.nationalmuseum.af.mil/Visit/Museum-Exhibits/Fact-Sheets/Display/Article/195801/avro-canada-vz-9av-avrocar/> (visited on 11/25/2020).
- [40] F. Zoueshtiagh et al. "Laminar-turbulent boundary-layer transition over a rough rotating disk". In: *Physics of Fluids* 15.8 (Aug. 2003), pp. 2441–2444.

Appendix A

Numerical Solution for Ordinary Differential Equations in von Kármán's Problem

In order to solve the problem described in subsection 2.1.6, von Kármán introduced a characteristic length ξ (defined in section 4.3) as well as some assumptions regarding the velocity components and pressure:

$$U = \Omega r F(\xi) , \quad (\text{A.1})$$

$$V = \Omega r G(\xi) , \quad (\text{A.2})$$

$$W = (\Omega \nu)^{\frac{1}{2}} H(\xi) , \quad (\text{A.3})$$

$$p = -\rho \Omega \nu P(\xi) . \quad (\text{A.4})$$

This change of variables allows for the derivation of a similarity solution of the steady Navier-Stokes equations, which can then be numerically solved, with the derivatives of the variables in regards to ξ being represented by ':

$$H' = -2F , \quad (\text{A.5})$$

$$F'' = F^2 - G^2 + F'H , \quad (\text{A.6})$$

$$G'' = 2FG + G'H, \quad (\text{A.7})$$

$$P' = HH' - H'' . \quad (\text{A.8})$$

The values for F , G , H and $P - P(0)$, as well as the derivatives of the radial and azimuthal variables are presented, in regards to ξ , in figure A.1:

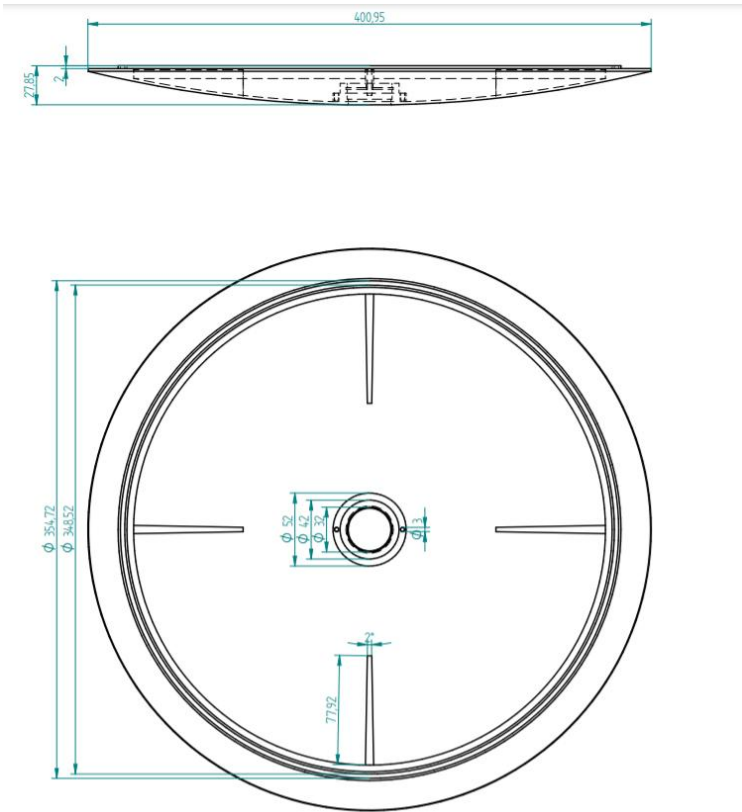
ξ	F	G	H	P-P(0)	F'	G'
0.0	0.0000	1.0000	0.0000	0.0000	0.5102	-0.6159
0.1	0.0462	0.9386	-0.0048	0.0925	0.4163	-0.6112
0.2	0.0836	0.8780	-0.0179	0.1674	0.3338	-0.5987
0.3	0.1133	0.8190	-0.0377	0.2274	0.2620	-0.5803
0.4	0.1364	0.7621	-0.0628	0.2747	0.1999	-0.5577
0.5	0.1536	0.7076	-0.0919	0.3115	0.1467	-0.5321
0.6	0.1660	0.6557	-0.1239	0.3396	0.1015	-0.5047
0.7	0.1742	0.6067	-0.1580	0.3608	0.0635	-0.4764
0.8	0.1789	0.5605	-0.1934	0.3764	0.0317	-0.4476
0.9	0.1807	0.5171	-0.2294	0.3877	0.0056	-0.4191
1.0	0.1802	0.4766	-0.2655	0.3955	-0.0157	-0.3911
1.1	0.1777	0.4389	-0.3013	0.4008	-0.0327	-0.3641
1.2	0.1737	0.4038	-0.3365	0.4041	-0.0461	-0.3381
1.3	0.1686	0.3712	-0.3707	0.4059	-0.0564	-0.3133
1.4	0.1625	0.3411	-0.4038	0.4066	-0.0640	-0.2898
1.5	0.1559	0.3132	-0.4357	0.4066	-0.0693	-0.2677
1.6	0.1487	0.2875	-0.4661	0.4061	-0.0728	-0.2470
1.7	0.1414	0.2638	-0.4952	0.4053	-0.0747	-0.2276
1.8	0.1338	0.2419	-0.5227	0.4043	-0.0754	-0.2095
1.9	0.1263	0.2218	-0.5487	0.4031	-0.0751	-0.1927
2.0	0.1189	0.2033	-0.5732	0.4020	-0.0739	-0.1771
2.1	0.1115	0.1864	-0.5962	0.4008	-0.0721	-0.1627
2.2	0.1045	0.1708	-0.6178	0.3998	-0.0698	-0.1494
2.3	0.0976	0.1565	-0.6380	0.3987	-0.0671	-0.1371
2.4	0.0910	0.1433	-0.6569	0.3978	-0.0643	-0.1258
2.5	0.0848	0.1313	-0.6745	0.3970	-0.0612	-0.1153
2.6	0.0788	0.1202	-0.6908	0.3962	-0.0580	-0.1057
2.7	0.0732	0.1101	-0.7060	0.3955	-0.0548	-0.0969
2.8	0.0678	0.1008	-0.7201	0.3949	-0.0517	-0.0888
2.9	0.0628	0.0923	-0.7332	0.3944	-0.0485	-0.0814
3.0	0.0581	0.0845	-0.7452	0.3939	-0.0455	-0.0745
3.2	0.0496	0.0708	-0.7668	0.3932	-0.0397	-0.0625
3.4	0.0422	0.0594	-0.7851	0.3926	-0.0343	-0.0524
3.6	0.0358	0.0498	-0.8007	0.3922	-0.0296	-0.0440
3.8	0.0304	0.0417	-0.8139	0.3919	-0.0253	-0.0369
4.0	0.0257	0.0349	-0.8251	0.3917	-0.0216	-0.0309
4.5	0.0168	0.0225	-0.8460	0.3914	-0.0144	-0.0199
5.0	0.0109	0.0144	-0.8596	0.3912	-0.0094	-0.0128
5.5	0.0070	0.0093	-0.8684	0.3912	-0.0062	-0.0082
6.0	0.0045	0.0060	-0.8741	0.3912	-0.0040	-0.0053
7.0	0.0019	0.0025	-0.8802	0.3912	-0.0017	-0.0022
8.0	0.0008	0.0010	-0.8827	0.3911	-0.0007	-0.0009
9.0	0.0003	0.0004	-0.8837	0.3911	-0.0003	-0.0004
10.0	0.0001	0.0002	-0.8842	0.3911	-0.0001	-0.0002
∞	0.0000	0.0000	-0.8845	0.3911	0.0000	0.0000

Figure A.1: Numerical solutions of the ordinary differential equations.

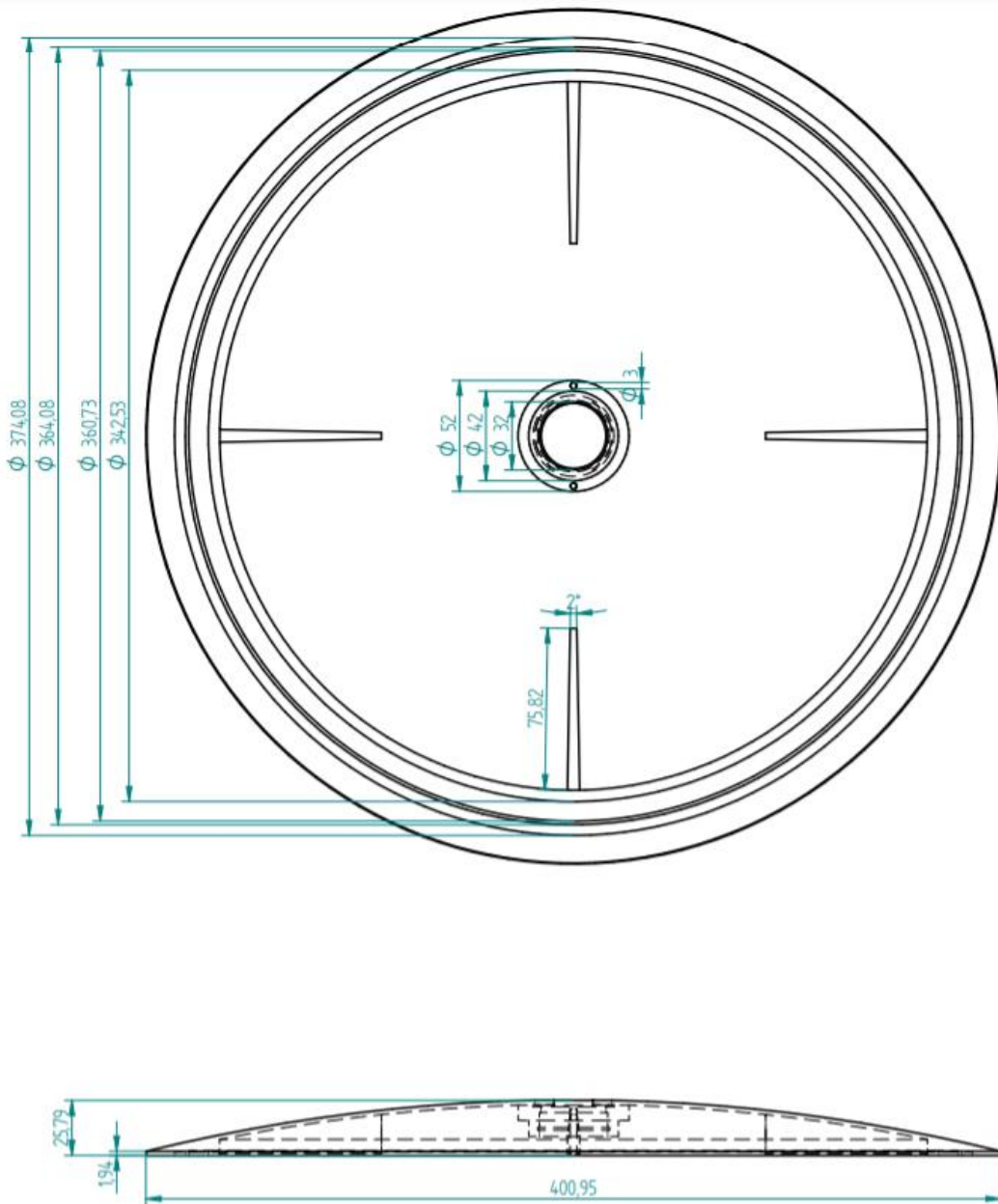
Appendix B

Prototype's Drawings and General Dimensions

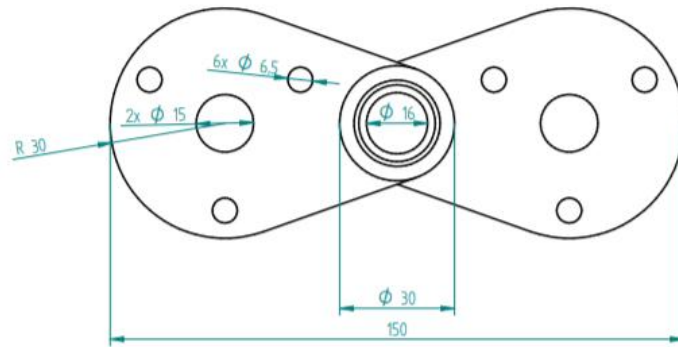
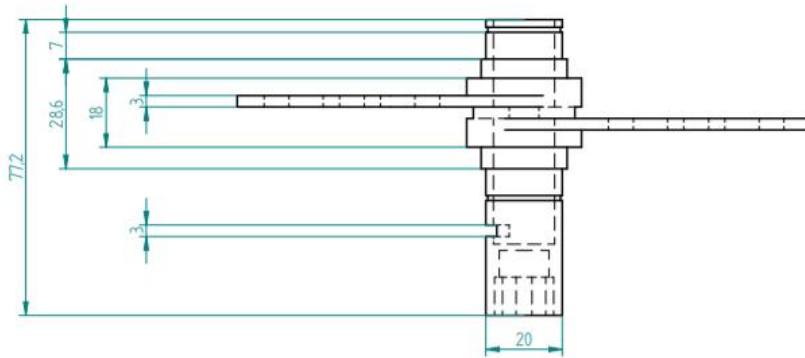
B.1 Bottom Disc



B.2 Top Disc



B.3 Central Structure

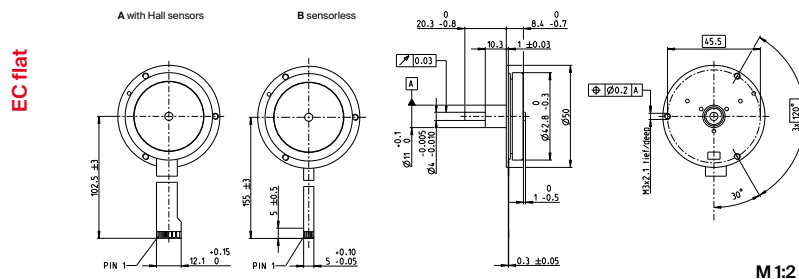


Appendix C

Motors' Datasheets

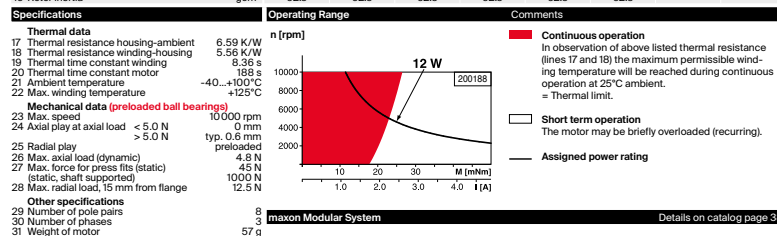
C.1 Maxon's EC 45 flat [27]

EC 45 flat Ø42.8 mm, brushless, 12 Watt



	Part Numbers					
	A with Hall sensors		B sensorless			
Stock program	200188	339275	339276	339277	339278	
Standard program		200141				
Special program (on request)						

Motor Data		200188	200141	339275	339277	339276	339278
Values at nominal voltage							
1 Nominal voltage	V	9	9	12	12	24	24
2 No load speed	rpm	8000	7980	8160	8150	7310	7300
3 No load current	mA	147	147	115	115	476	476
4 Nominal speed	rpm	4780	4540	4540	4720	4390	4360
5 Nominal torque (max. continuous torque)	mNm	23.8	23.6	20.1	20	27	27
6 Nominal current (max. continuous current)	A	2.04	2.04	1.37	1.37	0.766	0.768
7 Stall torque ¹	mNm	92.6	80.6	70.8	66.5	114	112
8 Stall current ¹	A	8.9	7.75	5.24	4.92	3.74	3.67
9 Max. efficiency	%	77	75	73	73	79	79
Characteristics							
10 Terminal resistance phase to phase	Ω	1.01	1.16	2.29	2.44	6.42	6.54
11 Terminal inductance phase to phase	mH	0.32	0.32	0.541	0.541	2.75	2.75
12 Torque constant	mNm/A	10.4	10.4	13.5	13.5	30.5	30.5
13 Speed constant	rpm/V	918	918	706	706	313	313
14 Speed/torque gradient	rpm/mNm	89.3	103	120	128	65.9	671
15 Mechanical time constant	ms	48.9	56.1	65.5	69.8	36.1	36.8
16 Rotor inertia	gcm ²	52.3	52.3	52.3	52.3	52.3	52.3



Specifications	Operating Range	Comments
17 Thermal data	6.59 K/W	Continuous operation In observation of above listed thermal resistance (lines 17 and 18) the maximum permissible winding temperature will be reached during continuous operation at 25°C ambient. = Thermal limit.
18 Thermal resistance housing-ambient	5.56 K/W	
19 Thermal time constant winding	8.36 s	Short term operation The motor may be briefly overloaded (recurring).
20 Thermal time constant motor	193 s	
21 Ambient temperature	-40...+100°C	Assigned power rating
22 Max. winding temperature	+125°C	
Mechanical data (preloaded ball bearings)		
23 Max. speed	10000 rpm	
24 Axial play at axial load < 5.0 N	0 mm	
25 Radial play	typ. 0.6 mm preloaded	
26 Max. axial load (dynamic) (static, shaft supported)	4.8 N	
27 Max. force for press fits (static)	45 N	
28 Max. radial load, 15 mm from flange	1000 N	
Other specifications		
29 Number of pole pairs	3	
30 Number of phases	3	
31 Weight of motor	57 g	

Values listed in the table are nominal. maxon Modular System Details on catalog page 38

Connection	with Hall sensors	sensorless
Pin 1	V ₊ 4.5...16 VDC	Motor winding 1
Pin 2	Hall sensor 3*	Motor winding 2
Pin 3	Hall sensor 1*	Motor winding 3
Pin 4	Hall sensor 2*	Λ-neutral point
Pin 5	GND	
Pin 6	Motor winding 3	
Pin 7	Motor winding 2	
Pin 8	Motor winding 1	

Adapter	Part number	Part number
see p. 514	220300	220310
Connector	Part number	Part number
TE	1-84953-1	84953-4
Molex	52207-1133	52207-0433

Pin for design with Hall sensors:
 *Calculation does not include saturation effect (p. 61/168)
 Pin for design with Hall sensors:
 FPC, 11-pol, Pitch 1.0 mm, top contact style
 Wiring diagram for Hall sensors see p. 49

Recommended Electronics:	Notes	Page 38
ESCON Module 24/2		486
ESCON 36/3 EC		487
ESCON Mod. 50/4 EC-S		487
DEC Module 24/2		491
EPOS4 Micro 24/5		495
EPOS4 Mod./Comp. 24/1.5		496
EPOS4 Mod./Comp. 50/5		496
EPOS4 Comp. 24/5 3-axis		497
EPOS4 50/5		501

C.2 Faulhaber's Brushless DC-Flat Motors [6]

NEW

FAULHABER

Brushless DC-Flat Motors

38 mNm

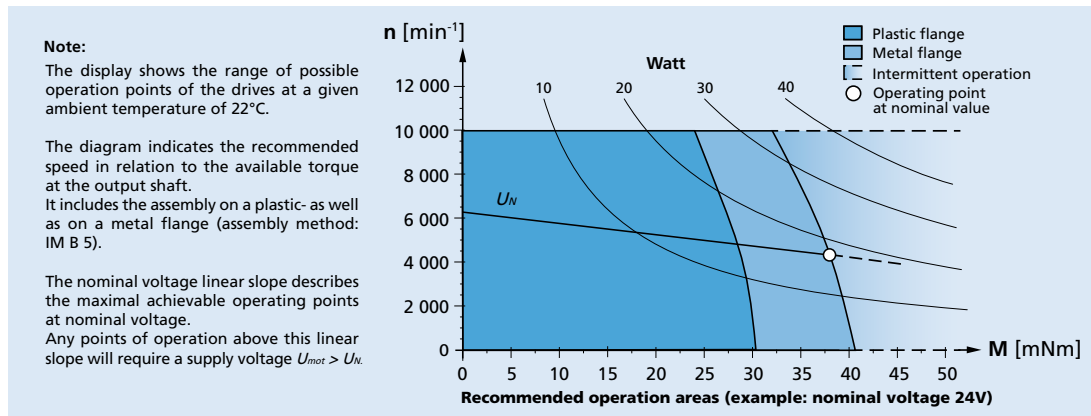
External rotor technology, with housing

20 W

Series 3216 ... BXT H

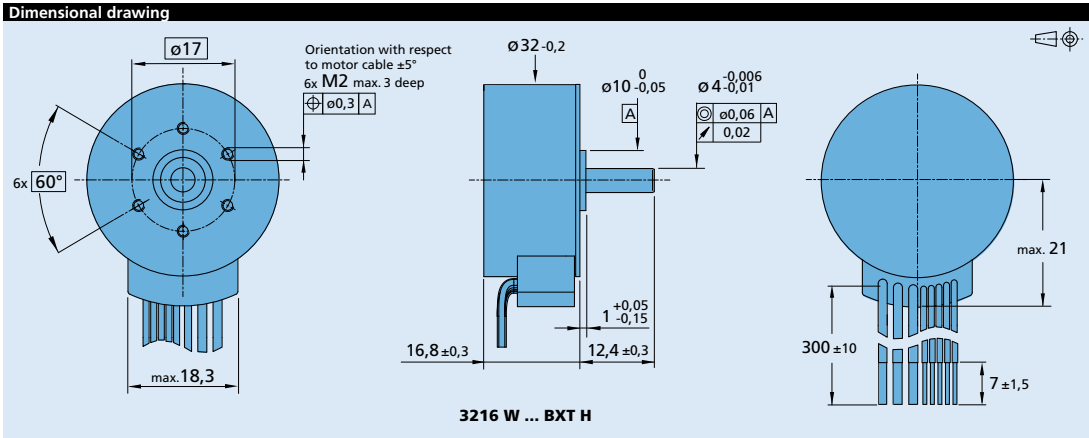
Values at 22°C and nominal voltage	3216 W	009 BXT H	012 BXT H	024 BXT H	
1 Nominal voltage	U_N	9	12	24	V
2 Terminal resistance, phase-phase	R	0,55	0,88	3,26	Ω
3 Efficiency, max.	η_{max}	83	84	81	%
4 No-load speed	n_0	6 060	6 230	6 250	min ⁻¹
5 No-load current, typ. (with shaft \varnothing 4 mm)	I_0	0,165	0,126	0,068	A
6 Starting torque	M_A	225	245	263	mNm
7 Speed constant	k_n	691	530	267	min ⁻¹ /V
8 Back-EMF constant	k_E	1,45	1,89	3,75	mV/min ⁻¹
9 Torque constant	k_M	13,8	18	35,8	mNm/A
10 Current constant	k_i	0,0724	0,0555	0,0279	A/mNm
11 Slope of n-M curve	$\Delta n/\Delta M$	27,5	25,9	24,3	min ⁻¹ /mNm
12 Terminal inductance, phase-phase	L	191	331	1 290	μ H
13 Mechanical time constant	τ_m	5,28	4,97	4,66	ms
14 Rotor inertia	J	18,3	18,3	18,3	gcm ²
15 Angular acceleration	α_{max}	123	134	144	$\cdot 10^3$ rad/s ²
16 Operating temperature range:					
– motor		-40 ... +100			°C
– winding, max. permissible		+125			°C
17 Shaft bearings		ball bearings, preloaded			
18 Shaft load max.:					
– with shaft diameter		4			mm
– radial at 3 000 min ⁻¹ (5 mm from mounting flange)		15			N
– axial at 3 000 min ⁻¹ (push / pull)		3			N
– axial at standstill (push / pull)		50			N
19 Shaft play:					
– radial	\leq	0,015			mm
– axial	$=$	0			mm
20 Mass		65,3			g
21 Direction of rotation		electronically reversible			
22 Speed up to	n_{max}	10 000			min ⁻¹
23 Number of pole pairs		7			
24 Hall sensors		digital			
25 Magnet material		NdFeB			
Rated values for continuous operation					
26 Rated torque	M_N	37	38	38	mNm
27 Rated current (thermal limit)	I_N	2,76	2,18	1,1	A
28 Rated speed	n_N	3 400	3 860	4 320	min ⁻¹
29 Rated slope of n-M curve	$\Delta n/\Delta M$	71,9	62,4	50,8	min ⁻¹ /mNm

Note: Rated values are measured at nominal voltage and 22°C ambient temperature.




For notes on technical data and lifetime performance refer to "Technical Information".
Edition 2020 Aug. 12

© DR. FRITZ FAULHABER GMBH & CO. KG
Specifications subject to change without notice.



Option, cable and connection information

Example product designation: **3216W012BXTH-3830**

Option	Type	Description	Connection		
			No.	Function	Colour
3830	Connector 	Standard cable with connector MOLEX Microfit 3.0, 43025-0800, recommended mating connector 43020-0800	1	Phase C	yellow
			2	Phase B	orange
			3	Phase A	brown
			4	GND	black
			5	U _{DD} (+5V)	red
			6	Hall sensor C	grey
			7	Hall sensor B	blue
			8	Hall sensor A	green
			Standard cable		
			Single wires, material PVC, AWG 20, Phase A/B/C		
			AWG 26, Hall A/B/C, U _{DD} , GND		

Product combination

Precision Gearheads / Lead Screws	Encoders	Drive Electronics	Cables / Accessories
26A 26/1R 32GPT 32/3R	IE3-1024 IE3-1024 L IEF3-4096 IEF3-4096 L IERS3-500 IERS3-500 L IER3-10000 IER3-10000 L	SC 2402 P SC 2804 S MC 5004 P MC 5005 S	Brake MBZ is available in combination with Encoder IEF3(L) only. To view our large range of accessory parts, please refer to the "Accessories" chapter.

For notes on technical data and lifetime performance refer to "Technical Information".
 Edition 2020 Aug. 12

© DR. FRITZ FAULHABER GMBH & CO. KG
 Specifications subject to change without notice.